POLITECNICO DI MILANO

Scuola di Ingegneria Industriale e dell'Informazione

Corso di Laurea Magistrale in Ingegneria Biomedica

Design and testing of a microfluidic hyperbolic channel to assess single cell deformation in a homogeneous extensional flow.

Relatore: Prof. Gabriele Dubini

Correlatore: Dr. Ing. Monica Piergiovanni

Tesi di Laurea Magistrale di:

Valeria Galli, 877162

Anno Accademico 2017-2018

Every book usually has one author, but hides many behind. And this one is no exception, so it is just the time to thank people behind the scene.

Before anyone else thank you, mum and dad, my firm support, always happy to encourage me to follow my dreams and ambitions.

Thank you, dearest nonna Giovanna, my biggest fan ever since.

Thank you, Federico, for being exactly as you are, my complementary colour.

Thank you, my friends of a lifetime, for always being there for me and simply my joy.

Thank you, friends from University, it has been amazing to share this path with you.

Thank you, Stefania, for being a mentor in music and life.

Thank you, professors Gabriele Dubini and Andrew deMello, for giving me the chance to work in your groups and discover the beautiful world of research.

Thank you, Monica and Gregor, for being great supervisors and inspiring researchers.

Contents

List of Figures

List of Tables

Summary

The study of mechanical properties of cells is of great interest in the scientific community, given the clinical relevance of the information that can be extracted from this label free biomarker. In the last years, the widespread use of soft lithography and microfluidics has led to the development of diverse platforms aimed at assessing cell mechanical properties at low and controlled flow rates and at a length scale in the same order as the observed objects (microns).

The present work collocates in this perspective, presenting a microfluidic hyperbolic channel designed to assess single cell deformation in a homogeneous extensional flow. The importance of this shape resides in the production of a mixture of shear and extensional flow, equally important in representing the complex flow occurring in various contexts inside the body. Importantly, in this scenario cells are deformed in a contactless mode solely by fluid induced forces, unlike most assays for mechanical phenotyping (AFM, micropipette aspiration, microfluidic constriction channels).

A fluid dynamic computational analysis was performed to assist the design and complement the experimental results with information on the main fluid dynamic parameters playing a role in deforming the cells (shear and extensional rates, shear stress). The geometries were designed with the aid of CAD softwares (SolidWorks, AutoCAD), whereas meshing and simulations were performed in ANSYS (Design Modeller, Mesh, Fluent, Direct Optimization).

Simulations showed the patterns of velocity and stresses and the values of shear and

extensional rates along the centreline (positioned at mid depth, $z = \frac{h}{2}$ and along the symmetry line in the 2D plane, $y = \frac{w_c}{2}$), the position of maximum velocity and ideally where the cells flow preferentially during experiments. Notably, the hyperbolic shape imparts a linear increase in velocity thus a constant extensional rate along the centreline (Figure 1).

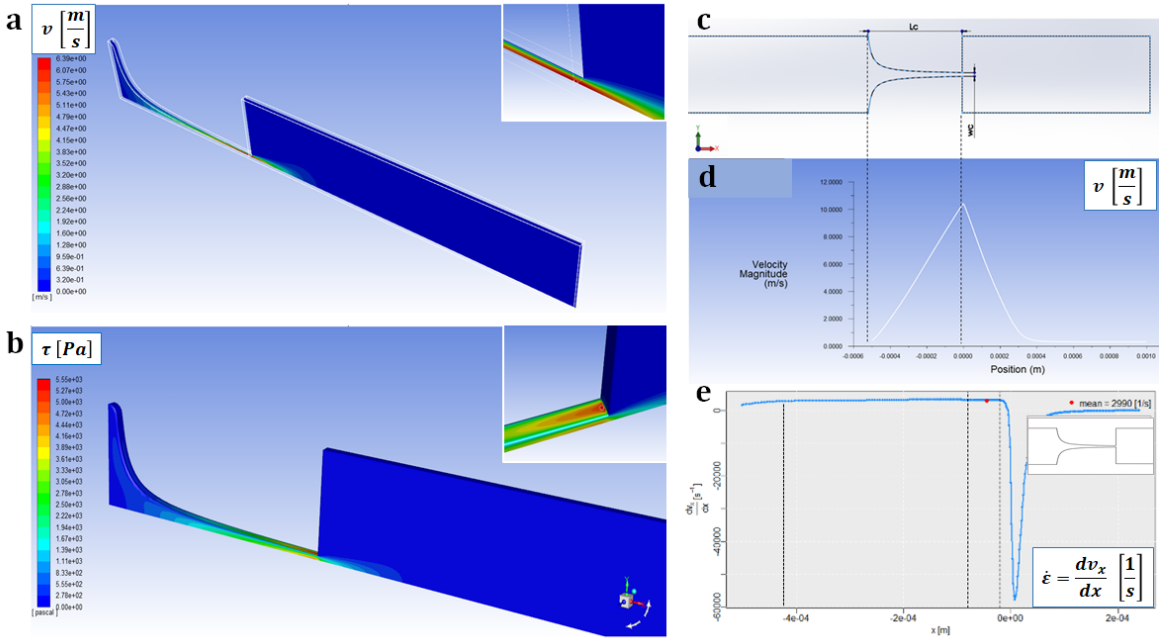

Figure 1: Overview of the computational results: the left panel shows the velocity and shear stress contours in the hyperbolic channel (half of the geometry was used exploiting the symmetry). In the right panel the velocity and extensional rate profiles along the channel are reported.

The experimental tests consisted in flowing a cells suspended in a buffer inside PDMS hyperbolic microchannels while observing them under bright field microscopy and recording videos with a high speed camera, to be then processed offline afterwards (Figure 2 on page III, a). Commercialized leukaemia derived cell lines (HL60, Jurkat) were cultured in standard conditions, harvested and resuspended in two different buffers (high and low viscosity) made of Phosphate Buffered Saline with the addition of Methylcellulose powder. Experiments were conducted at increasing flow rates (higher

for the less viscous buffer and viceversa). In total, six different hyperbolic geometries and one straight channel were used for simulations and experiments, with varying width an length but constant depth ($20\mu m$) to facilitate focusing with the 20X objective used.

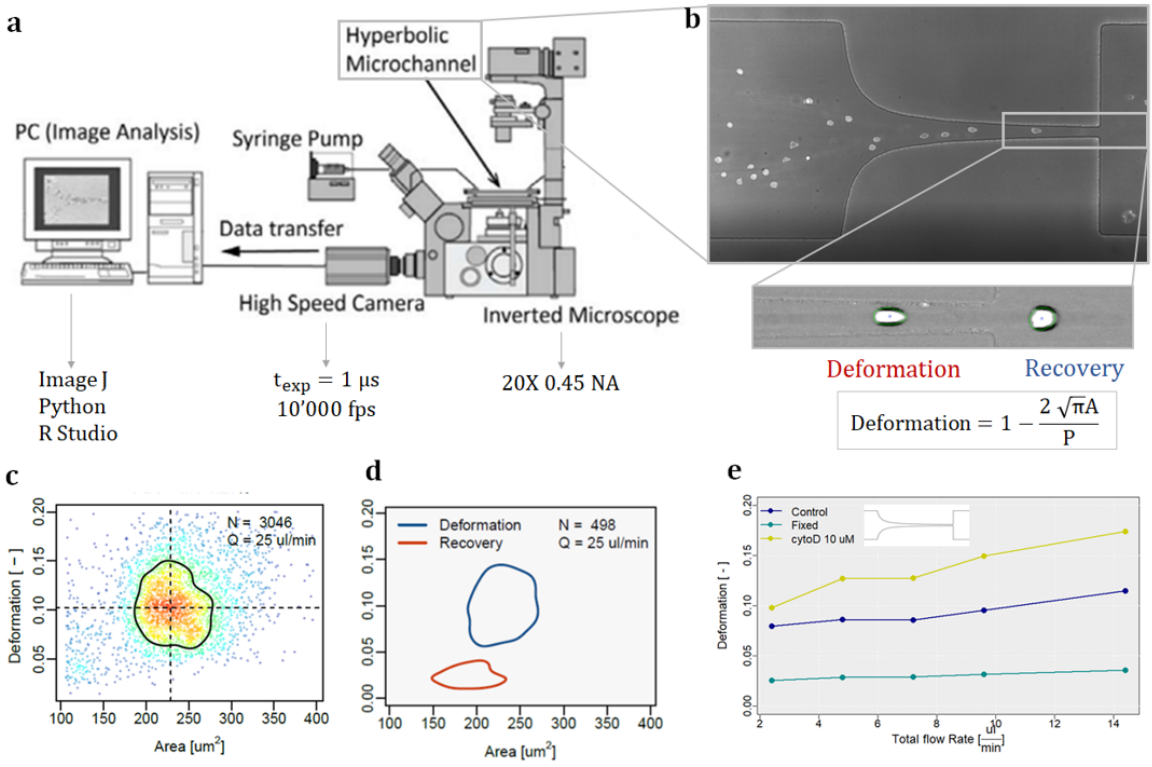

Figure 2: Schematic representation of the workflow of the experiments: images of cells flowing in the channels were recorded with a high speed camera and postprocessed offline to calculate deformation from the extracted geometrical parameters (a). A small region of interest was set and two different phases - deformation and recovery - were distinguished as the end of the channel and the beginning of the riexpansion respectively (b). Scatterplots of deformation versus area with a black line showing the 50% density contours (c) and the distinction among deformation and recovery (d) were visualized. Results showing the deformation at increasing flow rate of Jurkat cells fixed and treated with cytochalasin D were performed the long hyperbolic channel (e).

Experimental data were processed with a Python code that tracked cells, drew contours and provided their position and geometrical features (area, perimeter); deformation was calculated as a non dimensional parameter quantifying the deviation from circularity (Figure 2, b). Results were visualized as scatterplots of deformation versus detected area and a clear distinction between deformation and recovery phase

(end of the channel and riexpansion, respectively) was found in the majority of cases (Figure 2 on page III, c and d). As expected, an increase in deformation with increasing flow rate was observed and cytoskeletal affecting treatments such as cell fixation and cytochalasin D administration showed a detectable stiffening and softening effect respectively (Figure 2 on page III, e).

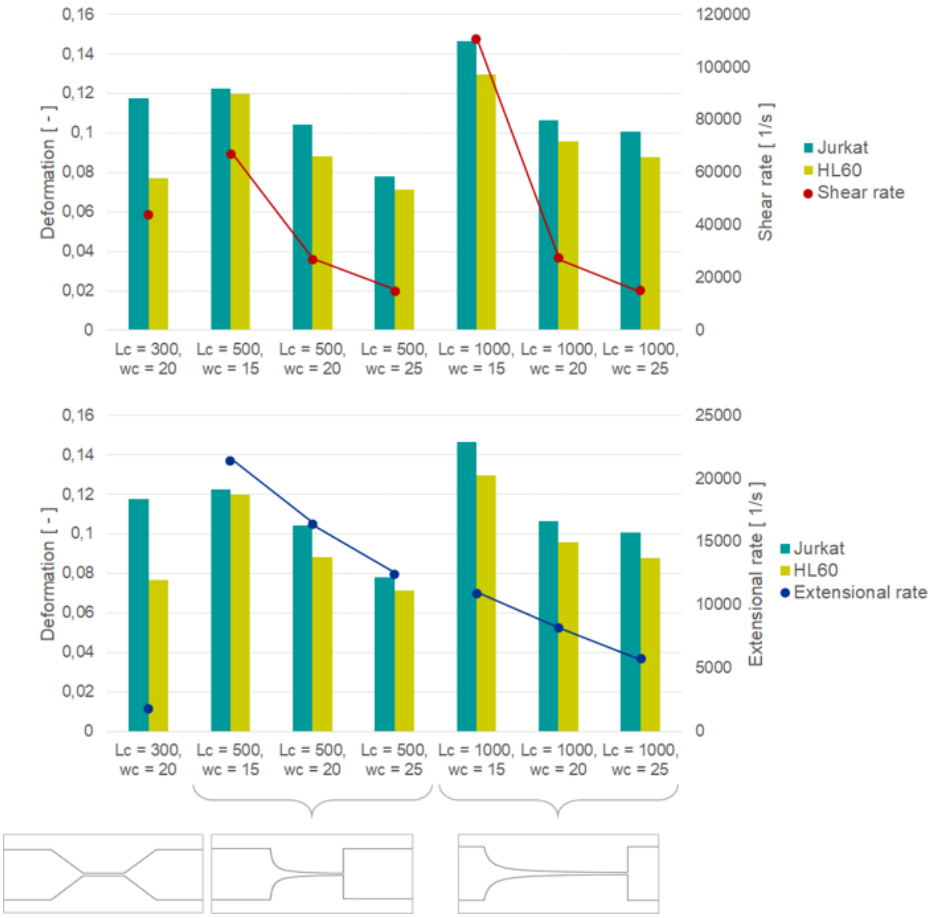

Figure 3: Correlation of experimental and computational results: for sake of clarity, the trend of extensional and shear rates are displayed in two separate plots given their difference in magnitude. Solid lines link points referring to channels with the same length and different widths at the contraction w_c.

An increase in deformation with increasing flow rate (increasing fluid induced forces) was detected, and Jurkat cells were observed to be softer than HL60 cells in all conditions. The correlation of the deformation detected experimentally with shear and

extensional rates showed that the major contributor in deforming cells in the short hyperbolic channels was the extensional component, whereas the long channel with the smallest width ($w_c = 15\mu m$) featured higher shear that revealed predominant in inducing deformation, likewise the case of the straight channel having extremely low extension but significant shear (Figure 3 on page IV).

In conclusion, this work provides a simple and fast way to probe cell stiffness in a label free manner and with minimum bias (no contact between cells and channel walls); the fluid dynamic conditions imposed are relevant as they provide both shear and extensional components found in complex flows in the body. With further development of the setup towards improvement of image quality and automation of the postprocessing, the presented platform could serve as valuable tool to evaluate the deformability of cells from clinical samples (e.g. biopsies from cancer patients).

Sommario

Lo studio delle proprietà meccaniche della cellula ha acquisito crescente interesse nella comunità medico scientifica, grazie alla rilevanza clinica di suddette proprietà che si sono rivelate un significativo indicatore di diverse situazioni fisio-patologiche quali il potenziale metastatico di cellule (sospette) cancerogene, il grado di differenziazione di cellule staminali, lo statodi attivazione del sistema immunitario ed altre ancora. Un grande vantaggio di queste caratteristiche risiede nella semplicità della loro misurazione grazie all'assenza di manipolazione biologica delle cellule comunemente operata nei test di routine (ad esempio, quelli basati sulla fluorescenza oppure test ELISA).

Negli ultimi anni, la rapida diffusione della *soft lithography* e l'uso sempre più diffuso della microfluidica in diversi ambiti hanno consentito lo sviluppo di varie piattaforme realizzate per esaminare le proprietà meccaniche della cellula. I vantaggi di questo approccio sono molteplici, primi fra tutti la scala dimensionale paragonabile alla dimensione dell'oggetto di interesse (scala micrometrica), la possibilità di controllare in modo preciso le portate e le pressioni, la ridotta quantità di reagenti necessari e il regime di flusso laminare.

Il presente lavoro si colloca in questa prospettiva, presentando un canale microfluidico di forma iperbolica progettato per analizzare la deformazione di cellule in sospensione sottoposte a un flusso estensionale omogeneo. L'importanza di utilizzare questa forma peculiare risiede proprio nel produrre un flusso complesso che presenta sia una componente di taglio che una estensionale, spesso trascurata in lavori presenti in letteratura ma di almeno eguale importanza nel simulare il complesso campo di flusso che si ritrova

in vari contesti nel corpo umano.

É estremamente importante sottolineare che, nel design utilizzato, la deformazione impartita alle cellule è frutto delle sole forze indotte dal flusso, senza alcun contatto con le pareti del device (che si ritrova invece in altre note tecniche utilizzate per la caratterizzazione meccanica delle cellule come il microscopio a forza atomica e l'aspirazione con micropipetta). Questo permette di escludere disturbi ed errori introdotti da fenomeni di adesione o frizione non quantificabili con certezza.

Complementarmente alla campagna sperimentale, simulazioni fluidodinamiche sono state condotte con lo scopo di rendere il design più efficace individuando l'effetto dei parametri geometrici sulle quantità fluidodinamiche di interesse e di correlare i risultati ottenuti con le grandezze fluidodinamiche responsabili dello sforzo agente sulle cellule. Varie geometrie con diverse dimensioni sono state realizzate mediante CAD (SolidWorks, AutoCAD) e le simulazioni sono state effettuate mediante il software ANSYS (Design Modeller, Mesh, Fluent, Direct Optimization).

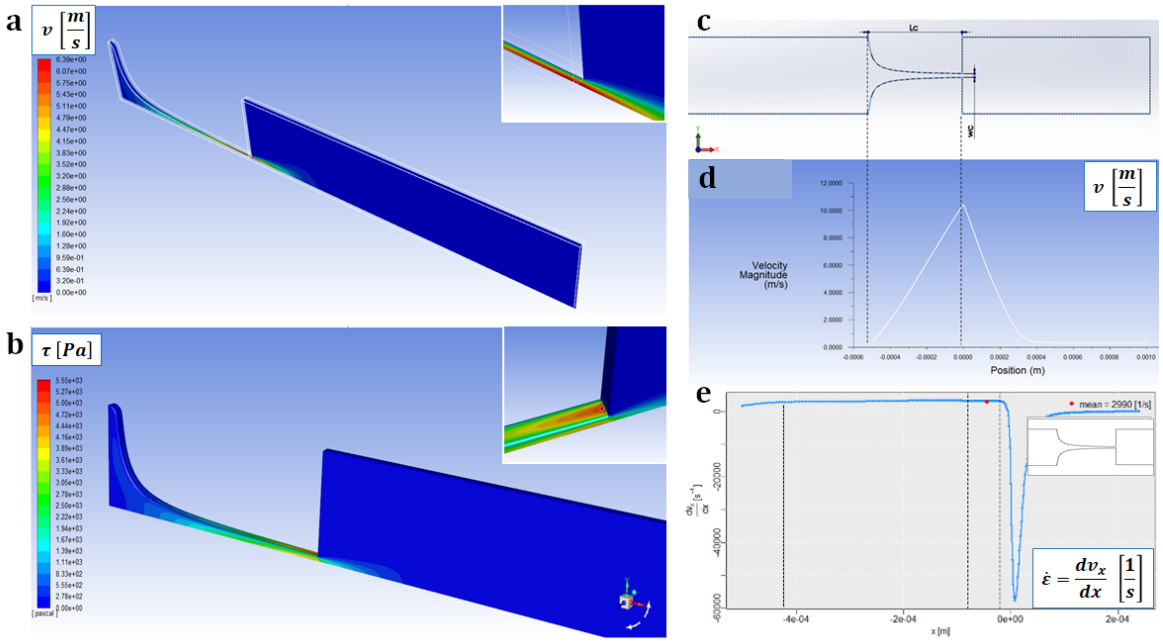

Figure 4: Panoramica dei risultati computazionali: contorni di velocità (a) e sforzo di parete (b) per il canale iperbolico corto, profili di velocità (d) ed extensional rate (e) lungo il canale (c). Le simulazioni sono state eseguite su metà della geometria sfruttandone la simmetria.

L'andamento di velocità e sforzo di parete sono stati ricavati dalle simulazioni per avere una visione complessiva delle forze fluidodinamiche in gioco ed *exensional* e *shear rate* sono stati calcolati in corrispondenza della *centreline* (Figura 4), ovvero la linea centrale dove la velocità è massima ed idealmente la traiettoria lungo cui si dispongono le cellule una volta a fuoco in tutte le direzioni (questa linea è posizionata alla metà della profondità ed equidistante dalle pareti nella direzione perpendicolare alla profondità: $z = \frac{h}{2}, y = \frac{w_c}{2}$).

Nello specifico, la forma iperbolica impartisce un andamento lineare crescente della velocità progredendo lungo il canale iperbolico (con la sezione che si restringe in modo continuo): conseguentemente, la derivata della velocità nella direzione di flusso, altresì nota come *extensional rate* è costante lungo la *centreline* per la maggior parte del canale (Figura 4).

I test sperimentali sono stati effettuati visualizzando le cellule in transito nei canali mediante microscopia ottico in campo chiaro ed acquisendo immagini con una camera ad alta velocità sotto forma di video (Figura 5, a). Cellule di linea derivate da leucemia acuta (HL60, Jurkat) sono state coltivate in condizioni standard, prelevate e sospese in due differenti buffer (bassa ed alta viscosità). Questi ultimi sono stati ottenuti mediante l'aggiunta di metilcellulosa a soluzione salina tamponata al fosfato (comunemente nota come PBS) con un fluidi pseudoplastici come risultato. Gli esperimenti sono stati condotti a portate crescenti e diversi intervalli di portata sono stati impiegati per i due fluidi tenendo conto della viscosità di ciascuno (portate più basse per il fluido più viscoso e viceversa).

In totale, sei differenti canali di forma iperbolica sono stati utilizzati con tre diverse larghezze finali; tutti i canali sono stati realizzati con una profondità di circa $20\mu m$ per facilitare la messa a fuoco con l'obiettivo ad ingrandimento 20X utilizzato.

I dati sperimentali sono stati processati mediante un codice Python che individua e traccia il contorno delle cellule e fornisce la loro posizione (coordinate del centro) e parametri geometrici quali area, perimetro, larghezza ed altezza; la deformazione è

stata calcolata - proprio basandosi su tali parametri - in termini di deviazione dalla forma circolare (Figura 5, b).

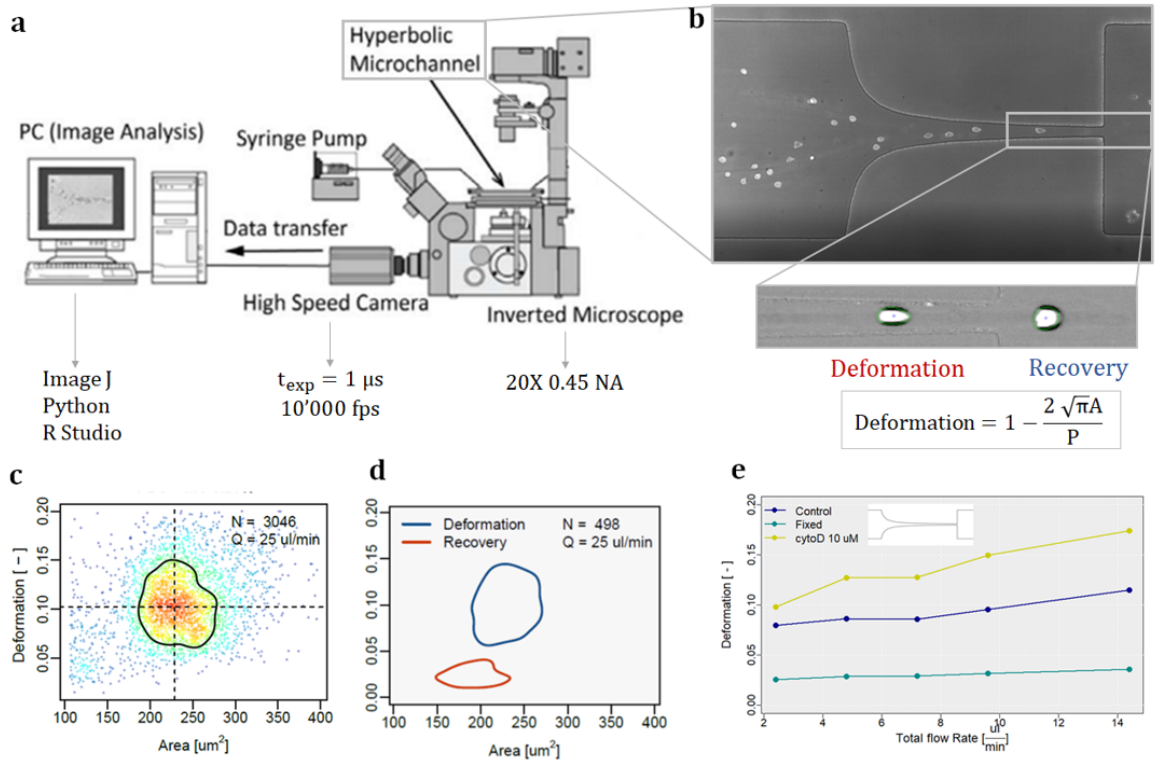

Figure 5: Schema dell'acquisizione dei dati sperimentali e rappresentazione dei risultati: le cellule che fluiscono all'interno dei canali sono state osservate in microscopia a campo chiaro e riprese con l'ausilio di una camera ad alta velocità ed i dati processati offline (a) per ricavare parametri geometrici da cui calcolare la deformazione secondo l'equazione in (b). Una regione di interesse è stata impostata e le due fasi di deformazione e recupero individuate alla fine del canale e in corrispondenza della riespansione, rispettivamente (b). I risultati sono stati visualizzati come grafici a dispersione della deformazione rispetto all'area, con una linea di contorno che racchiude il 50% della popolazione (c); la distinzione fra le fasi di deformazione e recupero è stata rappresentata considerando il 50% dei valori (d). Un esempio di risultati mostra la deformazione al crescere della portata di cellule Jurkat fissate e trattate con citocalasina D rispetto al controllo (e).

Una correlazione positiva fra portata e deformazione rilevata è stata osservata per tutte le condizioni sperimentali, concordemente a quanto atteso data la crescita delle forze indotte dal flusso all'aumentare della portata. In tutte le condizioni (tutti i canali ed entrambi i fluidi) una maggiore deformazione è stata osservata per le cellule Jurkat rispetto alle HL60, in linea con dati presenti in letteratura. La correlazione fra de-

formazione e quantità fluidodinamiche coinvolte nell'indurre lo sforzo sulla cellula ha mostrato che nei canali iperbolici con curvatura accentuata ($L_c = 500\mu m$) la componente estensionale gioca un ruolo preponderante mentre nei canali iperbolici lunghi che nel tratto finale sono più simili a canali dritti, soprattutto nel caso con $w_c = 15\mu m$, la componente di taglio contribuisce alla deformazione in modo sostanziale, analogamente a quanto accade per il canale dritto (Figura 6).

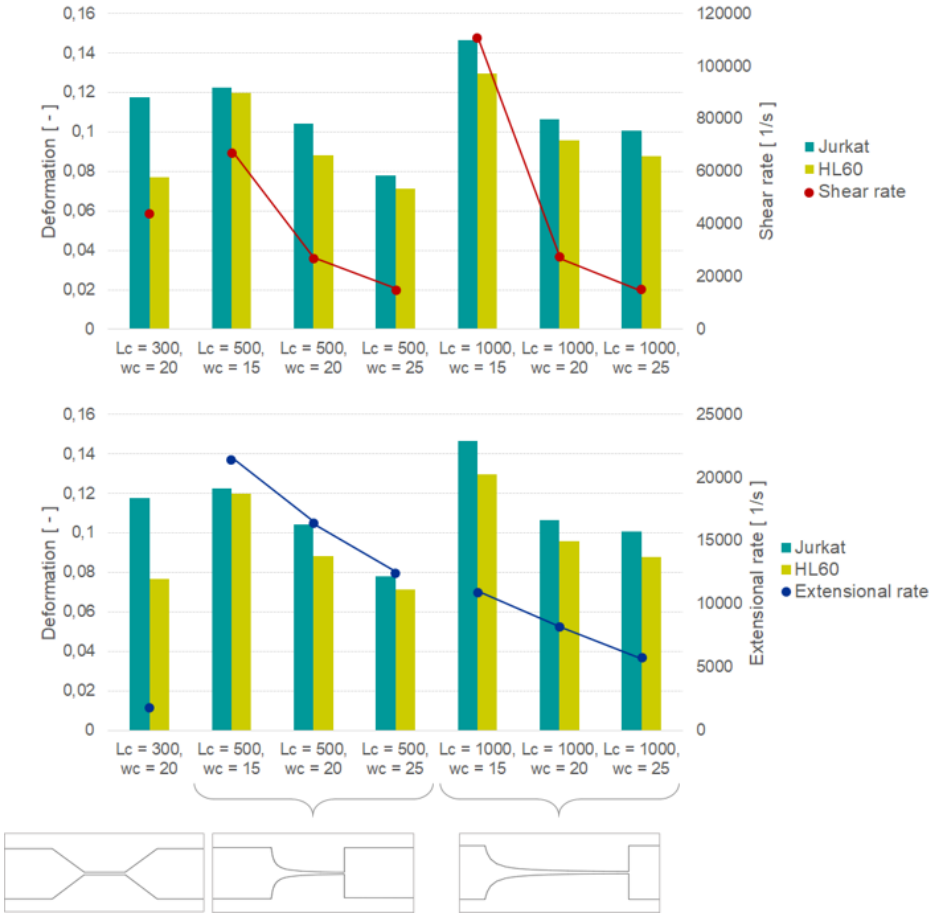

Figure 6: Correlazione fra risultati sperimentali e computazionali: per maggior chiarezza, gli andamenti di shear ed extensional rate sono rappresentati su due grafici differenti, mentre le deformazioni sperimentali sono riportate identicamente. Le linee collegano i punti relativi a canali con la stessa lunghezza e diversa larghezza alla contrazione w_c.

In conclusione, questo lavoro si propone di offrire un device ottimizzato per misurare la deformazione di diversi tipi cellulari in modo semplice e rapido, senza l'uso di

alcuna molecola aggiuntiva nè di contatto con le pareti del canale; particolare interesse è stato posto nell'osservazione delle condizioni fluidodinamiche per ottenere una combinazione delle componenti estensionale e di taglio nel flusso.
Con futuri miglioramenti del setup verso una migliore qualità delle immagini e l'automazione del processo di postprocessing, il device presentato potrebbe rivelarsi un valido strumento per valutare la deformabilità di cellule provenienti da campioni biologici di rilevanza clinica, come ad esempio, cellule cancerogene derivanti da biopsie di pazienti.

Introduction

0.1 Motivation and aims

The present work presents a microfluidic platform for single cell deformability measurements: on the wave of the spread of new topics in biomedical research like point of care diagnostics and lab on a chip devices, a tool to assess cell mechanical properties in a simple and fast way was envisioned. Indeed, cell stiffness and viscosity have proven to be promising label-free biomarkers for many scenarios in cell physiology and pathology, thus acquiring growing importance in research and yielding significant efforts from the scientific and medical communities.

Diverse research groups have brought up microfluidic devices of various shape to perform measurement of cell deformability: their impact on clinical practice is potentially very significant, with applications ranging from the identification of rare populations for cancer cell detection to quality control for stem cell therapies, prediction of sepsis and transplant rejection phenomena but also detection of various diseases (well known conditions like malaria, osteoarthritis and diabetes but also rare pathologies like sickle cell disease and spherocytosis).

In this scenario, the aim of this project is to provide an optimized platform to probe cell stiffness with solely fluid induced forces, with particular attention to the flow characteristics: unlike the majority of works in literature, this study focuses on the establishment of a mixture of shear and extensional flows, to provide a closer resemblance of the complex flow occurring inside the body (microcirculation) and in extracorporeal devices of small lumen such as needles and catheters entering larger vessels (when a rapid and sharp increase in velocity takes place).

The primary objective of this work was to find a suitable design that could enclose both components (shear and extension): the choice of the peculiar hyperbolic shape lies precisely on this underlying consideration. Importantly, two different but complementary means for designing were employed to address the problem: on one hand,

computational fluid dynamics served as a powerful means of investigating thoroughly, inexpensively and with good accuracy the overall characteristics of a device in terms of the main parameters playing a role (velocity and its derivative, shear stress); on the other hand, an experimental campaign only could provide direct and tangible information on the feasibility of a design, especially in terms of limitations of the setup (one thinks, for example, about the resolution that can be reached thus the information that can be effectively detected).

As far as the acquisition and analysis of experimental data is concerned, it is essential to point out that image quality was of striking importance: being the deformation extracted from the analysis and manipulation of optical images, the value and reliability of results strictly relied on this aspect.

In the light of what stated above, the secondary objectives of this work were the following:

- to individuate the main geometrical parameters influencing the distribution of velocity and stresses, and appropriate size of the devices (computational);
- to find the optimal condition in terms of flow rate, addressing the trade-off between inducing a detectable deformation and limiting the motion blur in images when cells reached high speeds: to this regard, fluids with different viscosities were also considered (experimental);
- to optimize a set-up and the protocol for experimental tests such that the best possible image quality could be obtained in a reasonable runtime, considering the biological nature of the tested objects that may undergo uncontrolled variation, possibly influencing the measured deformation (experimental);
- to relate the detected deformation with the computational findings, gaining insight on the forces responsible for the deformation induced on cells in a certain fluid dynamic configuration (computational and experimental).

As it is evident that the pursue of reliable biological results in terms of absolute values of deformation of the tested cells would require accurate handling of the biological samples by a skilled operator, this goes beyond the scope of this work, that aims rather at providing a simple, functioning platform to probe cell stiffness in a fast and reliable way. Upon further refinement and development of the existing solution, the greater ambition is to employ the device to test clinically relevant samples in the future (e.g. biopsies from cancer patients), with the aid of biological expertise to obtain reliable results that could serve in the diagnosis or prediction of diseases of great interest in the clinical community.

0.2 Outline of the work

A preliminary computational study to aid the design of the device was carried out and few geometries were chosen to be used for experiments. Afterwards, the experimental campaign was conducted on commercially available leukaemia cell lines in all the designs (and two additional ones found in the literature to provide a means of comparison). Eventually, the numerical and experimental results were analysed jointly and correlated.

The computational section was carried out in the Laboratory of Biological Structures Mechanics at Politecnico di Milano (Microfluidics group), whereas the experimental part was performed in the Department of Chemistry and Applied Biosciences at ETH Zurich (deMello group).

0.3 Outline of the thesis

At first, a brief overview of the human cell and of the current clinical applications of mechanical phenotyping are presented (**Biological background**).

In **State of the art**, the main techniques to study cell mechanical properties are de-

scribed with particular emphasis on the class of microfluidic systems. Computational efforts present in the literature are also highlighted to show the importance of this tool to support the experimental work.

Protocols of simulations and experimental tests, together with the setup and the materials used, are described separately and in detail in **Materials and Methods**.

In **Results and Discussion**, computational and experimental findings are presented and discussed separately at first, then critically correlated.

Lastly, general conclusions and further developments are given in **Conclusions**.

Biological background

1.1 The human cell

Cells are the basic functional units of the organism, accomplishing their living functions while strongly interacting with the physiological environment around them. Cell biology is a broad field of research that has provided extensive studies on the multitude of cellular components and functions (Figure 1.1), revealing complex interactions and internal mechanisms. Shortly, the membrane serves as structural barrier and regulator of substance permeability; the nucleus is well known as the control core of the cell, with production and regulation of the genetic material; mitochondria take part in the oxidation processes to produce energy; ribosomes are involved in the synthesis of proteins, other organelles accomplish specific functions (e.g. Golgi apparatus, lysosomes, etc) and the cytoskeleton acts as the cell structural sustain (Scanlon and Sanders, 2007).

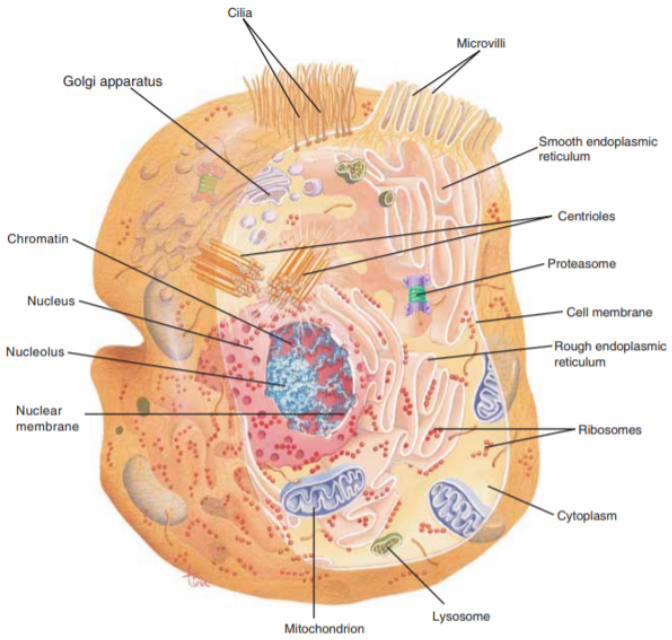

Figure 1.1: Eukaryotic cell with organelles and subcellular structures (Scanlon and Sanders, 2007).

On the other hand, system biology encourages the study of interaction of such living systems with the surrounding environment: these occur primarily by contact with

the neighbouring cells and with the extracellular matrix they are embedded in (El-Ali et al., 2006), by exerting mechanical forces, producing and destroying it continuously (Geiger et al., 2001). They are capable of sensing many different physical and chemical cues and to react accordingly; in particular, they sense mechanical stimuli through mechanosensitive pathways and respond by reorganization of the cytoskeleton and force generation (Moeendarbary and Harris, 2014).

Regarding the cell as a complex system, many efforts have been made to disentangle the interaction and processing of the multiple input signals and the resulting behaviour (Figure 1.2): environmental cues (such as cytokines), mechanical interaction with the extracellular matrix (ECM) and temperature conditions are among the factors determining cell behaviour (meaning movement, secretion, endocytosis, differentiation, division, and apoptosis). Inside the system, a multiplicity of activities takes place, localized in space and time. Unlike man made machines, the functioning of human cells is still far from being fully understood and characterized, mainly because of the enormous inter variability of different cell types (Carlo and Lee, 2008).

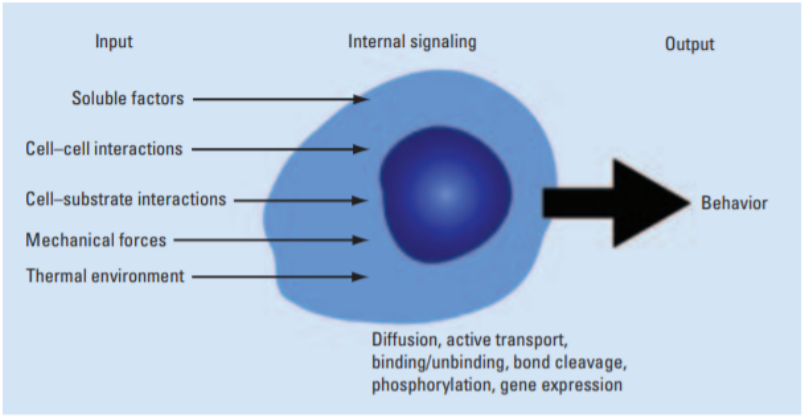

Figure 1.2: The human cell as a system, with an input-output response.

1.2 Clinical relevance of mechanical phenotyping

The mechanical behaviour of cells in their natural environment and in contact with artificial substrates is of great interest for uncountable applications and has been extensively investigated (Discher et al., 2005), also with a focus on the subcellular and molecular mechanisms underlying the macro scale mechanical properties (Suresh, 2007). Some have pointed out the complexity of mechanical characterization of such living entities, with the hypothesis - the so-called *tensegrity* model - of a prestressed state that together with external stimuli makes up for the overall behaviour (Wang et al., 2001).

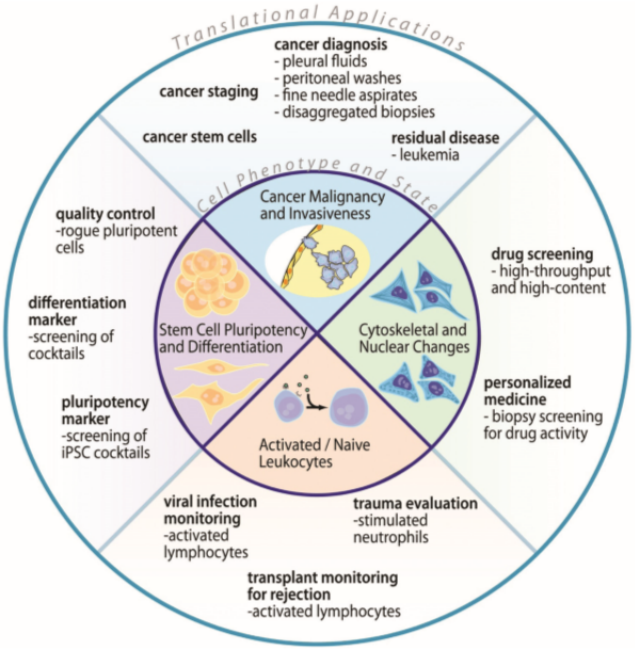

Figure 1.3: Overview of the main clinical applications of mechanical phenotyping (Di Carlo, 2012).

The importance of the analysis of cellular morphology and characteristics has been growing since the detection of rare cells (e.g. circulating tumour cells) was recognized as key instrument for early disease detection. The routine methods to study cellular

mechanisms and activity include flow cytometry (based on the detection of light scatter through cells often labelled with fluorescent markers), immunoassays (e.g. ELISA) relying on the measurement of the concentration of a certain molecule (antigen) when detected by an antibody which has to be linked to the cell, or genomic analysis. Nonetheless, a major drawback of all these technique appears as the uncontrolled change in cell physiology induced by linking a molecule to it (Murphy et al., 2018). Another important limitation that could be potentially overcome by the use of label-free mechanical assays is the strong variability of data among different laboratories, which is largely due to manual sample preparation procedures (Di Carlo, 2012).

Mechanical and physical properties of cells offer a good perspective of cellular characterization with valuable information and minimum perturbation of the cell during measurement. A thorough review from Di Carlo (2012) summarizes the main biological phenomena that can be linked to cell deformability (Figure 1.3), highlighting the significant clinical relevance of the mechanical properties of cells, while underlying the main drawbacks of current techniques, namely greater time consumption, reagent cost, assay complexity and low throughput.

Indeed, numerous and diverse applications in the context of translational medicine have already been attempted, investigating links and correlations of cell stiffness and viscosity to pathological states, phenotype identification, analysis of immune status, malignancy detection, drug screening and many others (Darling and Di Carlo, 2015).

In the following paragraphs, the main areas of investigation of mechanical phenotyping are described, given that there exist many more (still at a more pioneering stage) such as phenotype investigation, processes like locomotion or differentiation (Wang et al., 2013), effects of senescence (Schulze et al., 2012) and others, that are not illustrated in further detail for the sake of conciseness.

1.2.1 Red blood cells: disease detection

Many groups have been focusing their investigation on red blood cells, as their softness is a key feature for physiological functioning of the whole circulation: these small cells normally squeeze into capillaries smaller than their diameter thanks to the absence of a nuclear structure, which constitutes the stiffest part of the cell (Guilak et al., 2000). An increase in stiffness of red blood cells impedes their normal flow through micro vasculature leading to serious impairment in peripheral tissues perfusion and oxygen supply (Guo et al., 2017) and dangerous vaso-occlusive phenomena (Guo et al., 2012).

Red blood cells have been extensively characterized for the relevant stiffening that occurs in pathological conditions like malaria (Hou et al., 2010), sepsis (Lee et al., 2009), spherocytosis (Guck et al., 2005) or sickle cell disease (Suresh, 2006)(Rosenbluth et al., 2008), but also during storage in blood banks (Xu et al., 2018). On the other hand, their excessive deformation ins some cases has been hypothesized as a trigger to hemolysis, especially in extracorporeal devices where cells undergo strong complex flows (Yaginuma et al., 2013).

1.2.2 White blood cells: immune status

Much less investigation has been conducted on white blood cells which constitute a minor percentage in blood samples with respect to the abundance of red blood cells. To this regards, the prominent difference in stiffness of white blood cells with respect to the softer red blood cells has led to deformability based separation in continuous flow (Rodrigues et al., 2015)(Fay et al., 2016), developing an alternative to the more commonly used size based separation systems (Chen et al., 2014).

The focus on white blood cells deformability is motivated by the ability to predict and investigate a complex and important phenomenon as leukocyte activation: it has been shown that monocytes and neutrophils become stiffer upon activation through

chemokines (Worthen et al., 1989) and the exacerbation of this stiffening was observed in sepsis and trauma patients with tremendous increase in micro capillaries occlusion and consequent complications (Morikawa et al., 2015). Lymphocytes, on the other hand, have been shown to decrease their stiffness upon activation in order to allow transmigration through vasculature and lymph nodes (Brown et al., 2001).
Many other clinical situations of interest evolve around the immune status, thus a potential tool for their prediction and diagnosis is of outstanding interest in scenarios like allograft rejection or response to treatment in HIV patients (Gossett et al., 2012). Some investigated the deformability of white blood cells with deep understanding of the intracellular mechanisms guiding leukocyte activation upon inflammation, trying to trace the cytoskeletal components responsible for the increased deformability that allows migration to the site of injury: such studies have the potential to create a strong, useful link between inflammatory processes and mechanical changes footprints (Fay et al., 2016).

1.2.3 Cancer cells: malignancy and metastatic potential

The use of cell deformability as a biomarker has earned much credit is the study of cancer development and expansion: many findings support the theory that the capability of tumour cells to migrate and metastasize through the body could be also due to an abnormal softness (Rosenbluth et al., 2008)(Hou et al., 2009), possibly attributed to changes in the concentrations of cytoskeleton contents and structure – from a rather ordered and rigid one in normal cells to a more irregular and compliant state in cancer cells (Suresh, 2007).
Cancer cells must not only squeeze through the extracellular matrix and endothelial cell-to-cell junctions, but they must also travel through small capillaries to reach a distant site: to do so, they may undergo an epithelial-mesenchymal transition involving numerous biochemical and cytoskeletal changes that enable them to maintain a motile

and invasive state: this requires much greater deformability than any normal healthy cell (Zheng et al., 2015). Some also suggested a reduction in friction with surrounding tissues to be contributing, together with softening, to the invasiveness of highly metastatic potential of some cancer cells (Byun et al., 2013).

Notably, mechanical tests have not only been performed on cell lines but also on primary cancer cells from patients (Cross et al., 2007)(Remmerbach et al., 2009). A very interesting work with atomic force microscopy on *ex vivo* metastatic cancer cells extracted form pleural fluids of patients reported findings in line with routine immunohistochemical assays, supporting the relevance and reliability of cell stiffness as a biomarker of cancerous state(Cross et al., 2007).

Further, investigation on deformability of cancer cells was conducted to assess drug resistance: anti-cancer drugs, for example paclitaxel, are known to act on the cytoskeleton with an ultimate stiffening effect: screening biopsies retrieved from cancer patients with subsequent measurement of viscoelastic properties of cells could reveal as a powerful tool to detect drug resistant cells as the ones preserving abnormal softness after treatment (Islam et al., 2018).

Others pointed out that the increase in stiffness of leukaemia cells due to chemotherapeutic treatment could be harmful as they could be trapped in micro vasculature and create clogs: with mechanical characterization, a distinction in the process of stiffness increase induced by different chemotherapies on specific leukaemia cell types could be assessed, giving valuable information on the expected consequence of such change (Lam et al., 2007).

Overall, stiffness based cancer detection and study bring the enormous advantage of a quantitative approach to assist and replace the qualitative morphological analyses of shape change that are currently trusted as detection methods (Cross et al., 2007).

1.2.4 Stem cells: differentiation state

Deformability has also proved to be an indicator of stem cells differentiation and potency: higher deformability has been found with different techniques in undifferentiated stem cells, which would allow them to spread more easily; this was observed, for example, in a study based on stem cell derived red blood cells (Guzniczak et al., 2017). Such softness smears out with cell differentiation due to stiffening of the nuclear structure and condensing of intracellular material (Pajerowski et al., 2007). The discrimination of mesenchymal stem cells from their progeny is not an easy task with currently used biochemical markers, so deformability based assessment of stem cells state of differentiation appears as a powerful tool in regenerative medicine (Gossett et al., 2012).

More importantly, the assessment of deformability appears as an earlier quality control process prior to the implantation of stem cells: if not fully undifferentiated pretransplantation (softer), they could have tumorigenic effects (Di Carlo, 2012)(Pajerowski et al., 2007), and when transferred to Phosphate Buffered Saline twenty-four hours before being injected, they may suffer from starvation thus turning stiffer than fresh cells (Cha et al., 2012). It clearly appears that sorting based purification of stem cells relying on mechanical properties - with much higher throughput than currently used methods like Fluorescence Activated Cell Sorter - could hold tremendous benefit in cellular therapies that are catching on in regenerative medicine, by reducing the risk of implanting not fully differentiated dangerous cells.

State of the art

2.1 Techniques to measure the mechanical properties of cells

Since cell deformability has been recognized as an important biomarker in the biomedical community, several techniques have been developed to measure it under various forms like deformation observed directly by the shape but also quantities derived with the aid of mathematical models (e.g. Young modulus of an equivalent elastic sphere, shear modulus of a liquid droplet model, etc.).
Among them, a major distinction exists based on the presence of direct contact of the probe with the cell: all sorts of methods rely on forces physically applied on the cell surface, whereas microfluidic devices can either rely on physical constriction of the channel walls or on contactless fluid induced deformation. Importantly, some of the earliest techniques have been reproduced in a microfluidic environment later on to enhance throughput, as explained later in this section.
In the following paragraphs, an overview of the main state of the art techniques is given with highlight on their advantages and drawbacks.

2.1.1 Micropipette aspiration

The earliest technique at record is micropipette aspiration, dating back to 1960s with the analysis of red blood cells in normal and swollen state (Rand and Burton, 1964). The cell is sucked into a glass capillary with a lumen smaller than its size by applying a negative pressure on the opposite end of the capillary; the process is observed in bright field microscopy (Figure 2.1) and measurements of aspiration length and speed are taken and used in analytical models of the cell viscoelastic behaviour to derive Young Modulus and viscosity (Alexopoulos et al., 2003). The rate of the applied pressure influences the deformation and recovery as these are inferred to be dependent on actin remodelling in the cytoskeleton, with lower stiffness at faster rate of

applied pressure (Pravincumar et al., 2012). Despite some argued that friction with the capillary walls could be negligible in the calculation of the elastic modulus (Alexopoulos et al., 2003) this still remains a major drawback of this method along with non specific adhesive phenomena that were tentatively prevented by coating the capillary with silicon solution (Pravincumar et al., 2012). Furthermore, it clearly appears that this method involves a serial modality of measurement that is highly time consuming and operator intensive.

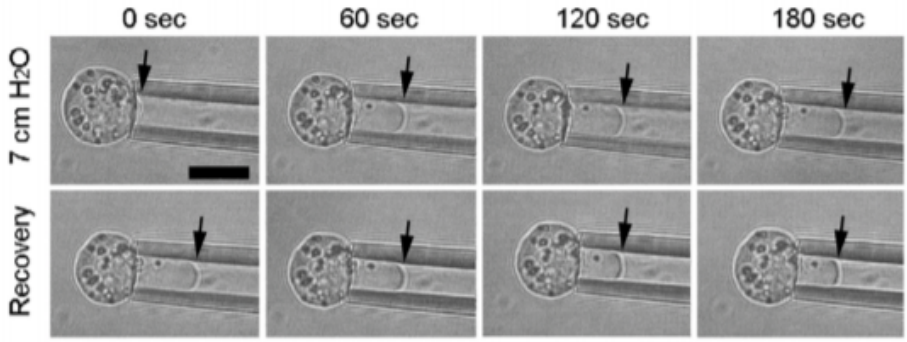

Figure 2.1: Microscopy images of a chondrocyte being aspired into a glass capillary by negative pressure and subsequent released to recover. Arrows indicate the aspiration length into the micropipette (Pravincumar et al., 2012).

2.1.2 Atomic force microscopy

Atomic force microscopy (AFM) is the benchmark technique for the measurement of surface topography at the nanometric scale, with various commercially available systems. An indenter tip mounted on a cantilever with a reflecting surface scans the surface: the deflection of such cantilever is recorded by a laser diode and the voltage difference converted into a vertical displacement, which informs elasticity models (e.g. the Hertz model) from which stiffness is derived.

Clearly, suspended moving cells may slip under the cantilever, so they need to be immobilized before being probed. One way to do so is by linking cells to a functionalised surface, with adherence possibly influencing the deformation mode of the cell (Rosenbluth et al., 2006). Confinement in microwells with continuous supply of fresh medium

has been inferred to provide a more suited environment for cells (Figure 2.2).

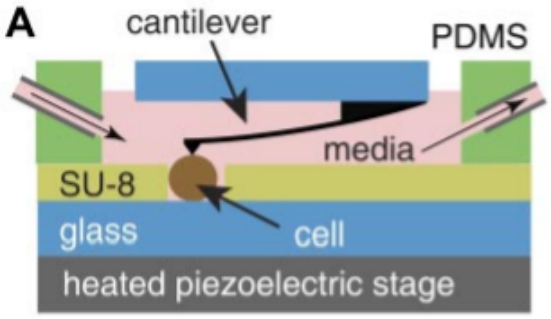

Figure 2.2: Representation of atomic force microscopy experiment on a cell confined in a microwell (Lam et al., 2007).

AFM provides useful localized information on cell stiffness but processes one cell at a time, thus yielding high time consumption and low throughput; automation remains hard due to complexity of precise simultaneous control of forces on parallel cantilevers (Darling and Di Carlo, 2015). Nonetheless, this remains a reliable technique still in use as assay to compare and validate measurements performed with different platforms, as also shown in an AFM study on metastatic cancers from pleural fluids whose findings in terms of stiffness of diverse cancer populations were in line with routine immunohistochemical assays use for diagnosis (Cross et al., 2007).

2.1.3 Optical tweezers and laser traps

Many works have relied on the use of optical forces to trap and stretch suspended cells either with the aid of microbeads attached to them (Figure 2.3) (Qie et al., 2004) or directly pointing the beams on cells flowing in glass capillaries (Remmerbach et al., 2009) or microfluidic channels (Guck et al., 2005): two counter propagating laser beams trap the cell at low power then stretch it by increasing the intensity and the deformation is observed and measured by video microscopy. While it is evident that non specific adherence to the beads may have a non negligible effect on the deformation mode and

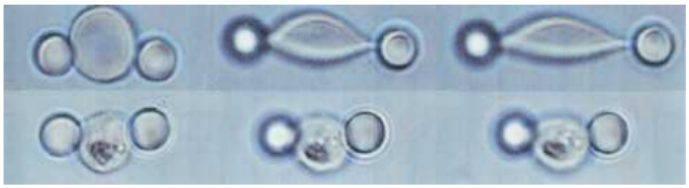

Figure 2.3: Optical microscopy images of a human red blood cells subjected to optical tweezers: a healthy cell deforms substantially (top) whereas the malaria infected red blood cell appears undeformed under the same force (bottom)(Qie et al., 2004).

measurement, optical stretching with beams directly on cells could provide a solution to this regard and potentially be brought on a high throughput scale in a microfluidic environment, with serial measurement of optical deformability as flowing cells pass through the beam (Figure 2.4).

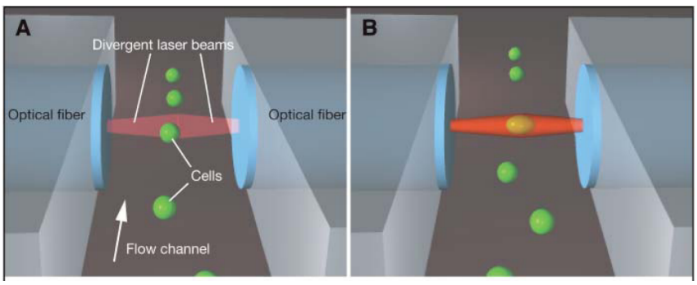

Figure 2.4: Illustration of the optical trapping and stretching mechanism in a microfluidic channel (Guck et al., 2005).

The complexity of this systems lies on the precise alignment of the two beams that is crucial for effective trapping and stretching (Zheng et al., 2013). The main disadvantage remains the degree of deformation that can be induced, limited to piconewtons in the case of tweezers (micro beads); even if nanonewtons can be reached for optical forces directed on cells, laser induced heating and photodamage need to be taken into account (Darling and Di Carlo, 2015).

2.1.4 Microbead rheometry

By placing magnetic particles on the cell and observing their motion (Figure 2.5), rheological properties can be monitored in time. The main benefit of such procedure is the possibility to provide localized information on multiple locations of the cell at the

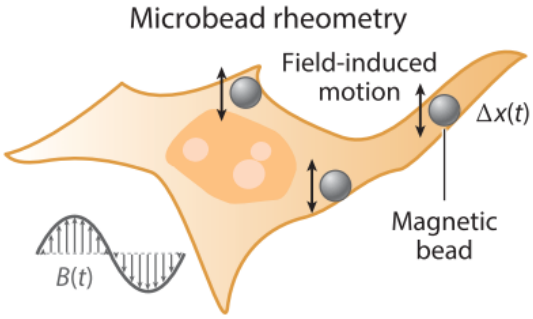

Figure 2.5: Schematic representation of the microbead rheometry experiment. Adapted from (Darling and Di Carlo, 2015).

same time, with deeper understanding of the behaviour of single cellular components (not feasible with AFM or micropipette aspiration, for example). Most of the times an external magnetic field is applied, so the active response of the cell is investigated (Wang et al., 1993).

A major hurdle to the translation of such technique to a high throughput level (e.g. with the use of microfluidic platform) is the simultaneous recording and monitoring of different beads on more than one cell continuously with the high resolution that is required (Darling and Di Carlo, 2015).

2.2 Microfluidic platforms

With the advent of soft lithography, the production of inexpensive and customizable microfluidic platforms has paved the way for uncountable different devices for cell analysis and deformability measurement, with the substantial advantage in terms of throughput.

Basically, these are realized in transparent polydimethylsiloxane (PDMS) poured and left to polymerize onto a pattern known as master. The master is obtained via UV induced polymerization of a photoresist (typically SU8): the channel pattern design is printed on a photomask (usually the cheapest category - oil emulsion masks - are accurate enough for features not smaller than $1\mu m$) and SU8 is poured onto a silicon

wafer; when UV light goes through the mask it selectively polymerizes the exposed SU8. Upon baking and development of uncrosslinked photoresist the final master is obtained: the master has to be the negative of the desired PDMS structure. Finally, the PDMS structure is peeled off the wafer, punched and bond to a glass slide (Figure 2.6).

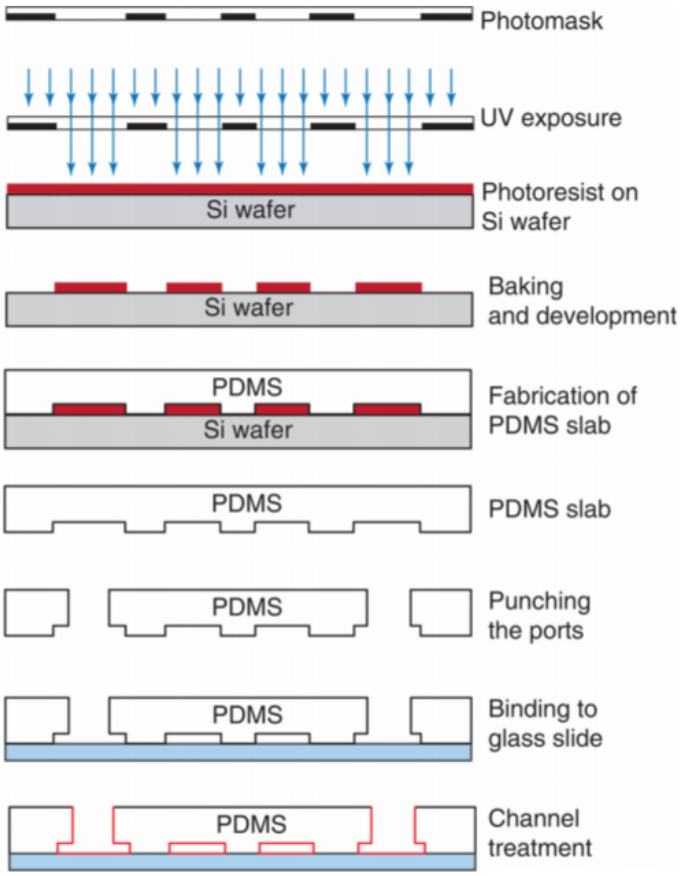

Figure 2.6: Schematic representation of soft lithography (Ung et al., 2013).

Cells flowing through transparent channels of dimension in the order of micrometers (comparable to their size) are imaged and videos are recorded for subsequent processing and extrapolation of parameters of interest. It readily appears that there is in theory no limit to the number of cells serially processed, with thousands to millions of cells per minute being analysed. This is crucial for the clinical applications discussed above: from rare cell population detection - such as malignant cells in pleural fluids (Gossett et al., 2012) - to isolation and study of the minority of white blood cells in whole blood

samples or even screening of batches of stem cells as quality control prior to implantation (Cha et al., 2012).

The use of microfluidics has been growing exponentially in the last decades in many fields of research, thanks to several advantages like reduced reagent quantities (particularly important for biological samples that usually are available in small quantities), the laminarity of the flow and the significant fluid induced stresses that can be applied at relatively low flow rates, tight control of the conditions and size comparable to the studied objects. Moreover, the miniaturization of more complex devices in the study of cellular mechanisms (not only mechanics) is a vibrating area with a lot of different cell based microsystems presented in literature under the framework of lab-on-a-chip or micro-total-analysis-systems, known under the acronym "µTAS" (El-Ali et al., 2006).

As far as deformability studies are concerned, it clearly appears advantageous to have a platform that does not require costly fluorescent labelled antibodies and skilled technicians to prepare samples and carry out tests. Also, the interpretation of results via image processing of cells flowing into the microfluidic chips, rather than an operator based analysis, promises the reduction of human error; this, together with minimal sample handling provides a sharp reduction in operator time and bias (Gossett et al., 2012).

In broad terms, microfluidic platforms for cell analysis classify in bulk and single cell systems: the former comprise microfluidic networks of pillars (microfiltration) or microvasculature mimicking networks, whereas the latter probe single cells with different mechanisms, described in more detail later in this chapter.

What is important to acknowledge is the limit of bulk measurements that make use of averaged results over a heterogeneous population, being a benefit to gain an overview of cell behaviour but insufficient to trace rare cells anomalies inside a broad population (Carlo and Lee, 2008). Single cell approaches, on the other hand, provide a less misleading characterization taking into account sample heterogeneity and, more importantly, individuate the "outliers" potentially embodying the source of rare diseases. Also, it

has been proved that a high heterogeneity can be present in populations of seemingly identical cells, like primary cells samples from animals or patients: this feature could only be addressed by studying them at the single level and may ideally allow to reveal and target single drug resistance cells (Murphy et al., 2018).
Among single cell approaches, a main classification can be done based on the presence of contact of cells with the channel walls: constriction channels of all sorts feature a cross section smaller than the cell size and deform it by means of the physical presence of the channel walls, whereas larger channels rely on fluid induced deformation only.

2.2.1 Constriction channels

The simplest way to induce deformation is to physically squeeze cells through constrictions or pores smaller than their size (Figure 2.7). Cells are known to be viscoelastic and able to deform to certain extents, depending on their cytoplasmic content and organization. The implementations of this principle rely on different readout methods of cell deformation and transit through the physical constriction: simple imaging (Fay et al., 2016) (Hou et al., 2009) electric impedance change (Adamo et al., 2012) (Zheng et al., 2015) or buoyant mass sensing (Islam et al., 2018).

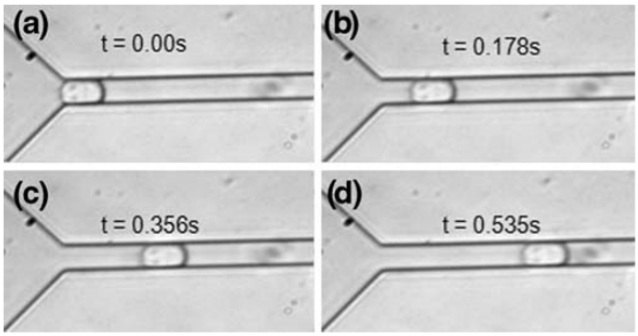

Figure 2.7: Optical images showing a breast cancer cell (typical size $20 - 25\mu m$ flowing through a channel with $10X10\mu m$ square cross section (Hou et al., 2009).

A different approach, inspired by micropipette aspiration, consisted in the use of and array of funnel constrictions with progressively smaller apertures (Figure 2.8): a

measure of the pressure applied (very precise) together with a model of cells (liquid droplets with constant volume and cortical tension) could give the effective stiffness of healthy and malaria infected red blood cells (Guo et al., 2012).

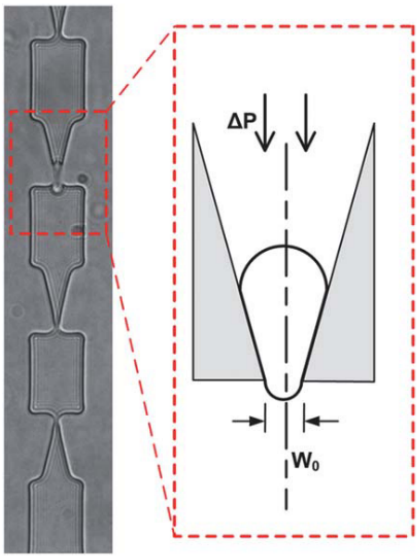

Figure 2.8: Bright field image of red blood cells flowing to progressively smaller funnel constrictions driven by a controlled pressure δP (Guo et al., 2012).

2.2.2 Hydrodynamic approaches

On the other hand, hydrodynamic approaches rely on fluid induced forces, with no contact with cell walls. Depending on the geometry of the channel, different flow patterns establish with predominance of shear or extension. Cells flow inside these channels much faster than in constriction channels, due to the absence of contact. What is common to all experiments and findings in deformability without contact is that higher flow rates, and in general higher cell velocity (e.g. a smaller cross section, on equal flow rates) imply a more pronounced deformation. As for the case of constriction channels, data are usually acquired via high speed recording in bright field microscopy.

Straight channels

The simplest solution is a straight channel with cross section larger than the probed cells: after an initial length the flow is fully developed and here the deformability is measured. A famous group in the field developed a real time deformability cytometer that acquires images and processes them with an in built software in real time: cells are deformed at very low flow rates thanks to a high viscosity buffer and shear stress and pressure gradient play a major role with respect to inertial forces (Figure 2.9, d). The throughput is in principle unlimited and large populations can be analysed to identify rare cells or just with the aim of mechanical characterisation (Otto et al., 2015).

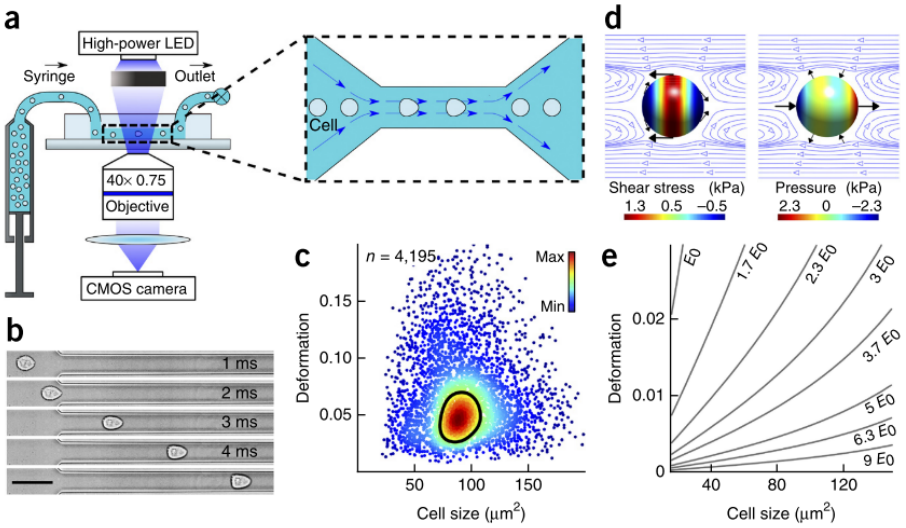

Figure 2.9: Illustation of the set-up (a), images of a cell flowing through the channel (b) scatter plot of deformability versus area (c), pressure and shear stress fields acting on sphere (d) and isoelasticity lines (e). Adapted from (Otto et al., 2015).

A detailed description of the protocol of these experiments is given in (Herbig et al., 2018) with relevant aspect such as the ratio of cell to channel cross section (cell diameter should be 30–90% of the channel width to reach a detectable deformation), flow rates for each channel size and focusing conditions to obtain optimal postprocessing. An analytical model valid for very low Reynolds numbers allows to decouple cell size and deformability: larger cells have their membrane closer to the walls and experience

a high shear. Combining a hydrodynamic model that derives the pressure distribution on a sphere (cell) and liner elasticity theory for elastic spheres, isoelasticity lines can be derived and objects lying on such lines have the same stiffness independently of their size (Figure 2.9, e).

An interesting work coupled the experimental images on Jurkat cells flowing through a $50\mu m$ x $50\mu m$ channel with numerical simulations using the liquid compound drop model: the cell membrane is assumed with zero thickness and cytoplasm is a shear thinning fluid with a stiffer drop inside resembling the nucleus (Tatsumi et al., 2014). Besides establishing a comparison between experimental and computational data, the authors pinpointed the role of the nucleus position on deformation modes of lymphocytes, observing a more pronounced bullet shape if nucleus locates on the trailing side (Figure 2.10, bottom). As noted also in the works cited above (Otto et al., 2015) (Herbig et al., 2018) a sheath flow is necessary to confine the cell stream in the centre of the channel (See "side inlets" in Figure 2.10, top).

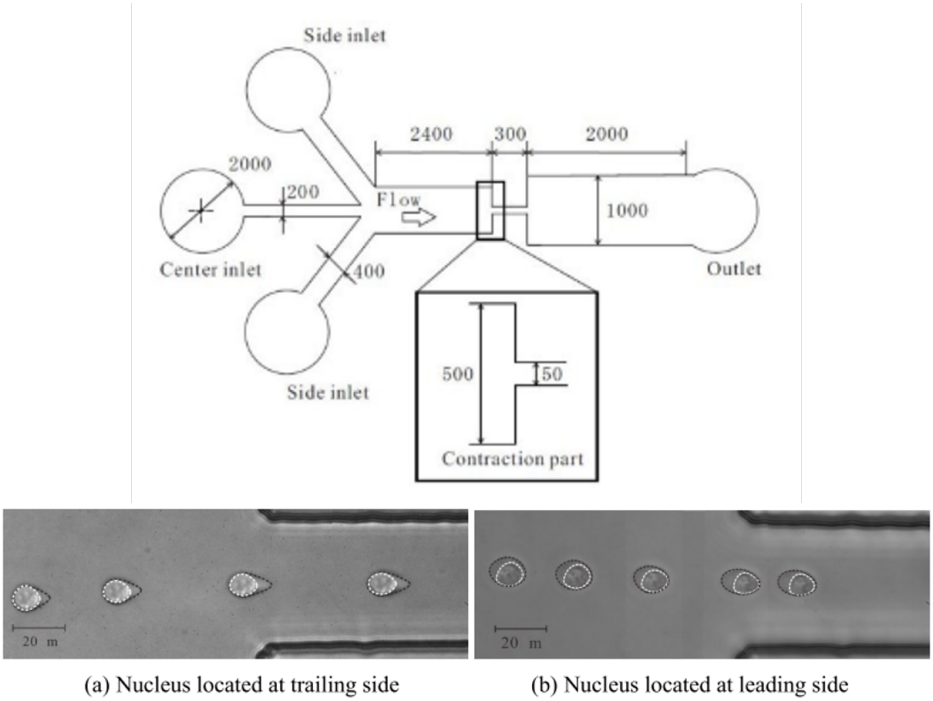

Figure 2.10: Representation of the channel geometry (top) and snapshots of cell flowing through the channel with different nucleus positions resulting in different deformation modes (bottom). Adapted from (Tatsumi et al., 2014).

Another group employed a straight microchannel of $15\mu m$x$10\mu m$ cross section to separate malaria infected from healthy red blood cells based on the principle of leukocyte margination: softer small red blood cells are brought to the centre of the channel where the flow velocity is maximum, whereas stiffer big white blood cells migrate towards the wall (Hou et al., 2010).
It is important to point out that in a straight channel of rectangular (or square) cross section, a nearly parabolic velocity profile develops, since the laminar regime is maintained for a wide range of flow rates at the microscale and for low aspect ratio the original solution of the velocity profile can be simplified to the well known Poiseuille flow. This yields a constant maximum velocity along the channel length for a given flow rate, which intuitively suggest that fluid induced forces on the cell will be constant along the channel length.

Cross slot channels

A quite different approach has been embraced by other groups that focused their attention on the mechanical behaviour of cells under a type of flow known as extensional: unlike the shear flow this features no vorticity and a stagnation point where the velocity reaches zero. A common shape to produce such pattern is the cross, with two perpendicular intersecting channels giving two inlets and two outlets. When flow is directed into the opposing inlets, fluid exits at 90° through the outlets. This establishes a planar extensional flow with a stagnation point – a point of zero velocity – centred at the channel intersection. At the stagnation point, cells experience compression along the inflow axis and extension along the outflow axis (Figure 2.11) and the maximum strain rate is experienced.
For the cross slot geometry to work efficiently, a focusing mechanism is needed to bring the cells at the centre of the channel cross section, to avoid low throughput and uncertainty in the measurements given by the the unlikelihood to find cells exactly at the stagnation point and by heterogeneity of trajectories, respectively (Cha et al.,

2012). While some works exploited inertial focusing through serpentine channels to align cells along the centreline (Figure 2.11, B) others made use of viscoelastic solutions like polyethylene glycol (Guillou et al., 2016) or polyvinylpyrrolidone (Cha et al., 2012).

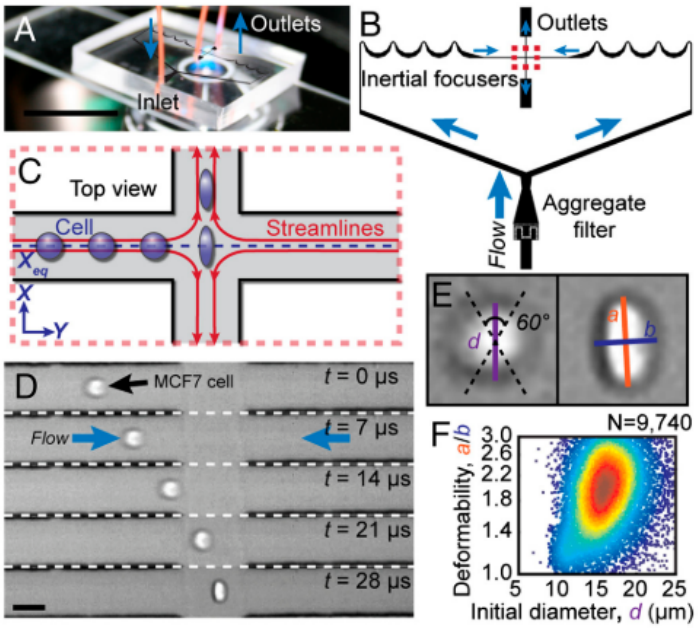

Figure 2.11: Cross slot deformability cytometer (A) with inertial focusing mechanism (B), detail of the cross (C), bright field images from high speed recording of a cell stretched in the stagnation point (D) and resulting measured deformability (E) represented in a scatter plot versus the diameter of non deformed cells (F) (Gossett et al., 2012).

Since cells typically assume an elliptical shape when subjected to this type of flow, many have individuated in the ratio between long and short axis of the ellipse an effective descriptor of the deformability (Figure 2.11, C and E). A very high throughput can be reached, with large populations of cells analysed and detection of rare malignant cells in pleural fluids (Tse et al., 2013), prediction of disease in cancer patients and pluripotent stem cells differentiation state pluripotent or differentiated embryonic stem cells (Gossett et al., 2012) and multiparametric mechanical screening (Masaeli et al., 2016).

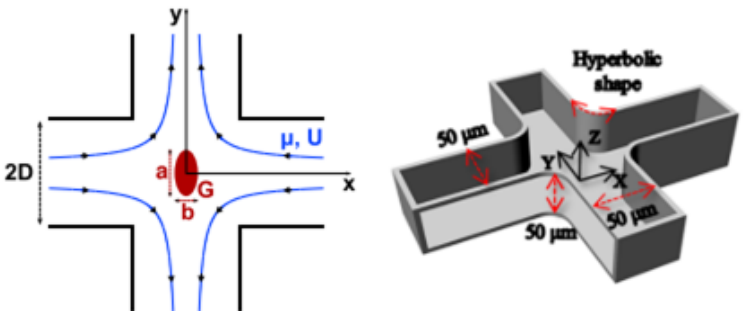

Figure 2.12: Straight walls cross slot device with streamlines depicted in blue (left, adapted from (Guillou et al., 2016)) and hyperbolic side walls cross (right, adapted from (Cha et al., 2012)).

A modification of the geometry to follow the streamlines was also proposed to homogenize trajectories, with equilateral hyperbolae as side walls of the cross instead of vertical and horizontal branches (Figure 2.12).

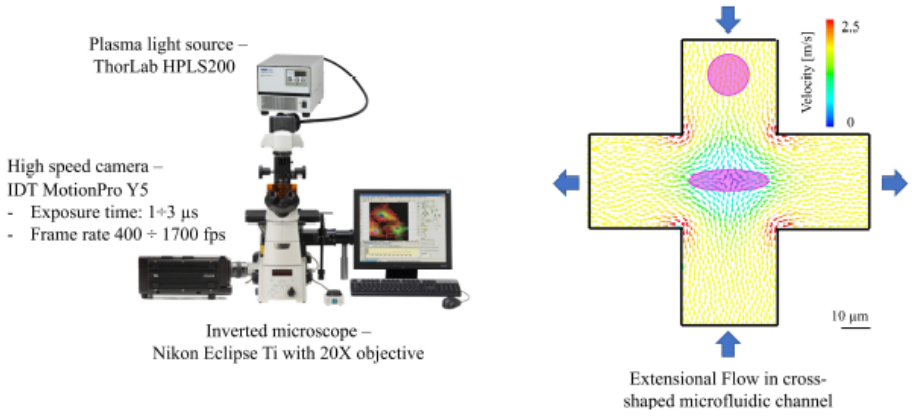

Figure 2.13: Experimental set up for high speed recording of cells flowing in the cross shaped device (left) and representation of the velocity vectors with the cell in initial and deformed configuration (right) (Piergiovanni, 2018).

In a previous work in our group, the deformation of human leukaemia cell lines (HL60 and Jurkat) in a cross slot device was measured experimentally to validate a volume of fluid computational model (Figure 2.13). Considerable stresses were delivered to cells by applying high flow rates and a high speed recording system was used to collect video recordings of the cells travelling at considerable speed (Piergiovanni, 2018).

Hyperbolic channels

The other shape that provides a constant extensional rate along the centreline is the hyperbolic converging channel. Despite the theory was first demonstrated for axisymmetric geometries (Feigl et al., 2003), adaptation to rectangular cross section channels with low aspect ratio is deemed as a good approximation.

An important drawback of the cross shaped device is the non-uniformity of extensional rate (there do not exist two different positions where the extensional rate is the same) and the fact that the deformation of cells at the stagnation point is a very fast, instantaneous process: in contrast, the linear increase in the axial velocity in the hyperbolic channels yield a constant extensional rate.

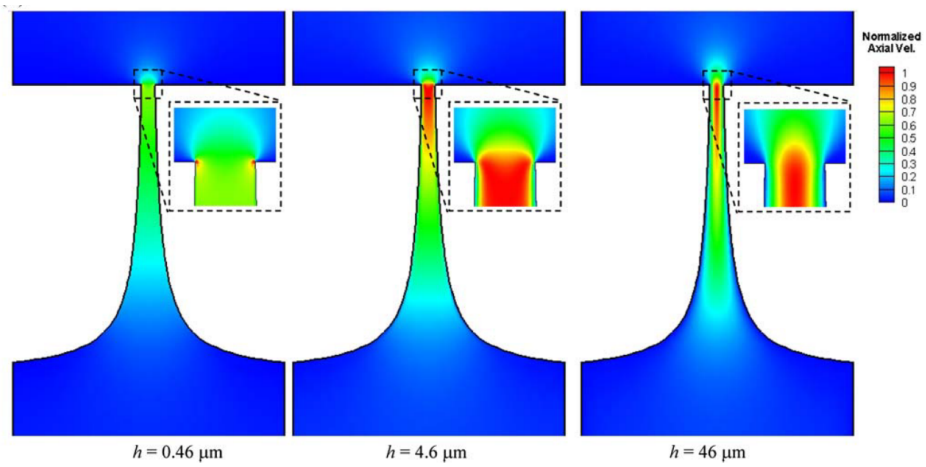

Figure 2.14: Effect of the device height h on the velocity field in a hyperbolic microchannel (Oliveira et al., 2007).

Hence, many works in literature report the study of cells stretching along a hyperbolic converging microchannel (Yaginuma et al., 2013)(Rodrigues et al., 2016a). In these works, a definition of the degree of stretching induced on the probed objects is found as the Hencky Strain ε_H (Ober et al., 2013):

$$\varepsilon_H = \int_0^t \dot{\varepsilon_a} dt = \ln \frac{w_u}{w_c} \tag{2.1}$$

where ε_a is the apparent extensional rate given by

$$\dot{\varepsilon_a} = \frac{Q}{L_c h}\left(\frac{1}{w_c} - \frac{1}{w_u}\right) \tag{2.2}$$

Such shape has also been employed in microfluidic extensional rheometry (Oliveira et al., 2007), with detailed fluid dynamic simulations of the flow pattern for different geometrical conditions (Figure 2.14) and for rheological characterization of blood analogues (Sousa et al., 2011). As mentioned above (see Biological background) research has been mostly focusing on red blood cells: different studies report their deformability under homogeneous extensional flow (Lee et al., 2009) in contact with magnetic nanoparticles (Rodrigues et al., 2016a) or with cancer cells (Faustino et al., 2014). Others have exploited the hyperbolic contraction - sudden expansion shape to increase the cell free layer downstream for blood separation purposes (Rodrigues et al., 2016b) (Calejo et al., 2016).

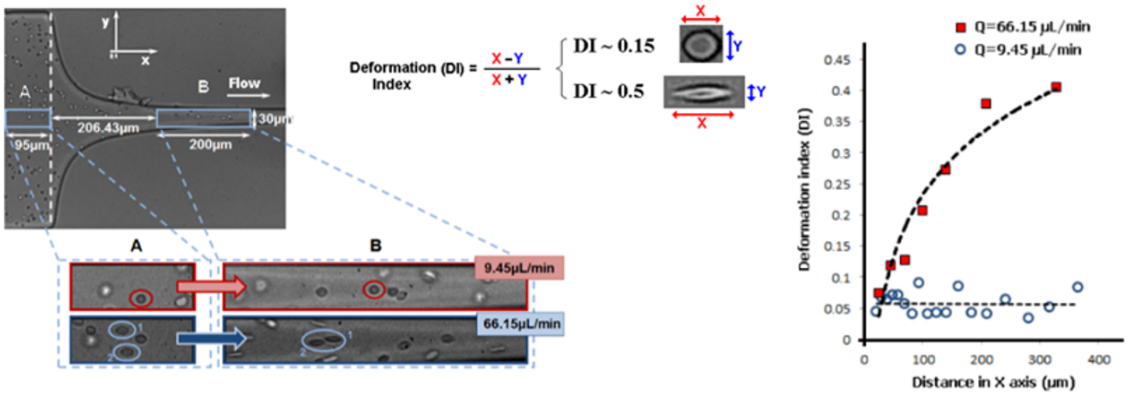

Figure 2.15: Bright field images of red blood cells deforming in a hyperbolic converging microchannel (top left), representation of the deformability calculation (here "deformation index", top right), deformation index and linear velocity along the channel (bottom) (Bento et al., 2018).

A key point of these studies is the establishment of a linearly increasing axial velocity along the centerline of the hyperbolic region, resulting in a constant extensional rate (derivative with respect to the axial direction).

Deformability has been often defined as the ratio:

$$DI = \frac{\text{long axis - short axis}}{\text{long axis + short axis}} \tag{2.3}$$

with axes belonging to an ellipse fitting the stretched cell (Figure 2.11, F) and has shown to be increasing with the flow rate (Figure 2.15). Another group has shown the effectiveness of extensional flow in deforming red blood cells as compared to simple shear: larger deformation indexes were observed for cells flowing through a hyperbolic channel as compared to experiments in a Couette device at physiologically relevant stresses in human vessels (Lee et al., 2009). Also in this case, a complementary fluid dynamic analysis showed the velocity pattern along the hyperbolic channel and the linear increase in velocity (Figure 2.16).

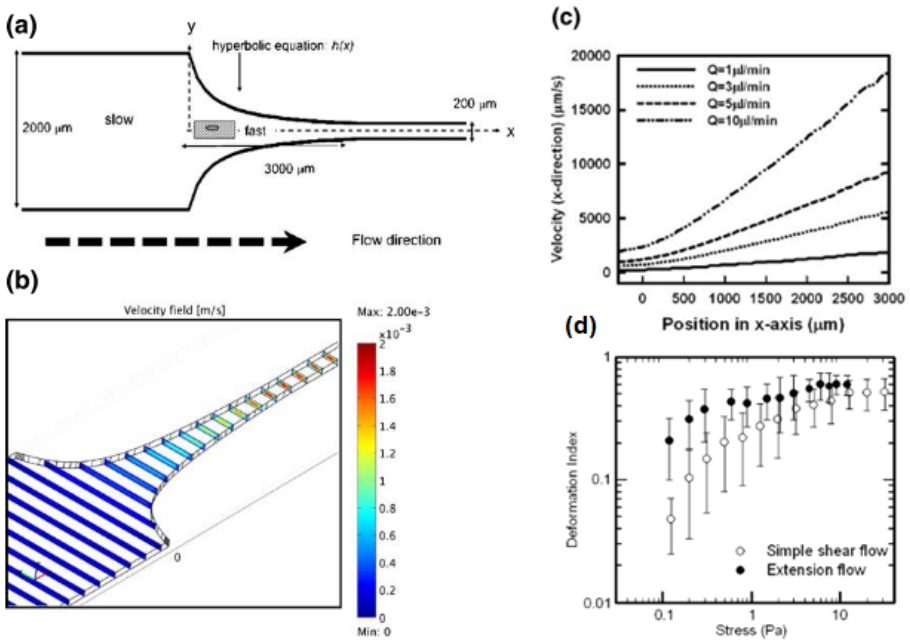

Figure 2.16: Sketch of the hyperbolic channel for red blood cells deformability assessment (a), with velocity field from numerical simulations (b), linear increase in axial velocity (c) and comparison of deformability under shear and extensional flow (d). Adapted from (Lee et al., 2009).

As previously mentioned, the hyperbolic shape allows for a continuous observation of deformability as the cross section shrinks, where the degree of stretching given by the

increasing velocity can be appreciated (Figure 2.17). This is of great interest because, unlike the case of the cross shaped channel which gives an instantaneous information, here time dependent deformation and recovery can be inferred.

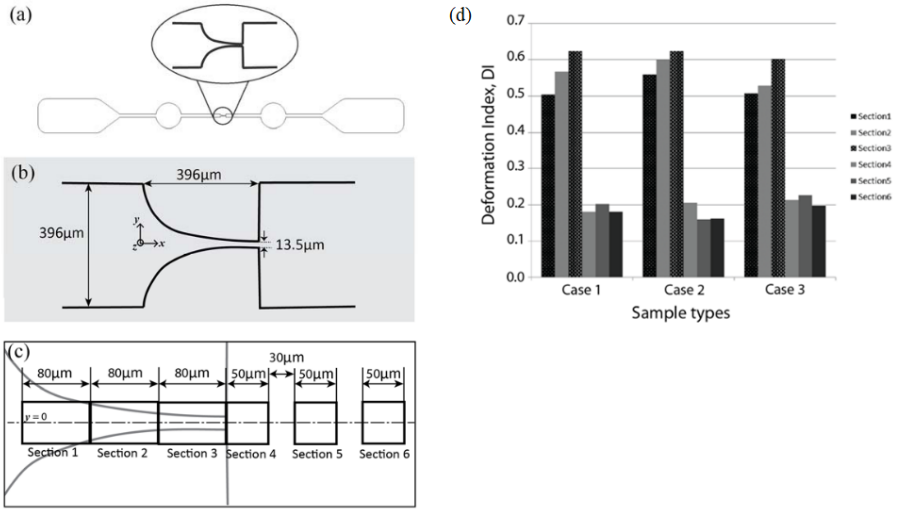

Figure 2.17: Sketch of the hyperbolic channel for red blood cells deformation assessment (a), zoom on the channel part (b), linear increase in axial velocity (c) and comparison of deformability under shear and extensional flow. The deformation index in three different cases is reported, and regardless the case DI increases until section 3 (constriction) and drops in correspondence with the ri-expansion (d). Adapted from (Faustino et al., 2014).

Interestingly, some exploited cell stiffness as a means to separate rigid white blood cells from softer red blood cells, developing a device that featured both cross flow filtration and sequences of hyperbolic channels to assess deformability upon separation of WBCs from erythrocytes (Rodrigues et al., 2015). WBCs clearly show a much lower deformability with respect to red blood cells when subjected to extensional flow and a less evident drop in the detected deformability in correspondence with the ri-expansion (Figure 2.18).

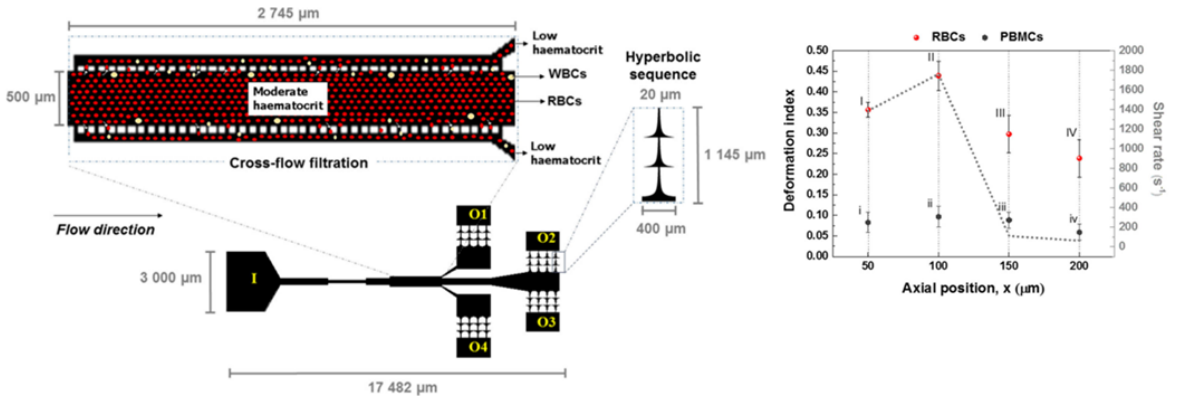

Figure 2.18: Cross flow filtration device with white blood cells retained in the main stream and series of hyperbolic channels at the outlets to measure the deformability index of red blood cells and peripheral blood mononuclear cells (PBMCs): overview of the platform (top) and DI of red blood cells and PBMCs along the hyperbolic channels (bottom). Adapted from (Rodrigues et al., 2015).

From the works cited above, it appears that, despite the acknowledged utility of white blood cells and cancer cell deformability characterization, there is a lack of investigation on these cell lines, especially with respect to red blood cells. Further, the use of the hyperbolic shape has proven successful in inducing high deformation thanks to a mixture of shear and extensional flow. For these reasons, a hyperbolic converging microchannel was used to assess the deformability of immortalized cell lines from human leukaemia to gain insight on the behaviour of a "standard" nucleated cell that features a deformation mode well far from the extensively studied erythrocytes.

Materials and Methods

3.1 Description of the investigated geometries

The geometry selected for the design of the channel was a symmetric hyperbolic contraction with the following characteristic dimensions (Figure 3.1): upstream width (w_u), contraction width (w_c), length of the hyperbolic region (L_c), and height of the device (h). In previous works on hyperbolic shaped channels, a definition of the degree of stretching induced by such shape is found as the Hencky Strain ε_H (see Eq. 2.1 in State of the art) that depends only on geometrical features: a larger strain is obtained when increasing the ratio between upstream and contraction widths. Here, the upstream width w_u was kept constant and three different contraction widths were chosen (Table 3.1).

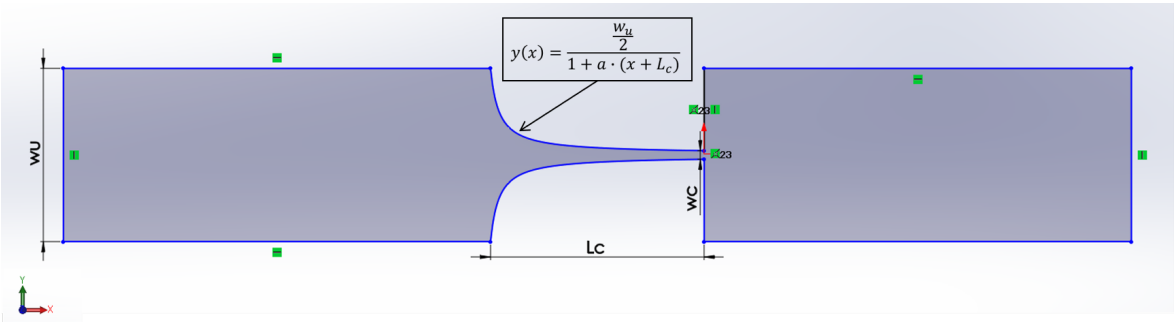

Figure 3.1: Sketch of the core hyperbolic geometry.

$w_u[\mu m]$	$w_c[\mu m]$	$\varepsilon_H[-]$
400	15	3.28
400	20	3.00
400	25	2.77

Table 3.1: Channel sizes and corresponding Hencky strains.

The channel length was also varied, and to get a difference that could be experimentally detectable, lengths of $500\mu m$ and $1000\mu m$ were chosen. The height of the device was kept constant at $h = 20\mu m$ since from the first experimental trials it was readily understood that a taller channel caused too much difficulty for the focusing in the z direction. Table 3.2 summarizes the six different channels that were used

throughout the work.

The equation of the hyperbola (also reported in Figure 3.1) is the following:

$$y(x) = \frac{\frac{w_u}{2}}{1 + a \cdot (x + L_c)} \tag{3.1}$$

with a defining the curvature which slightly varies based on the constriction width w_c: this can be easily obtained by calculating the value in the origin of the coordinate system that lies on the contraction, hence $y(0) = \frac{w_c}{2}$ and

$$a = \frac{1}{L_c} \cdot \left(\frac{w_u}{w_c} - 1\right) \tag{3.2}$$

with six different values of a found by varying w_c and L_c in the six cases, meaning the hyperbolae have slightly different curvatures one with respect to the other, maintaining the desired length and width at the contraction.

A cross section of such size was fairly larger than both cell lines (Table 3.3) with no contact between cells and channel walls in any of the experiments, even with the smaller width ($w_c = 15\mu m$). Furthermore, it is suggested in the literature that the cell diameter should cover 30% to 90% of the channel size to obtain a deformation large enough to be measured (Herbig et al., 2018) (Urbanska et al., 2018).

$w_u[\mu m]$	$w_c[\mu m]$	$L_c[\mu m]$	$h[\mu m]$
400	15	500	20
400	20	500	20
400	25	500	20
400	15	1000	20
400	20	1000	20
400	25	1000	20

Table 3.2: Dimensions of the six hyperbolic channels.

For sake of comparison with literature data and evaluation of the difference among different shapes, an additional geometry consisting of a straight channel was investigated (Figure 3.2): the height was still $20\mu m$ for the same reason as above, the

width$w_c = 20\mu m$ and the length $L_c = 300\mu m$.

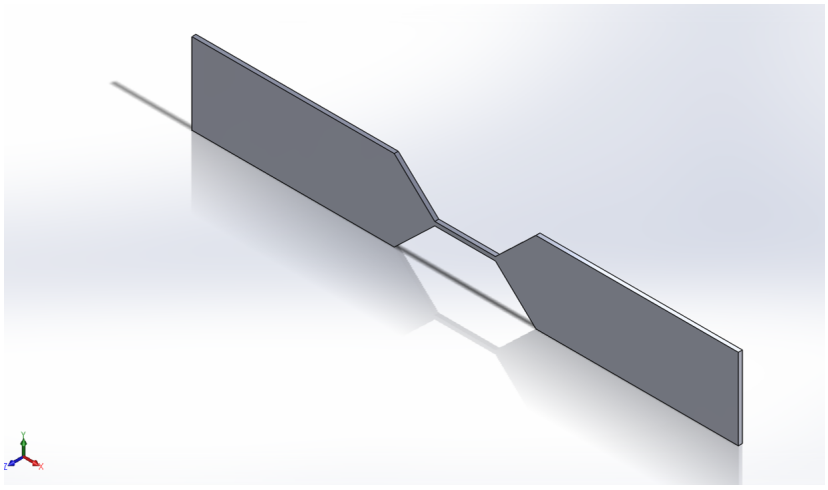

Figure 3.2: Geometry with the straight channel.

Few experiments and simulations were also performed on a cross shaped channel with $20\mu m$ x $20\mu m$ cross section to relate the results to the findings obtained in a previous work in our group (Piergiovanni, 2018). The details abut this channel are presented in Appendix B.

3.1.1 Final geometries

A further development of the geometry consisted in the addition of a sheath flow system, necessary for the focusing in the 2D plane (XY plane) as assessed from the first experiments. Therefore, the new geometry featured another inlet splitting into two branches that merged together with the original inlet and were long enough to allow fully developed flow and effective 2D focusing (Figure3.3).

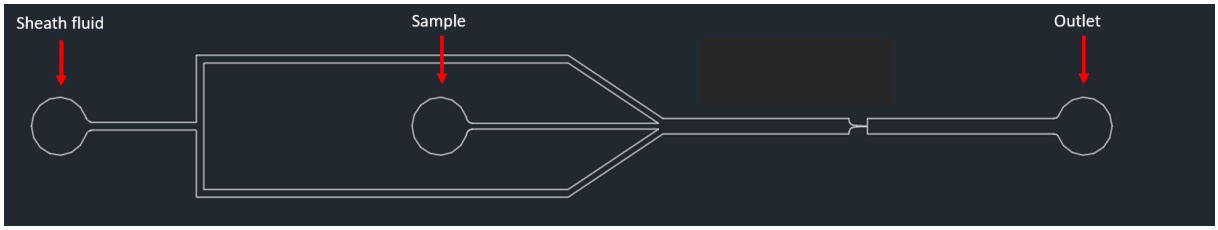

Figure 3.3: Geometry with sheath fluid system, with sheath inlet, sample inlets and outlet indicated (drawing realized in AutoCAD).

Moreover, due to frequent clogging of the channels, especially of the ones with the smallest width at the contraction ($w_c = 15\mu m$), two filtering units were added at the inlets (Figure 3.4). As commonly operated in microfluidics, a convenient way to filter out dirt in the channels is the use of progressively closer pillars: to avoid an increase in hydraulic resistance the section was enlarged (from 250 to $1770\mu m$). The minimum gaps between pillars were $10\mu m$ and $20\mu m$ (larger than the tested cells diameter, reported in Table 3.3) for the sheath fluid inlet and the sample inlet respectively.

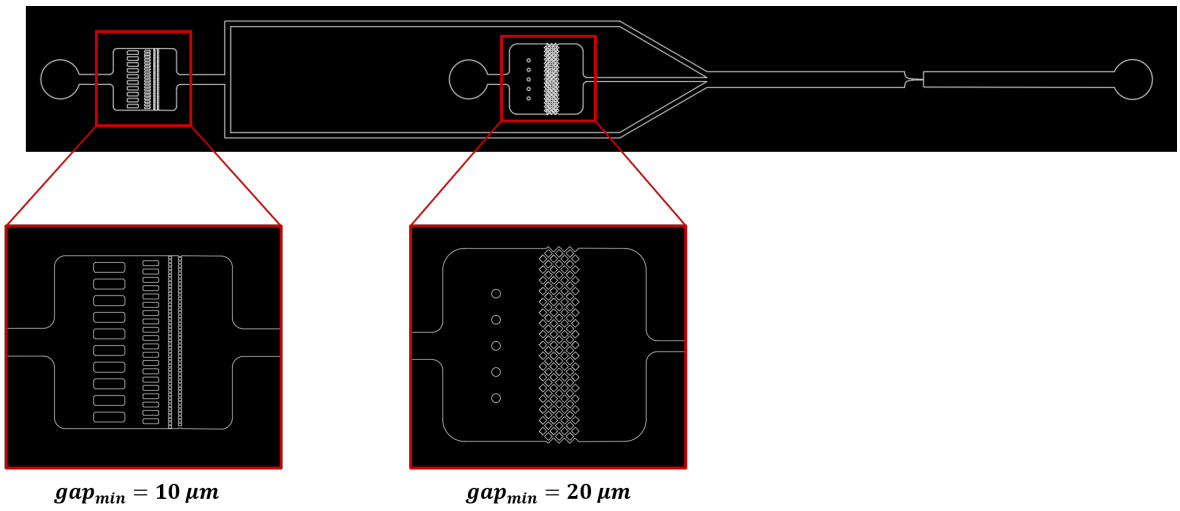

Figure 3.4: Final geometry with the sheath fluid system and the filtering units at the inlets (drawing realized in AutoCAD).

	Jurkat	**HL60**
diameter $[\mu m]$	11.5 ± 1.5	12.4 ± 1.2

Table 3.3: Size of the two tested cell lines as reported from data sheets (Milo et al., 2009).

3.2 Experimental campaign

3.2.1 Fabrication of the microchannels

All the devices were fabricated using standard soft lithography techniques: Poly Dimethil Syloxane (PDMS, Sylgard 184, Dow Corning) was prepared in a 10:1 ratio (polymer to crosslinker) mixed at 3000 rpm for 30 seconds, poured onto SU8 reusable moulds and baked in oven at 70°C for at least two hours. The moulds were made in a clean room with SU8 photoresist on silicon wafers with standard photolithography. For the schematization of the whole soft lithography process see Figure 2.6 in 2).
Upon baking, the chips were carefully peeled off the wafer, then cut and punched with a 22 gauge needle (i.e. 0.644 mm, matching the size of the metallic pins to be inserted in the inlets); eventually they were attached via plasma bonding to glass cover slips (thickness 0.13 to 0.16 mm). This support is more delicate to handle and more fragile with respect to glass slides (thickness $\sim$ 1 mm) but provided a slightly better image quality, that, as mentioned above (see Introduction), was a crucial part if considering that the evaluation of the deformation was based on optical images. Figure 3.5 shows one of the chips bonded to a coverslip.

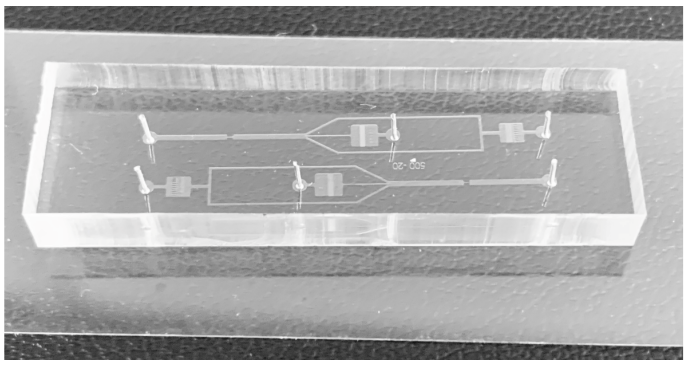

Figure 3.5: Picture of one of the microfluidic chip with two counter facing channels.

To improve the silicone to glass bond strength and to make sure to remove any dirt from the coverslips, these were left soaking in a very diluted KOH solution, which

rendered their surface hydrophilic. Before bonding, the KOH was carefully washed out of the coverslips under deionized water and they were thoroughly dried. This additional step is not common in routine microfabrication but significantly improved the bonding between the PDMS chips and the glass coverslips, which was crucial especially at the high pressures applied in some conditions.

3.2.2 Working fluids

For the sheath flow system to work optimally, sheath fluid and sample should have the same properties (density and viscosity), hence the same buffer was used for the sheath system and for the cell suspension.

The first experiments were performed with Phosphate Buffer Saline (DPBS, Life Technologies, Switzerland) but two main issues arose, namely rapid sedimentation of cells in the syringe (every few minutes this had to be turned upside down to redistribute cells evenly in the suspension) and the high flow rates needed to obtain a detectable deformation (with consistent pressure applied at the inlet connections). Sedimentation could be prevented by adding OptiPrep density gradient medium (Sigma-Aldrich, Switzerland) which is, however, extremely expensive, but still the high flow rates resulted in too high velocity and images of insufficient quality, with pronounced motion blur at the contraction.

The simplest way to overcome these limitations is the use of more viscous fluid: as found in literature (Otto et al., 2015) (Herbig et al., 2018), the addition of a biocompatible long chain polymer - Methylcellulose (Sigma Aldrich, Switzerland) - could provide a high density viscous fluid with shear thinning behaviour. The elevated density limited sedimentation and viscosity promoted higher stresses on the cell with much lower flow rates; as noted in a study aimed at investigating 3D particle focusing, the use of a shear thinning fluid was observed to facilitate the migration of cells towards the centre of the channel (Del Giudice et al., 2017), greatly beneficial in this case for the focusing

in the z direction.

Three different buffers were used, varying the concentration of methylcellulose (MC) in phosphate buffered saline (PBS):

- Buffer 0.25: PBS + MC 0.25% w/ (low viscosity);
- Buffer 0.37: PBS + MC 0.37% w/v (intermediate viscosity);
- Buffer 0.50: PBS + MC 0.50% w/v (high viscosity)

where w/v indicates the concentration as weight (g) over volume (ml). Buffer 0.37 was used in few experiments to see whether there existed a detectable difference in deformation even with a slighter change in viscosity.

All buffer samples were prepared by mixing Methylcellulose powder in PBS on a magnetic rotatory mixer for at least 24 hours. For such low concentrations, heating was not necessary to ensure mixing and also advised against by the manufacturer (Sigma Aldrich, Switzerland).

Buffer 0.50 was already described in the literature (Herbig et al., 2018), whereas Buffer 0.25 was characterized with a Couette rheometer (Antoon Paar, Austria) and the experimental results were fitted with a power law model (Figure 3.6). The model equation and calculated indices are explained later in this section (Eq. 3.4 in 3.3). The aim of a more viscous fluid was to lower velocities and obtain better images with reduction of motion blur; to limit the increase in pressure on the connections and on the bonding between PDMS and glass coverslip chip due to the increased viscosity, lower flow rates needed to be set in such case (Table 3.4).

Buffer 0.25	**Buffer 0.37**	**Buffer 0.50**
$Q = 10\frac{\mu l}{min}$	$Q = 5\frac{\mu l}{min}$	$Q = 0.6\frac{\mu l}{min}$
$Q = 15\frac{\mu l}{min}$	$Q = 7\frac{\mu l}{min}$	$Q = 1.2\frac{\mu l}{min}$
$Q = 20\frac{\mu l}{min}$	$Q = 10\frac{\mu l}{min}$	$Q = 1.8\frac{\mu l}{min}$
$Q = 25\frac{\mu l}{min}$	$Q = 12\frac{\mu l}{min}$	$Q = 2.4\frac{\mu l}{min}$
	$Q = 15\frac{\mu l}{min}$	$Q = 3.6\frac{\mu l}{min}$

Table 3.4: Sample flow rates for each buffer. The respective sheath flow rates are simply scaled by three ($Q_{sheath} = 3 \cdot Q_{sample}$) so that the total flow rate is $Q_{tot} = 4 \cdot Q_{sample}$.

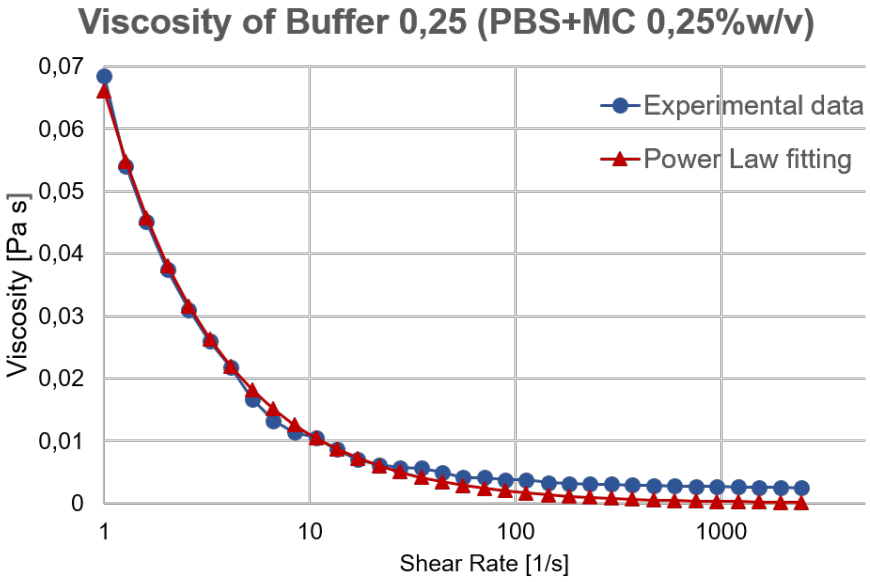

Figure 3.6: Power law model fitting for the shear thinning Buffer 0.25.

For Buffer 0.25, fifteen milliliters of fluid were prepared (to ensure enough buffer for both cell suspension and sheath fluid at high flow rates), whereas for buffer 0.50 and Buffer 0.37 a quantity of ten milliliters was sufficient.

3.2.3 Cells

In this work, two different cell lines were used to assess whether a difference in the mechanical properties could be detected: the leukaemia derived cell lines, namely HL60 (from acute myeloid leukaemia) and Jurkat (from acute lymphoid leukaemia). These are relatively easy to handle as they are immortalized cell lines thus remarkably robust also after many passages and they can fairly resemble the behaviour of a generic eukaryotic cell in terms of mechanical properties, especially considering the difference with respect to red blood cells.

HL60 and Jurkat cells were thawed with the standard protocol and resuspended and cultured in Gibco RPMI 1640 Medium (ThermoFisher Scientific, Switzerland) supplemented with 10% Fetal Bovine Serum and 1% PenStrep - a mixture of Penicillin Streptomycin ThermoFisher Scientific, Switzerland) - and put inside standard poly-

styrene flasks. Flasks were kept in the incubator at 37 °C, partial pressure of CO_2 5% (corresponding to the one measured in tissues, 35-45 mmHg) and 95% humidity (Galaxy 170s, Eppendorf, Germany); the cells were split and the medium refreshed every two days. During the first week after thawing three different concentrations were kept (1:5, 1:10, 1:20) to ensure at least one good condition, being cells more sensitive after the thermal shock and great stress undertaken. Afterwards, a concentration of about 1:20 was kept for both cell lines.

Both were observed to aggregate in clusters during culture: these clumps were broken by gently pipetting them upon medium refreshing (in such case care must be taken to cause the minimum possible shear on cells, hence using a large pipette and slow suction and expulsion). Both cell types tended to adhere to the bottom wall of the flask but could be detached just by gently hitting the flasks (since they do not have an adherent phenotype they simply deposited by gravity on the bottom of the flask). These cell lines were found to be quite robust and very few cells revealed apoptotic or dead when observed through a bright field microscope at different magnifications.

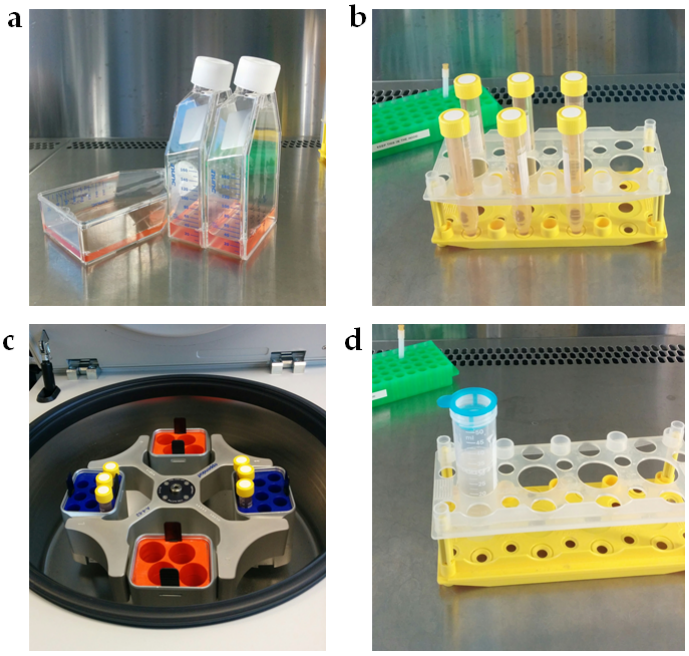

Figure 3.7: Steps in the sample preparation: cells from 75ml polystyrene flasks (a) were put in 15ml falcon tubes (b), centrifuged (c) and washed and filtered trough a strainer (d).

3.2.4 Sample preparation

The cell suspension was prepared with the same protocol for each experiment. The main variability between samples taken on different days was cell concentration in the flasks, which was generally kept high to provide for a consistent number of cells needed for experiments. Concentration could be easily estimated by naked eye looking at the colour of the flasks content: red phenol in the growth media is an index of metabolic activity, turning to yellow with acidification of the environment when cells grow and expand. A pink to violet colour of the flask is instead an indicator of poor cell grow and health. Another quick visual evaluation could be obtained by microscopy observation of the flasks, which was also important to check the presence of clusters or apoptotic phenomena.

Figure 3.8: Haemocytometer for cell counting (top): few microliters of the solution containing cell suspension and trypan blue were put under the glass slide with the aid of a precision pipette (bottom) for subsequent observation in bright field microscopy.

A suboptimal concentration could result in excessive apoptotic phenomena, easily detected by the presence of ruptured membranes and granules of lysed cell parts around. An estimation of the concentration could also be obtained by manual cell counting with a haemocytometer (Neubauer Improved Brightline, Germany): a mixture of cell

suspension and Trypan Blue (Thermofisher Scientific, Switzerland) was put onto a the chamber of known area and height under a thin glass slide (Figure 3.8) and cells were observed and counted in bright microscopy, usually with a 10X objective. Dead cells could be distinguished from alive ones by observing their colour: strongly blue appearing cells were dead as they had taken up the dye which alive cells are usually impermeable to.

For the preparation of each sample, the cell suspension was transferred from flasks to 15 ml falcon tubes and centrifuged at room temperature for 5 minutes at 120 rpm (18g). Supernatant was aspired and the cell pellet was washed with PBS to be subsequently filtered with a $40\mu m$ strainer in a 50 ml falcon tube. the filtered suspension was then centrifuged again to remove PBS and finally resuspended in the desired amount of buffer (Figure 3.7). The final sample volume depended on the buffer (hence flow rates) used:

- 2 to 3 ml or Buffer 0.25;
- 1 ml for Buffer 0.37;
- $500\mu l$ for Buffer 0.50.

All operations were conducted in a class 2 biosafety cabinet (Kojair Tech Oy, Finland).

Fixation

Cell fixation was performed with formalin 4%, obtained by the dilution of Formalin 36% (Sigma Aldrich) with PBS: after the first centrifugation, cells were resuspended in formalin, left for ten minutes and centrifuged again. To prevent cross linking between cells, they were washed with PBS with the addition of few millilitres of fetal bovine serum. A final centrifugation was performed, and the pellet was resuspended in Buffer 0.50 for measurements.

Cytochalasin D

Cytochalasin D (cytoD) is a cell permeable fungal toxin that binds actin and prevents its polymerization, having a great effect on the cytoskeleton (whose actin filaments constitute the major component) thus changing the membrane deformability. CytoD was purchased in form of pure powder (Sigma Aldrich) and resuspended in imethyl sulfoxide (DMSO) following the manufacturer's protocol.
Four different concentrations of the drug were used to assess the dose dependent response, with a tenfold step increase ($0.01\mu M, 0.1\mu M, 1\mu M$ and $10\mu M$). To avoid bias given by the presence of DMSO, the same percentage of with respect to the final sample was added: no more than 1% DMSO was recommended from the manufacturer due to the high toxicity at room temperature. The final samples were suspended in Buffer 0.50 hence 400 μl to 500 μl were prepared, with the addition of $4\mu l$ to 5 μl of cytoD+DMSO to the samples.
Four different solutions were prepared according to the desired final concentration in the sample and the desired amount of cytoD+DMSO was added to each sample as a last step (addition to the cells already resuspended in the buffer). The samples were incubated ten minutes to let the drug act prior to experiments.

3.2.5 Set-up

All the experiments were conducted with the use of an inverted microscope (Eclispe Ti-E, Nikon Instruments, Japan) connected to a high speed camera (MotionPro Y5, IDT vision, USA) and a syringe pumping system (neMESYS, Cetoni, Germany). A schematic representation and the real set-up are visible in Figure 3.9. For the first tests, a 10x objective (Nikon Instruments) was used to easily reach focusing in the z direction; then a 20X objective was preferred for a higher magnification despite the difficulty in focusing given by the lower depth of field. This can be estimated with the depth of field calculator provided by the manufacturer (Nikon) and it was readily clear

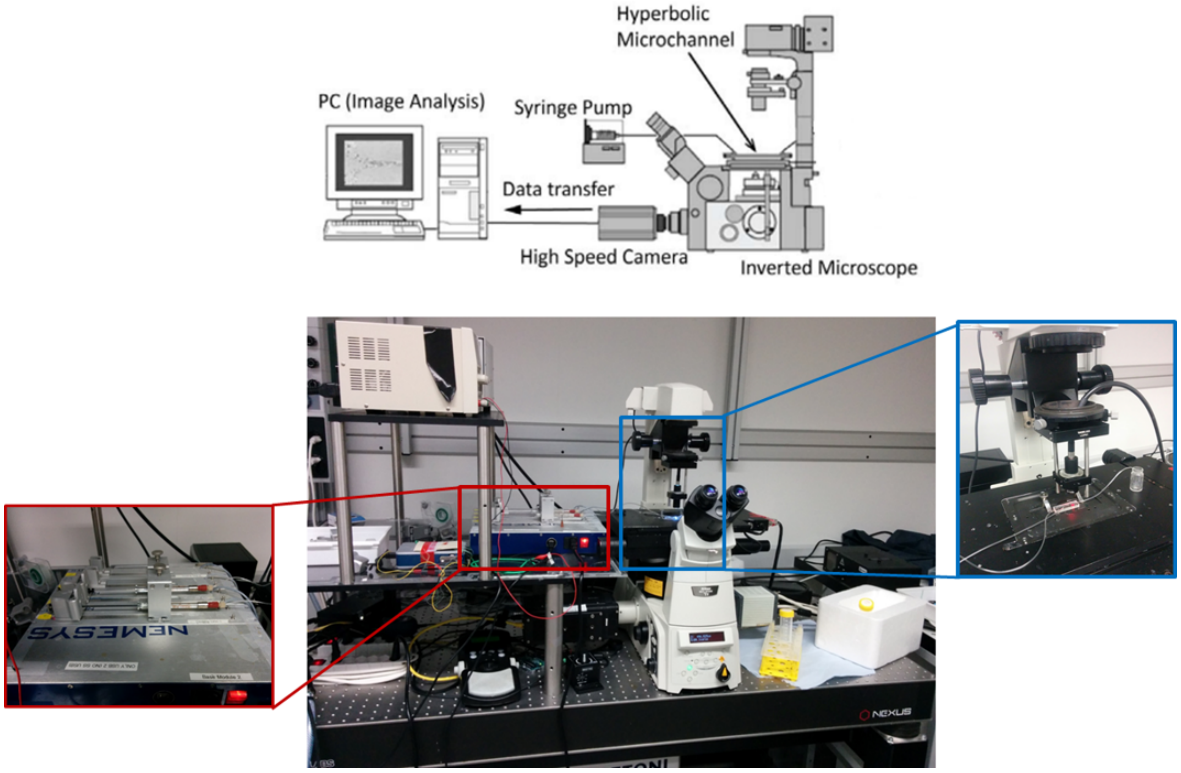

Figure 3.9: Experimental setup: schematic representation (top) and picture (bottom), with zooms on the syringe pump module (left) and on the chip mounted on the microscope stage with inlets and outlet connected (right).

that a higher magnification significantly reduces the depth of field - roughly of a factor three (Figure 3.10). Direct illumination was used to allow for maximum brightness after having set the camera parameters, since low exposure time and small region of interest significantly reduced brightness. Instead of using the standard lens systems, the optic fibre was put directly on the chip with the sole use of a focusing lens and a converging lens with a suitable support to align it with the objective (as visible in the detail of the chip in Figure 3.9).

3.2.6 Protocol for experimental tests

The same protocol was followed for all the experiments, with small adjustments for the different rheological conditions. Cell samples were prepared prior to each experiments and used right after, as nutrient depletion for cells kept in a buffer consisting

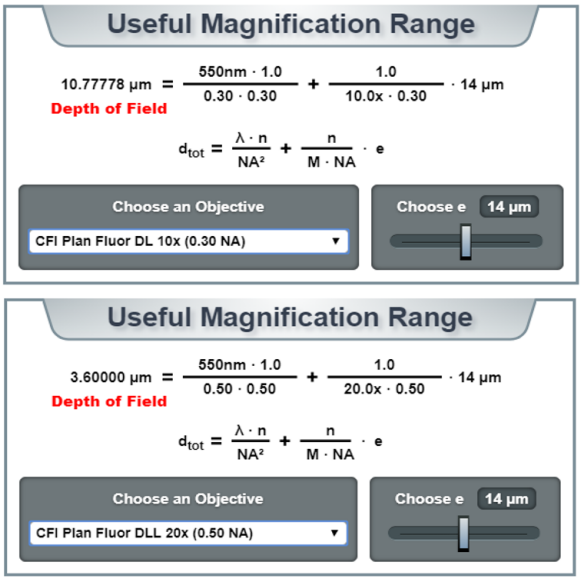

Figure 3.10: Depth of field for 10X and 20X objectives mounted on the inverted microscope as provided by the manufacturer (Nikon).

just of PBS and Methylcellulose for too long would have caused cell starvation. The cell sample and the sheath fluid were loaded in glass syringes (Hamilton, USA): 1 ml syringes were suitable for experiments with low and intermediate viscosity buffers (flow rates not lower than $5\frac{\mu l}{min}$) whereas smaller ones ($500\mu l$ or $250\mu l$) were more appropriate for experiments with the most viscous buffer (as minimum sample flow rate was $0.6\frac{\mu l}{min}$) to have the desired precision in dosage (see Table 3.4 for the complete flow rates values for each buffer).

Syringes were mounted on two of the four units of the pump and tightened with the dedicated screws to have firm positioning thus optimal control of the flow rate (Figure 3.9, detail of the syringe pump module at bottom left). The flow rates were controlled by the dedicated software on a computer connected to the set-up. Due to the presence of the tubes (approximately 20 cm, the minimum distance to reach the centre of the microscope stage where the chips were mounted) and to inertia of the pump, one to two minutes were necessary for the set flow rate to be reached and stable, thus each recording was taken after this time.

Metallic pins were inserted into the chip inlets and connected to tubes going to the

syringes containing the sample and the sheath fluid; the outlet tube was placed in a small eppendorf tube and appropriately disposed of at the end of experiments. Once mounted the chip on the microscope stage and found the plane of focus for the 20X objective, the light was turned on and controlled via its dedicated software (Lumencor, USA).

The high speed camera was used to record videos of the cells flowing into the channel at considerable velocity. The most important parameters that affected image quality were the time of exposure (t_{ext}) and the frame rate. The first indicates the amount of time at which the object is exposed to light: the faster the object travels, the lower the exposure should be, hence the lowest exposure time allowed by the camera was set ($t_{exp} = 1 \quad \mu s$). The second is the rate at which image frames are captured and saved, thus the higher this rate the better for subsequent image processing as a lot of images can capture cells in different positions of the channel and in progressive deformation states.

In turn, to enhance the frame rate a smaller area of observation (region of interest, ROI) can be imaged, thus a compromise between frame rate and ROI was sought. Since the sheath systems well confined the cells in the XY plane to a central band, the zone of interest was sufficiently narrow and allowed for a small ROI (Figure 3.11), yielding 10'000 frames per second. Ten thousand images were acquired as Audio Video Interleave (AVI) format (3 to 4 minutes) as 8-bit Tagged Image File Format (TIFF) images to be subsequently analysed with the aid of ImageJ software (National Institutes of Health, USA). In practice, a video was recorded for each condition tested, meaning each flow rate for each channel and both cell lines.

Troubleshooting

The first problem encountered was the clogging of devices with the smallest width at the contraction ($w_c = 15\mu m$), but it could be effectively solved by placing filtering units upstream of each inlet (Figure 3.4). However, this also implied that the channels

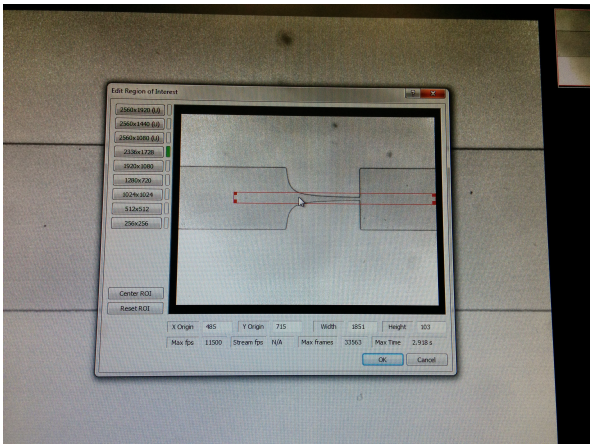

Figure 3.11: Setting of the region of interest on the camera for video recording: the ROI was 100 to 120 pixels high (36 to 44μm) and as large as the full screen width desired, since the frame rate just depended on the ROI height.

could not be reused: while in the first experiments the same channels could be cleaned by flushing Pluronic solution (Sigma Aldrich, Switzerland), this was not feasible after the introduction of the filters as, especially at low flow rates, cells inevitably accumulated around the pillars in the sample inlet and if the flow was stopped even for a small time, it was not possible to clean the channels entirely afterwards.

Moreover, it was not desirable to use the same chip for both cell lines to avoid contamination, thus a large quantity of PDMS chips needed to be manufactured. As mentioned in State of the art, one of the advantage of soft lithography is the re-use of the SU8 mould as a master for many times, so the production of more channels was not particularly time consuming, yet it could be addressed as a disadvantage of this type of microchannel as compared, for example, to geometries with large width that can be easily cleaned and do not cause any clogging.

Another issue in the tests was related to cell viability, as it was not possible to run experiments for more than about two hours, since the buffers did not contain any nutrients and cell starvation was inevitable. Apoptosis and death phenomena were observed few times, detectable by the presence of fragments and debris detaching from the cells, most likely due to membrane lysis (Figure 3.12).

Figure 3.12: Example of cells lysis observed in too long experiments: red arrows point at small debris with very irregular contours.

3.2.7 Image processing

All the images were processed by means of a Python code already present in the group that operated the following steps (Figure 3.13):

- Background calculation and subtraction: background was calculated as the arithmetic average of each pixel in a desired number of images from each folder (the higher this number, the more "accurate" the background image but the slower the processing);
- Bandpass filtering of the pixel intensity distribution: upper and lower thresholds were chosen depending on the image brightness, so for very dark image this band should be moved towards lower values and vice versa;
- Image smoothing: an open CV code for image blurring (cv2.medianBlur) was used to remove high frequency components such as edges and noise;
- Filtering: a combination of open CV binary and Otsu threshold were applied (the Otsu method is particularly useful in the case of bimodal images, meaning two main colours are present which means the pixel intensity histogram presents two separate peaks: the Otsu method automatically detects the separation of the two parts of the histogram so that the binary threshold then works efficiently on both);
- Erosion and dilation: these are standard morphological transformation applied to get smoother boundaries;
- Contour tracking: an openCV code to find contours was applied (cv2.findContours);

- Parameters calculations and saving: with regards to the detected contours, area, perimeter, width, height and x,y coordinates of the centroid were computed and saved in a Comma Separated Value (.csv) file.

It was very convenient to have all these quantities stored in an accessible format for subsequent display of the results by means of the R-Studio software.

a

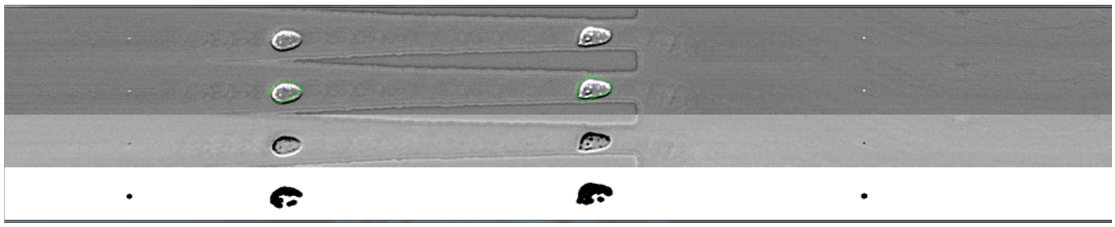

b

	A	B	C	D	E	F	G	H	I	J	K
1	Count	MaxIntensity	QuantilIntensity	Center x	Center y	Width	Height	Angle	Area	Perimeter	
2											
3	4	255	37	1903	56.5	70	51	0	2995	207.46	
4											
5	5	255	37	1934.5	56.5	65	55	0	2956.5	203.41	
6											
7	7	255	42	1975.5	56.5	63	59	0	2976.5	201.11	
8											

Figure 3.13: Representation of the image processing steps. The image shows the output of the code (top to bottom): raw image, contours, image downstream all the morphological operations and binary image.
The screenshot at the bottom shows the report of parameters in an excel file, with the ones of interest highlighted by red boxes.

3.3 Computational study

From the works discussed above (State of the art) it is evident that analytical models and simulations serve as useful means to evaluate the fluid dynamic characteristics of the devices and to model cell behaviour in a relatively simple way (mostly as liquid droplets with appropriate physical parameters).
As stated before (see Introduction), in this work several fluid dynamic simulations were performed in support of the experimental campaign, to assess the variation of the main parameters of interest (velocity, shear stress, extensional rate and pressure) in different geometrical and rheological scenarios.
The geometries were designed in SolidWorks and exported to ANSYS. The symmetry of the design allowed to study just half of it to cut computational effort (Figure 3.14). Since the final devices with the sheath system were almost 3 cm long, it was convenient to study the upstream sheath system and the channel part separately: a sufficiently fine mesh (with elements down to $2\mu m$ in size) with the whole geometry would have had millions of elements with a tremendous slow down on the simulations.
Therefore, a total of four geometries were meshed and used in simulations:

- upstream part (sheath flow system);
- straight channel, $L_c = 300\mu m$;
- short hyperbolic channel, $L_c = 500\mu m$;
- long hyperbolic channel, $L_c = 1000\mu m$

3.3.1 Geometry

Prior to the mesh construction, the geometry was manipulated in ANSYS Design Modeller by dividing the solid body with a set of slices along planes parallel to XZ and

YZ, both to reduce the domain to one symmetrical part (Figure 3.14) and to obtain a convenient partition for subsequent Cartesian meshing (Figure 3.15).

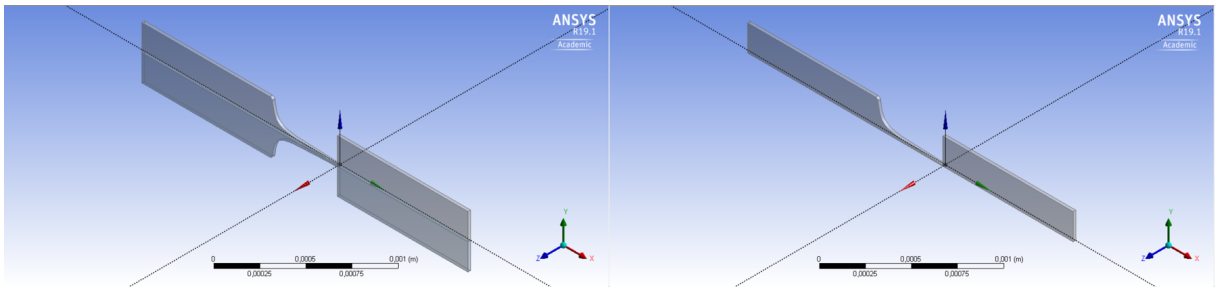

Figure 3.14: Splitting of the channel geometry on the plane of symmetry to reduce computational cost

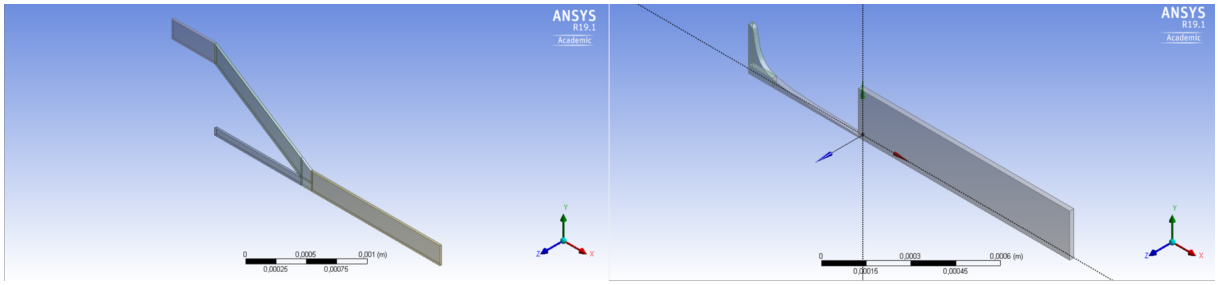

Figure 3.15: Splitting of the upstream (left) and channel (right) geometries for subsequent Cartesian meshing.

3.3.2 Mesh

ANSYS mesher was used to build a structured Cartesian mesh (hexahedral elements), as it is often deemed the optimal solution for simple geometries, providing maximum orthogonality, minimum skewness and high element quality. All these quality control parameters can be investigated in Ansys Mesher with visualization of elements according to the chosen parameter (e.g. the aspect ratio, as in Figure 3.17).
In the initial region of the hyperbola it was not feasible to construct a Cartesian mesh due to the pronounced curvature of the geometry, thus an unstructured mesh with minimum skewness and aspect ratio was chosen. An overview of the mesh of all the parts is shown in Figure 3.16.

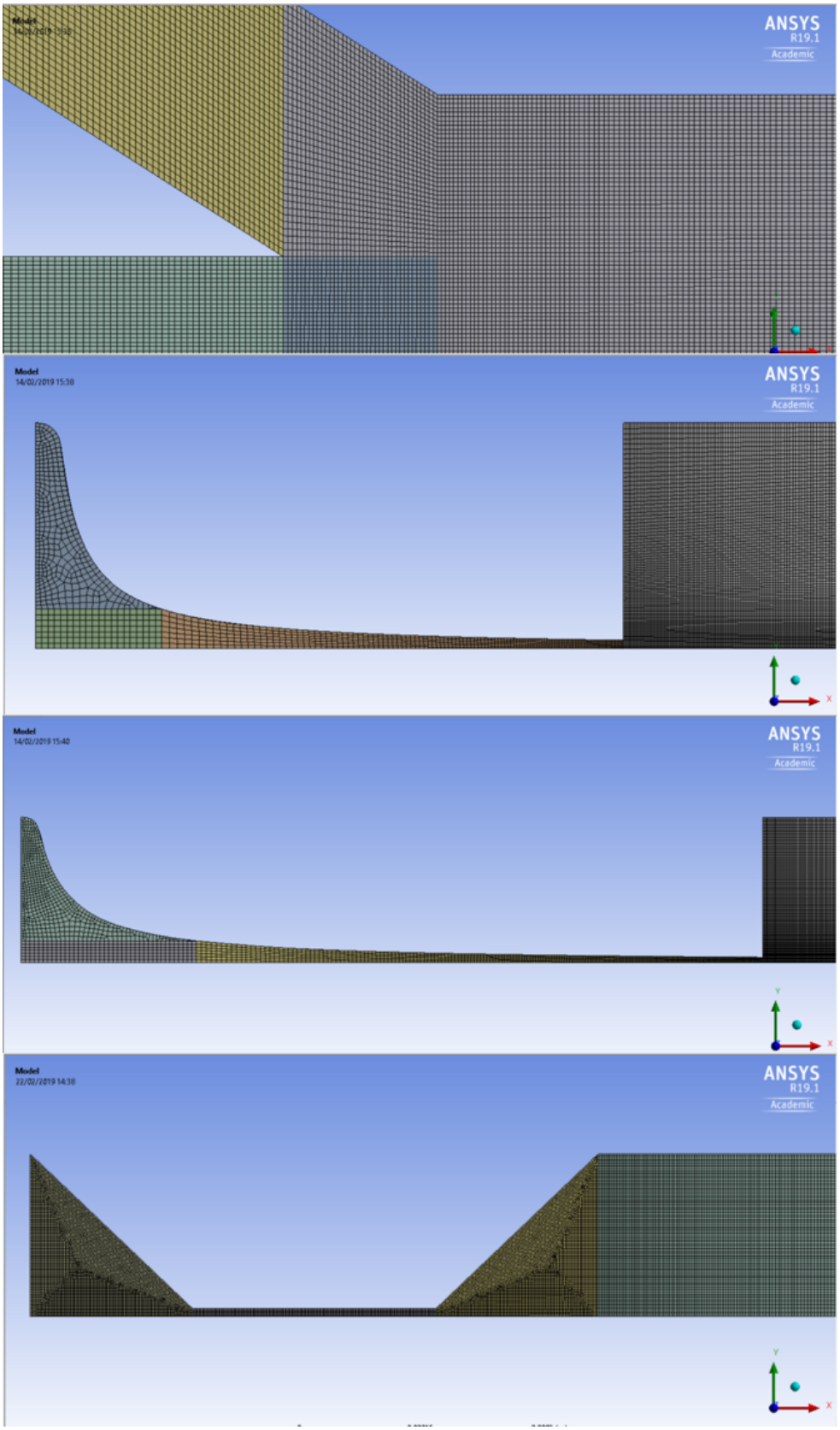

Figure 3.16: Overview of the four meshes (from top to bottom): upstream (detail at junction), hyperbolic with $L_c = 500\mu m$, hyperbolic with $L_C = 1000\mu m$, straight channel.

The key regions where a fine and high quality mesh is needed are the junction for the upstream sheath flow module, the whole channel for the straight geometry and the contraction (point of minimum width, $y = \frac{w_c}{2}$) for the hyperbolic channels. For the hyperbolic channels the smallest elements were cubical elements with $2\mu m$ edges, whereas for the straight channel a size of $4\mu m$ was fine enough, given the fact that the ri-expansion was gradual with respect to he abrupt ri-expansion of the hyperbolic geometries.

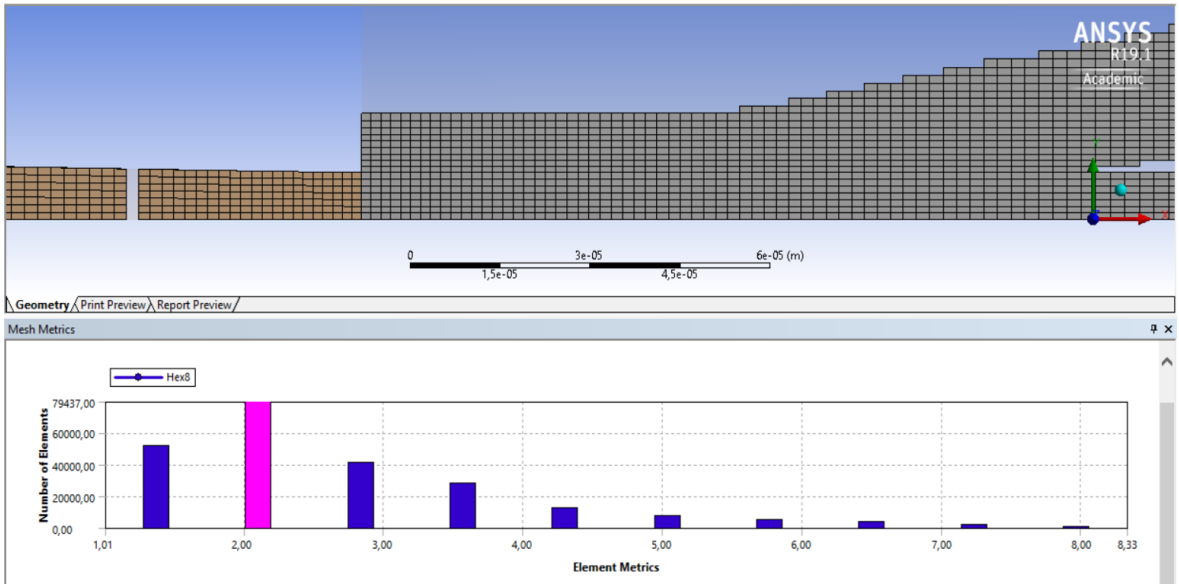

Figure 3.17: Visualization of the aspect ratio as a quality parameter of the mesh: elements corresponding to the selected value (AR=2) are highlighted.

3.3.3 Simulations

The boundary conditions for the simulations were defined as in Figure 3.18 and analogously for the other channels. This is easily done by creating "named selections" in ANSYS Mesh named respectively "Inlet", "Outlet", etc ato be automatically recognized by ANSYS Fluent as the corresponding boundary conditions:

- velocity inlet: either a specified velocity in $\left[\frac{m}{s}\right]$ or a profile;
- pressure outlet: zero gauge pressure, basically meaning atmospheric pressure;

- symmetry: zero normal velocity and zero normal gradients of all variables at a symmetry plane;
- walls: the velocity is null at walls since these are stationary and no-slip is assumed.

Inlet velocities of the upstream part were set as mean velocities

$$v_{mean} = \frac{Q}{A} \quad \left[\frac{m}{s}\right] \tag{3.3}$$

with Q the flow rate and A the cross section for each condition (see Appendix A for complete report of all values). For each channel (hyperbolic channels and straight channel) the inlet velocity profile corresponded to the outlet velocity profile of the upstream sheath flow system at each flow rate.

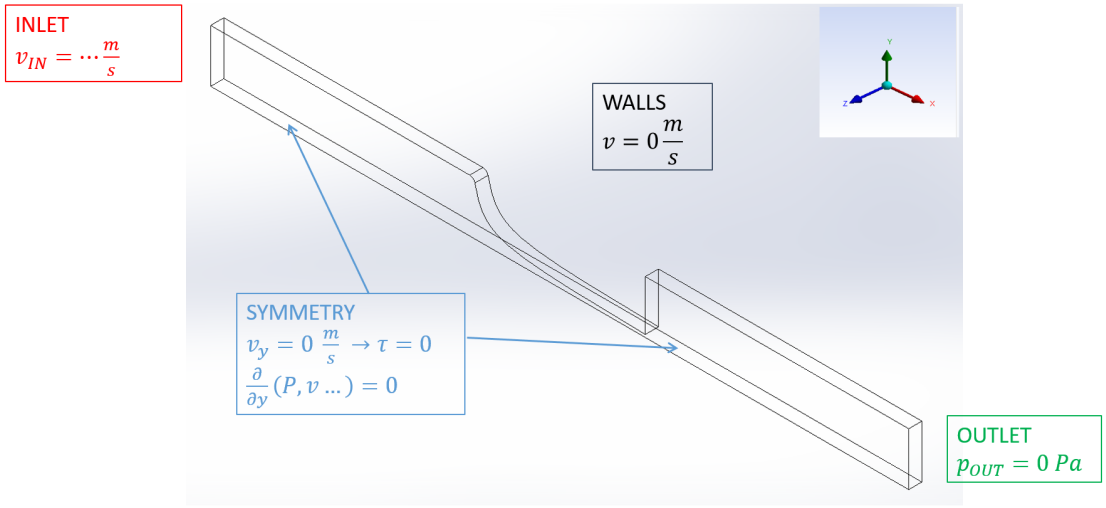

Figure 3.18: Boundary conditions for the channel simulations.

Steady state simulations with pressure based solver and laminar flow regime were set. Default solving methods were suited since the simulations were relatively simple in terms of model (no turbulent or vorticity phenomena, low Reynolds number and no complex geometrical features): SIMPLE scheme for pressure and velocity coupling and second order methods for both pressure and momentum as spatial discretization.
As in the experiments mainly Buffer 0.25 and Buffer 0.50 were used, simulations were

performed with both fluids at the corresponding flow rates (see Table 3.4 on page 46). Both of them had a shear thinning behaviour, which could be modelled in ANSYS Fluent simply by fitting the power law model with appropriate indices:

$$\tau = K \cdot \dot{\gamma}^{n-1} \tag{3.4}$$

where $\tau\,[Pa]$ is the shear stress, $\gamma\,[s^{-1}]$ the shear rate, $K\,[\frac{kg}{m \cdot s^{n-2}}]$ the consistency index and $n\,[-]$ the power index. The software also requires upper and lower bounds of the viscosity values: for Buffer 0.50 these were found in literature (Herbig et al., 2018) whereas for Buffer 0.25 they were taken from the rheological characterization with the Couette device (Figure 3.6 on page 47). The respective values for the two buffers used in the simulations are reported in Table 3.5.

	Buffer 0.25	**Buffer 0.50**
$K[\frac{kg}{m \cdot s^{n-2}}]$	0.066	0.178
$n[-]$	0.222	0.677
$\eta_{min}[Pas]$	0.0025	0.004
$\eta_{max}[Pas]$	0.0684	0.015

Table 3.5: Indexes for the power law fitting of the the shear thinning buffers.

3.3.4 Parametrization

A convenient way of performing simulations for the hyperbolic channels of different dimensions was the use of parametrization of the width w_c to span the three desired values $(15, 20, 25\mu m)$, with ANSYS Direct Optimization. By setting the element size in the mesh instead of the number of divisions for the edges defining w_c, the software automatically rebuilt a mesh retaining element size: in this way, any influence on the results given by a change in the element size right where accuracy was most important could be avoided. With this tool, quantities of interest were chosen as output parameters whose value was updated and available for post processing to show their

dependence on the variation of inputs (Figure 3.19).

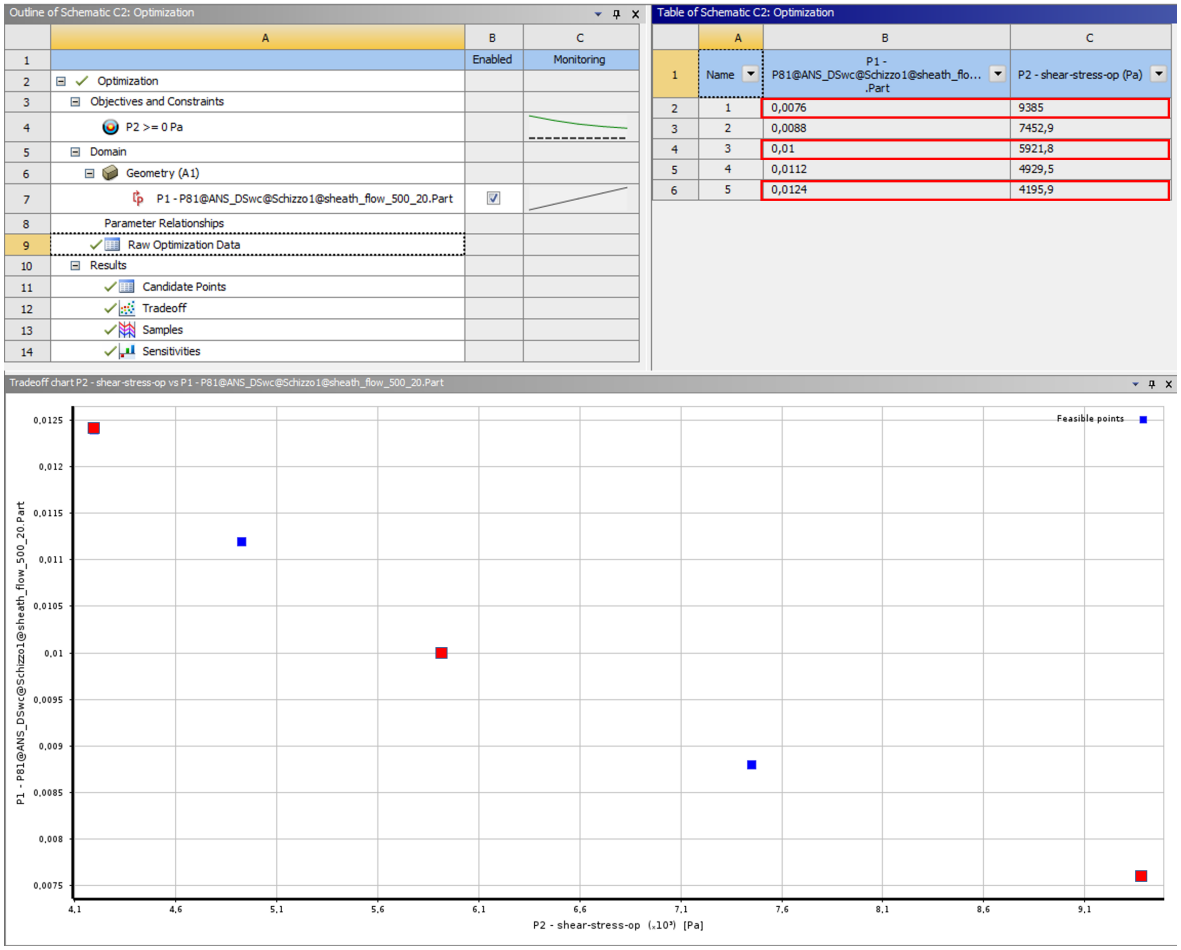

Figure 3.19: Screenshot of the Direct Optimization tool: by varying the parameter w_c the output parameter τ_{max} (maximum wall shear stress) was updated. Since the simulations were performed on half geometry, the input parameter was half the width at the contraction w_c, varying from $7.5\mu m$ to $12.5\mu m$. The obtained values are shown in the Table (top right) and plotted in the graph (bottom) showing that a decrease in the width at the contraction (y-axis) was followed by an increase in shear stress (x-axis).

3.3.5 Grid independence test

It is good practice in any numerical simulation to test the robustness of results with respect to the mesh, meaning the results should be independent of the mesh size. Commonly, few parameters are identified as "monitors" and simulations are performed with progressively finer meshes. The coarsest mesh which yields monitor values within

5% variation with respect to the finer mesh is selected. There is no precise protocol for mesh refining but normally an increase of 50 to 100% in the number of elements is suggested.

A grid independence test was performed for both the upstream sheath system and the two channels ($L_c = 500\mu m$, $L_c = 1000\mu m$): this evaluation was based on the calculation of the maximum velocity on a plane positioned at half of the device height, $z = \frac{h}{2}$, the maximum shear stress at the walls and the average pressure at surfaces where the geometry changes (Figure 3.20).

The grid independence test showed negligible differences between three progressively finer meshes for the upstream sheath flow system (Table 3.6) hence the coarsest mesh was chosen (230'700 elements); for the channel, there was a $\sim 6\%$ variation in mean pressure between the coarsest and the finest mesh (Table 3.7) thus the intermediate mesh was selected (338'080 elements).

number of elements	$v_{max}[\frac{m}{s}]$	$P_{mean}[Pa]$	$\tau_{wall}[Pa]$
230'700	1.0407e+01	1.0194e+04	9.2436e+03
338'050	1.0694e+01	1.0223+04	9.4100e+03
	(+2.75%)	(0.28%)	(+1.8%)
461'720	1.0591e+01	1.0083e+04	9.2984e+03
	(+1.76%)	(-1.08%)	(+0.59%)

Table 3.6: Grid independence test for the upstream sheath flow system. Percentage variations with respect to te coarsest mesh are reported. Values refer to the simulation with Buffer 0.25 at the maximum flow rate $Q_{tot} = 100\frac{\mu l}{min}$.

number of elements	$v_{max}[\frac{m}{s}]$	$P_{mean}[Pa]$	$\tau_{wall}[Pa]$
161'432	3.8515e-01	2.7032e+04	2.8535e+02
338'050	3.9391e-01	2.6021e+04	2.8051e+02
	(+2.27%)	(-3.74%)	(-1.62%)
440'260	3.9471e-01	2.8630e+04	2.8572e+02
	(+2.48%)	(+5.91%)	(+0.12%)

Table 3.7: Grid independence test for the hyperbolic channel: percentage variations with respect to te coarsest mesh are reported. Values refer to the simulation with Buffer 0.25 at the maximum flow rate $Q_{tot} = 100\frac{\mu l}{min}$.

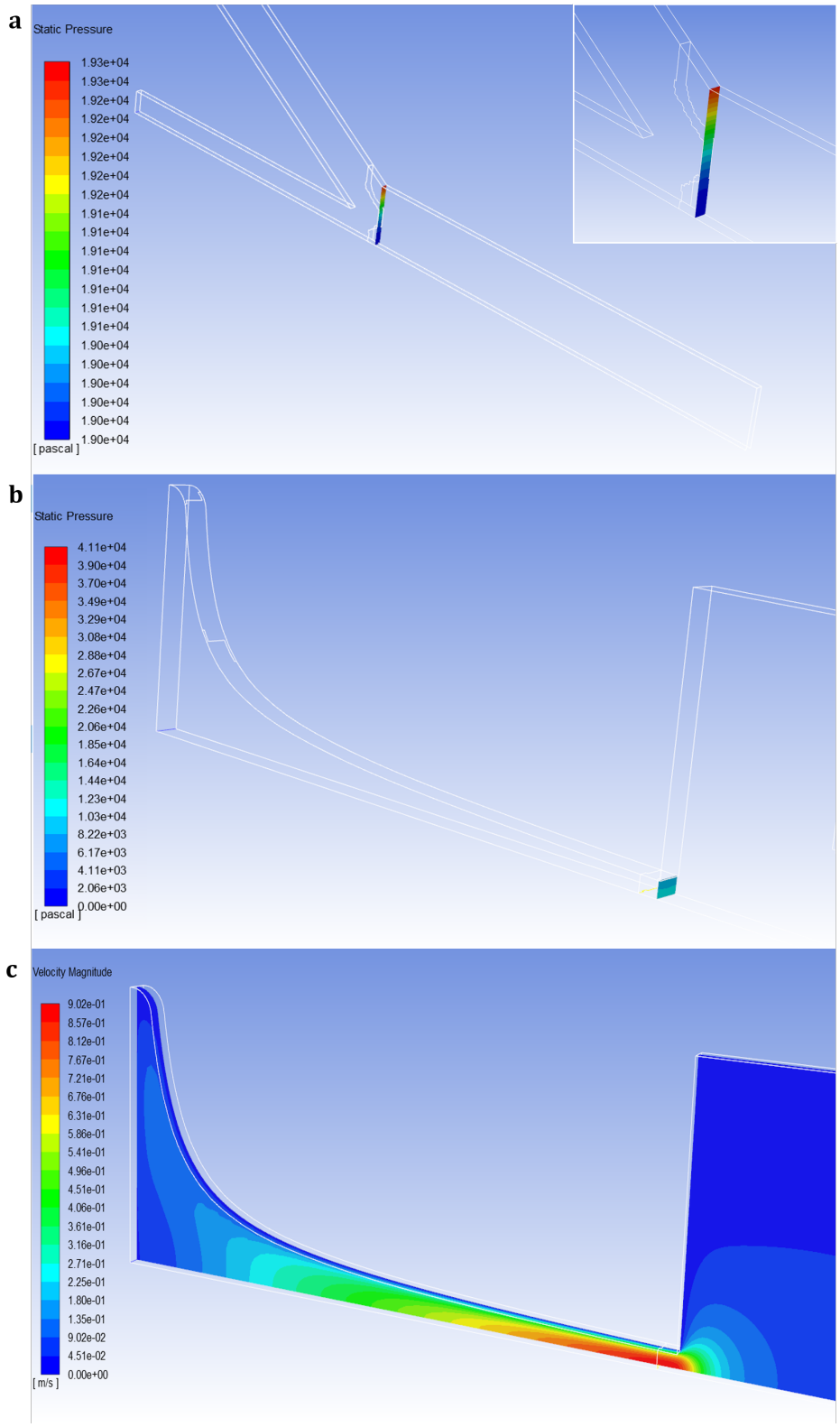

Figure 3.20: Planes to track pressure in the upstream sheath flow part (a) and in the channel (b) and velocity in a monitor plane situated at mid height (c).

3.3.6 Definition of shear and extensional rates

Shear and extensional stress are of primary importance in the evaluation of deformation, being the two main forces playing a role. These derive directly from the respective velocity derivatives

- shear rate:

$$\dot{\gamma} = \frac{dv_x}{dy} \tag{3.5}$$

- extensional rate

$$\dot{\varepsilon} = \frac{dv_x}{dx} \tag{3.6}$$

scaled by viscosity:

- shear stress

$$\tau = \eta\dot{\gamma} \tag{3.7}$$

- extensional stress

$$\tau_{ext} = \eta\dot{\varepsilon} \tag{3.8}$$

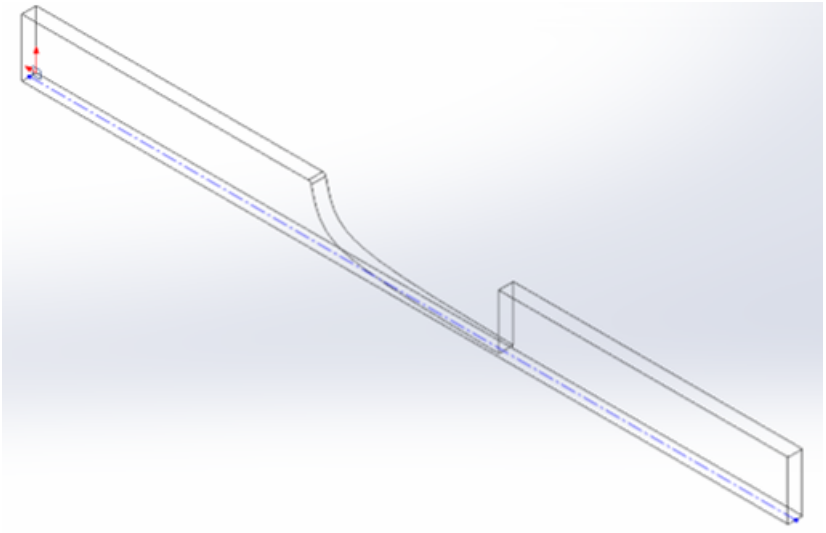

Figure 3.21: Representation of the centreline for the hyperbolic channel. The same applies to the straight channel (not shown).

The maximum velocity along the monitor plane and the velocity trend along the centreline ($z = \frac{h}{2}$, blue dotted line in Figure 3.21) were evaluated, since ideally cells were supposed to position along this line during experiments thanks to the confinement of the sheath flow and the physical constraint of a the low height of devices ($h = 20\mu m$). Wall shear stress was also evaluated and compared among different channels.

Results and Discussion

4.1 Computational results

The main objective of the computational analysis was to gain insight into the fluid dynamic quantities of interest and into their dependence on geometrical and rheological parameters. The following were analysed:

- velocity field (v_{mean}, v_{max} $[\frac{m}{s}]$);
- extensional rate

$$\dot{\varepsilon} = \frac{dv_x}{dx} \quad [s^{-1}] \tag{4.1}$$

- shear rate

$$\dot{\gamma} = \frac{dv_x}{dy} \quad [s^{-1}] \tag{4.2}$$

- shear stress

$$\tau = \eta \frac{dv_x}{dy} = \eta\dot{\gamma} \quad [Pa] \tag{4.3}$$

with x being the flow direction and y the transverse direction (see following figures).

4.1.1 Velocity and shear stress

Regardless of the punctual values that varied with flow rates, repeating trends of velocity and shear stress were observed in defined planes (a monitor plane at $z = \frac{h}{2}$ and channel walls respectively).

For the upstream part, the flow was already fully developed less than 1 mm downstream the junction (Figure 4.1, in orange) and the maximum shear stress at the walls was detected in correspondence with the junction (Figure 4.2, in red); unlike the well known case of an axisymmetric cylindrical channel where the shear stress is uniform (and has its maximum) on the walls, in a channel with rectangular cross section it dropped significantly at the corners (Figure 4.2, in light blue).

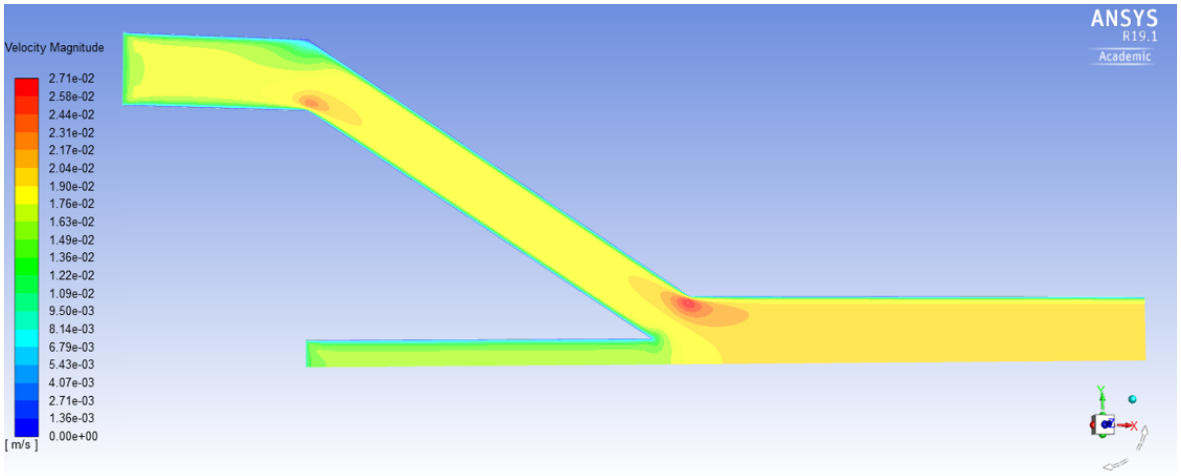

Figure 4.1: Contours of velocity magnitude on the monitor plane for the upstream sheath flow system (simulation with Buffer 0.5 and $Q_{sample} = 1.8\frac{\mu l}{min}, Q_{sheath} = 5.4\frac{\mu l}{min}$).

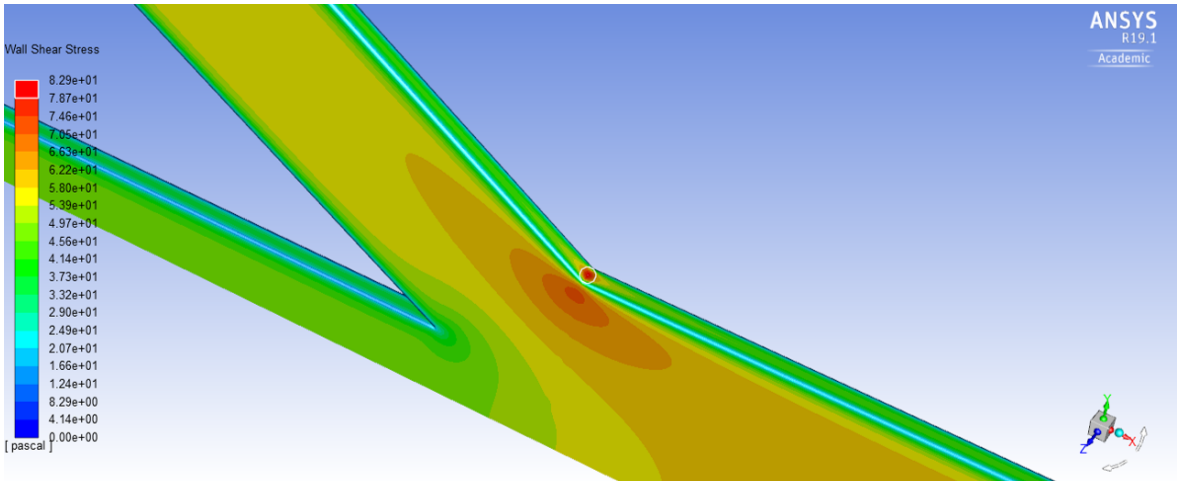

Figure 4.2: Contours of wall shear stress on the walls for the upstream sheath flow system. (simulation with Buffer 0.5 and $Q_{sample} = 1.8\frac{\mu l}{min}, Q_{sheath} = 5.4\frac{\mu l}{min}$)

As for the hyperbolic channels, velocity was higher along the centreline (the furthest from walls) and expectedly reached the peak at the contraction; after the ri-expansion the velocity dropped of one order of magnitude (10^0 to 10^{-1} and to zero, red and blue respectively) and the length up to which a higher speed was still retained was dependent on the flow rate (Figure 4.3). This was not evident in the case of Buffer 0.50 even comparing the minimum and maximum flow rates ($Q_{tot} = 2.4\frac{\mu l}{min}, Q_{tot} = 14.4\frac{\mu l}{min}$) but was instead observed for the case of Buffer 0.25 and the flow rates $Q_{tot} = 40\frac{\mu l}{min}, Q_{tot} = 100\frac{\mu l}{min}$, as visible both in the contours (Figure 4.3) and from the profiles (Figure 4.4).

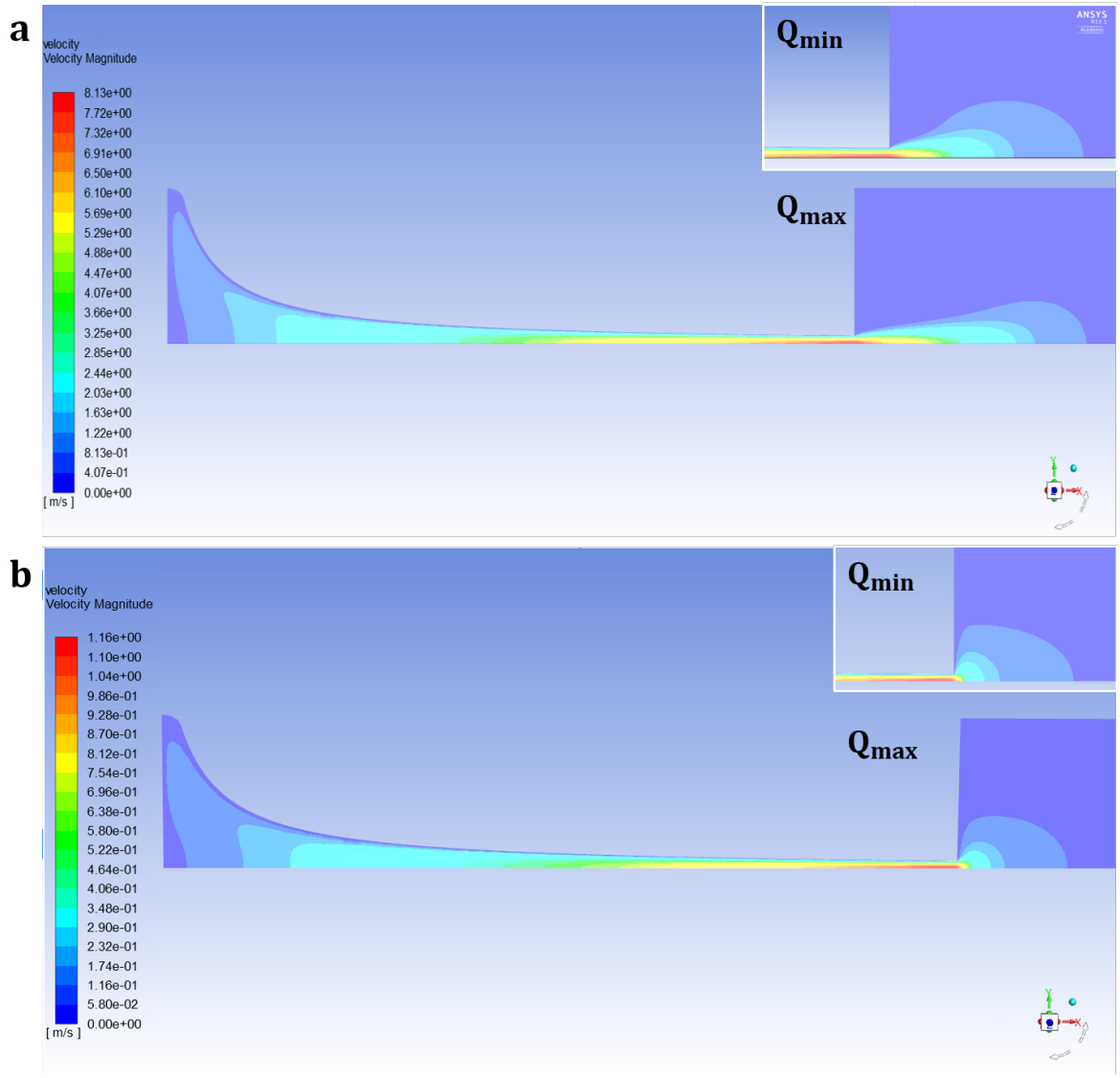

Figure 4.3: Contours of velocity magnitude on the monitor plane for the long hyperbolic channel: simulations with Buffer 0.25 (a) and Buffer 0.50 (b) at the highest and lowest respective flow rates to show the difference in the profile at the ri-expansion. Values refer to the simulation with the channel of length $L_c = 1000\mu m$ and width at the contraction $w_c = 20\mu m$.

The same patterns were found for the short channels with slight differences (basically just in the magnitude): for this reason, figures are represented for just one case.

The wall shear stress presented a maximum located at the contraction (on the top wall) and decreased at the corners of the channel (inset to Figure 4.5, in light blue). A very rapid undershoot was visible from the decrease of more than one order of magnitude in correspondence with the riexpansion.

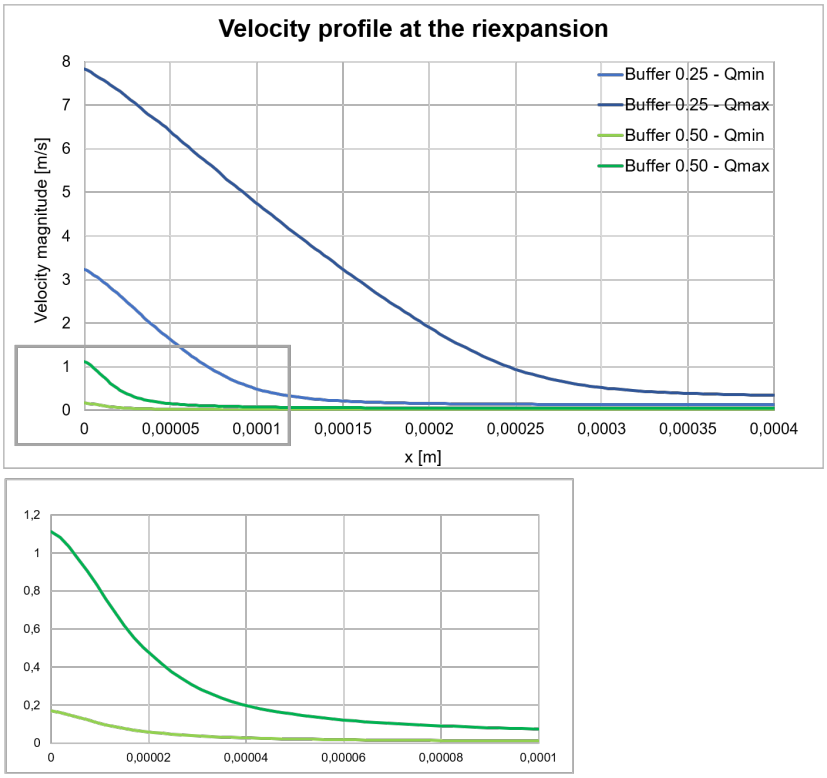

Figure 4.4: Velocity profiles at the ri-expansion for the long hyperbolic channel with intermediate width ($L_c = 1000\mu m, w_c = 15\mu m$) and both buffers at the minimum and maximum respective flow rates. The x coordinate in the abscissa indicates the position along the centreline after the ri-expansion, that is, starting from the origin of the coordinate system situated in correspondence with the ri-expansion.

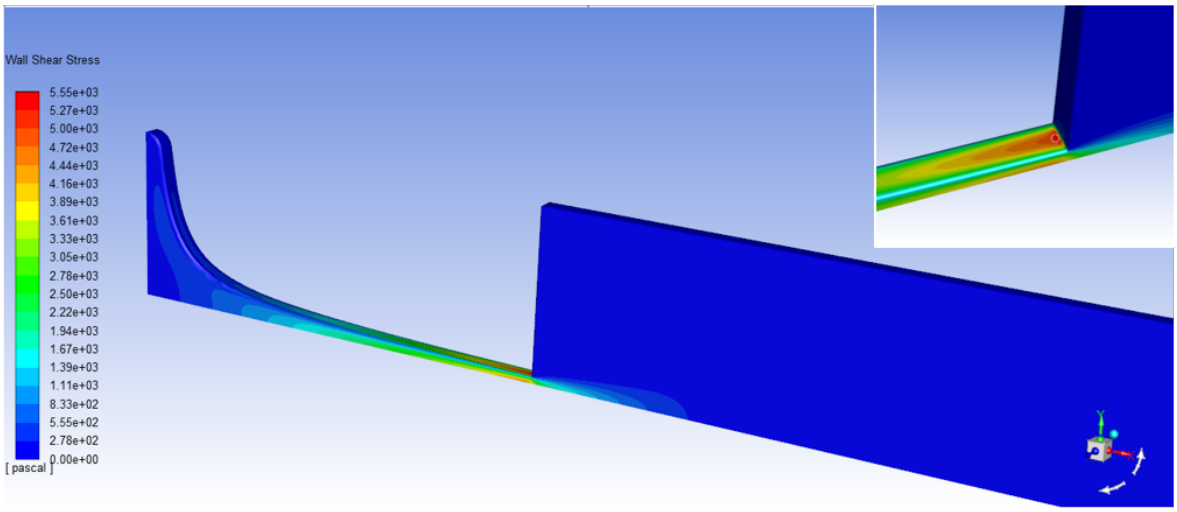

Figure 4.5: Contours of wall shear stress on the walls for the short hyperbolic channel (simulation with Buffer 0.25 and $Q_{tot} = 60\frac{\mu l}{min}$.)

The straight channel ($L_c = 300\mu m$) presented slightly different patterns: since the cross section did not shrink as in the hyperbolic cases, the velocity profile was constant along the channel (Figure 4.6) whereas the maximum shear stress on the wall was found in correspondence with the beginning of the straight channel (Figure 4.7, highlighted red spot) and with the same distribution for the four faces of the channel (given the full symmetry of the $20\mu m$ x $20\mu m$ square cross section).

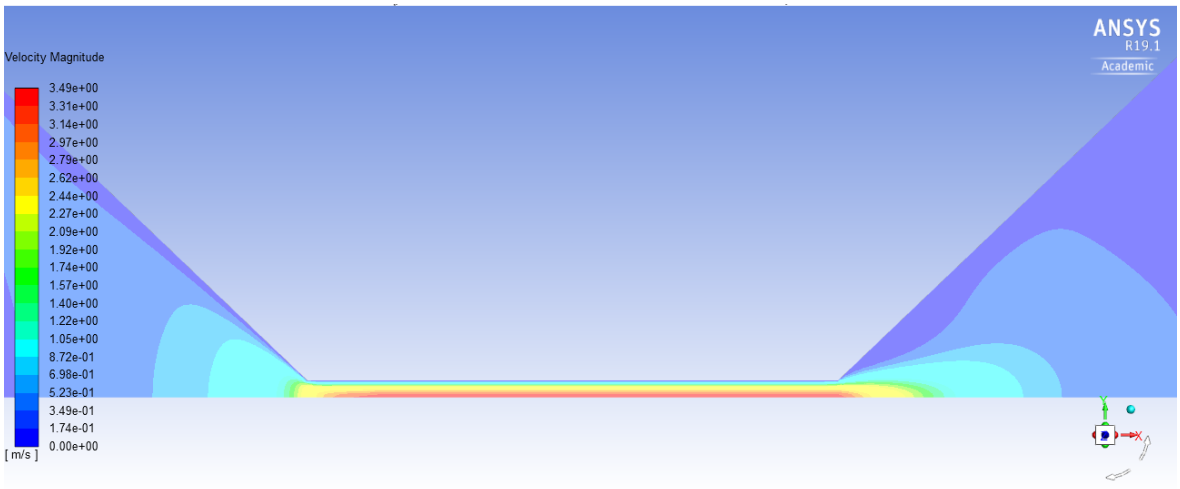

Figure 4.6: Contours of velocity magnitude on the monitor plane for the straight channel (simulation with buffer 1 and $Q_{tot} = 40\frac{\mu l}{min}$.)

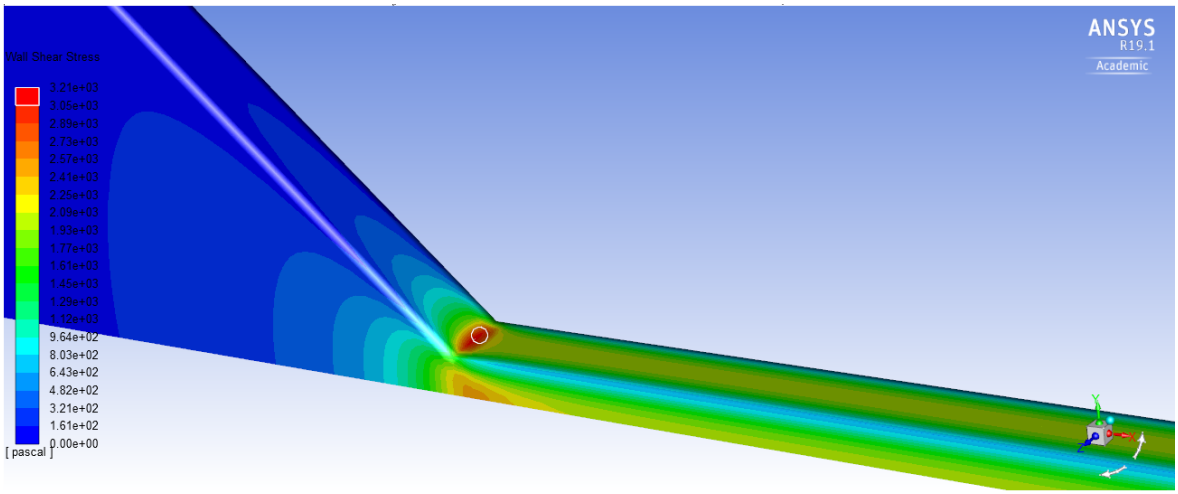

Figure 4.7: Contours of wall shear stress on the walls for the straight channel (simulation with buffer 1 and $Q_{tot} = 10\frac{\mu l}{min}$.)

To establish a comparison between all channels of the same width ($w_c = 20\mu m$) an overview of the velocity and shear stress values obtained for each case for Buffer 0.25 and Buffer 0.50 is given in Table 4.1 respectively. For both cases, the maximum total flow rate was considered (buffer 1: $Q_{max} = 100\frac{mul}{min}$; buffer 2: $Q_{max} = 14.4\frac{mul}{min}$). Comparing the channels with the same width ($w_c = 20\mu m$) it could be observed that the maximum velocity was higher for the straight channel with respect to both hyperbolic channels. In all cases, the velocity in the long hyperbolic channels was slightly higher than in the short ones.

Channel	**Size**	$\boldsymbol{\tau_{max}[Pa]}$	$\boldsymbol{v_{max}[\frac{m}{s}]}$
Straight	$L_c = 300\mu m, w_c = 20\mu m$	9.78e+03	8.72e+00
Hyperbolic	$L_c = 500\mu m, w_c = 15\mu m$	9.41e+03	1.04e+01
Hyperbolic	$L_c = 1000\mu m, w_c = 15\mu m$	9.27e+03	1.12e+01
Hyperbolic	$L_c = 500\mu m, w_c = 20\mu m$	5.83e+03	7.84e+00
Hyperbolic	$L_c = 1000\mu m, w_c = 20\mu m$	5.59e+03	8.13e+00

Table 4.1: Maximum velocity and shear stress in the different geometries (Buffer 0.25).

Channel	**Size**	$\boldsymbol{\tau_{max}[Pa]}$	$\boldsymbol{v_{max}[\frac{m}{s}]}$
Straight	$L_c = 300\mu m, w_c = 20\mu m$	1.52e+03	1.19e+00
Hyperbolic	$L_c = 500\mu m, w_c = 15\mu m$	2.24e+03	1.53e+01
Hyperbolic	$L_c = 1000\mu m, w_c = 15\mu m$	2.23e+03	1.61e+00
Hyperbolic	$L_c = 500\mu m, w_c = 20\mu m$	1.43e+03	1.12e+00
Hyperbolic	$L_c = 1000\mu m, w_c = 20\mu m$	1.39e+03	1.13e+00

Table 4.2: Maximum velocity and shear stress in the different geometries (Buffer 0.50).

As for shear stress, at low viscosity and high flow rates (Buffer 0.25) the straight channel expectedly produced a much larger shear stress with respect to the hyperbolic channels with the same cross section ($20\mu m$ x $20\mu m$) - 68% and 75% higher than the one in the short and long hyperbolic channels respectively - but rather closer to the case of $w_c = 15\mu m$ (Table 4.1). This was likely due to the fact that the hyperbolic channels had a larger cross section with respect to the straight one except for the very last segment before the ri-expansion, where the width actually reached $20\mu m$.

At high viscosity and low flow rates (Buffer 0.50), τ_{wall} in the straight channel was comparable to the hyperbolic channels with the same width (Table 4.2), whereas a smaller width ($w_c = 15\mu m$) produced 28% and 35% higher stresses compared to the straight channel (short and long hyperbolic channels respectively).

The complete report of velocity and shear stress in all conditions (all flow rates and all dimensions) is given in Appendix A.

The evaluation of shear stress established above is to be taken as a means of comparison between the different cases to understand the influence of shape, but the definition of shear stress at the walls was not suited to evaluate the effective stress imposed on the cells, as they preferentially positioned along the centre of the channel in all directions: in the XY plane - thanks to the focusing of the sheath flow - and in the z direction - thanks to the confinement of a low height channel ($h = 20\mu m$) and to the use of a viscous buffer. Even if this could not be assessed quantitatively from the images, as the microscope could only provide a 2D information, cells were observed to have very similar focal planes during experiments, meaning the were all roughly at the same position in the z direction.

Hence, it was convenient to evaluate the shear rate instead as an indicator of stress and related to extensional rate.

4.1.2 Shear and extensional rates

To understand the trend of shear and extensional rates, velocity profiles in the straight and hyperbolic channels were observed (Figure 4.8 and 4.9 respectively). The velocity magnitude corresponded in practice to the sole x component v_x, due to the shape of the channels with the x dimension (along the flow of direction) predominant over the width (y direction) and height (z direction).

Both quantities were evaluated for all geometries and conditions (flow rates, viscosities): examples of the shear rate and extensional rate along the centreline are reported

and the regions where they were evaluated (delimited by black dotted lines) corresponded to where deformation was calculated in the post processing of experimental data ($-80\mu m < x < 0$). The origin of the coordinate system was placed at the contraction for the hyperbolic channels (Figure 4.9, top - and analogously for the case $L_c = 1000\mu m$) and $200\mu m$ downstream the end of the straight channel (Figure 4.8, top). The extensional rate plots for each type of channel and for the two buffers

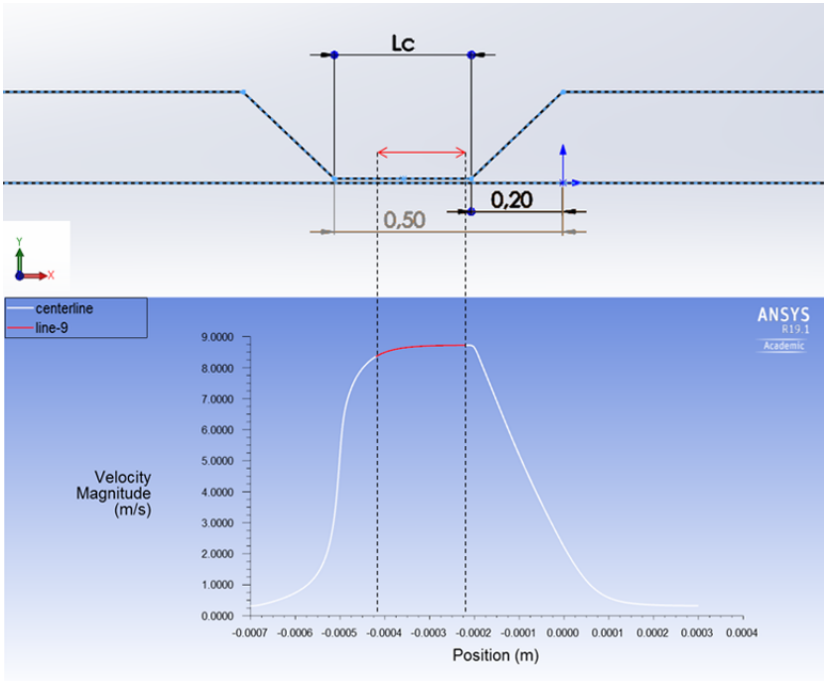

Figure 4.8: Velocity profile along the centreline in the straight channel: the red part identifies the region where shear and extensional rates were evaluated.

studied are reported in Figure 4.10. As expected the constant velocity yielded a zero extensional rate in the straight channel, whereas the hyperbolic geometry produced a linear increase in velocity along the progressively shrinking cross section, resulting in a constant (non zero) extensional rate for most part of the channel, except for the initial part when $\dot{\varepsilon}$ was still increasing. The mean values in the section considered for later evaluation of the experimental data were taken as representative (red dots in Figure 4.10).

About 20 μm to 40 μm prior to the ri-expansion, a large undershoot in the extensional

rate was observed due to the quasi instantaneous drop of the velocity: for the lower flow rates (Buffer 0.50) a sharp negative peak followed by a very rapid increase was reported, whereas in the case of higher velocities (Buffer 0.25) it started to increase more smoothly after the drop in correspondence with the ri-expansion.

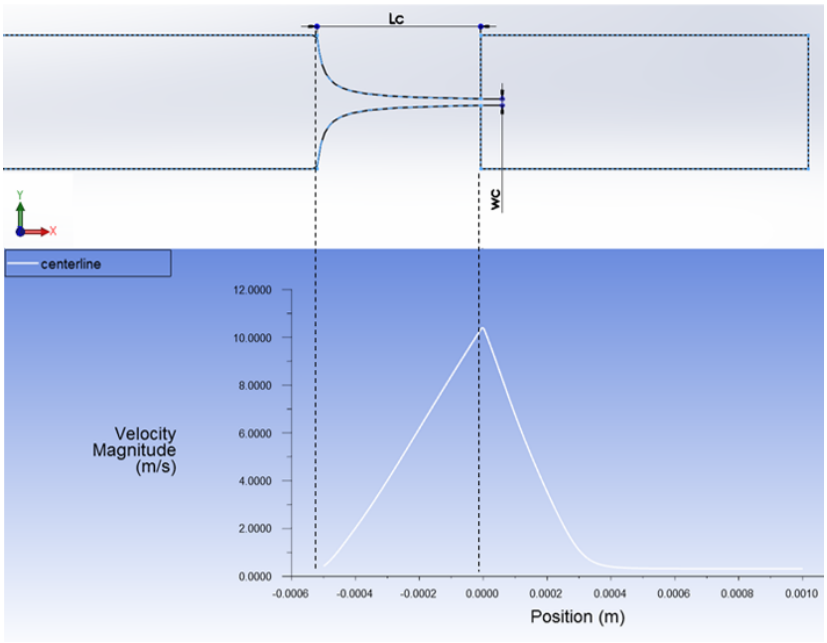

Figure 4.9: Velocity profile along the centreline in the short hyperbolic channel.

The shear rate plots for each type of channel and for the two buffers are reported in Figure 4.11. This quantity was nearly constant in the case of the straight channel, as expected in a developed flow through a rectangular cross section, whereas it steeply increased along the hyperbolic channels up to a local maximum just before the ri-expansion, then dropped and reached a new higher peak in correspondence with the ri-expansion. This was due to the rapid change in direction of the velocity streamlines that spread all over the expanded section, going upwards (positive y direction). In particular, for lower flow rates (Buffer 0.50) the streamlines instantaneously rearranged along the whole ri-expansion, whereas at higher velocity (Buffer 0.25) a vortex arose at the ri-expansion (Figure 4.12).

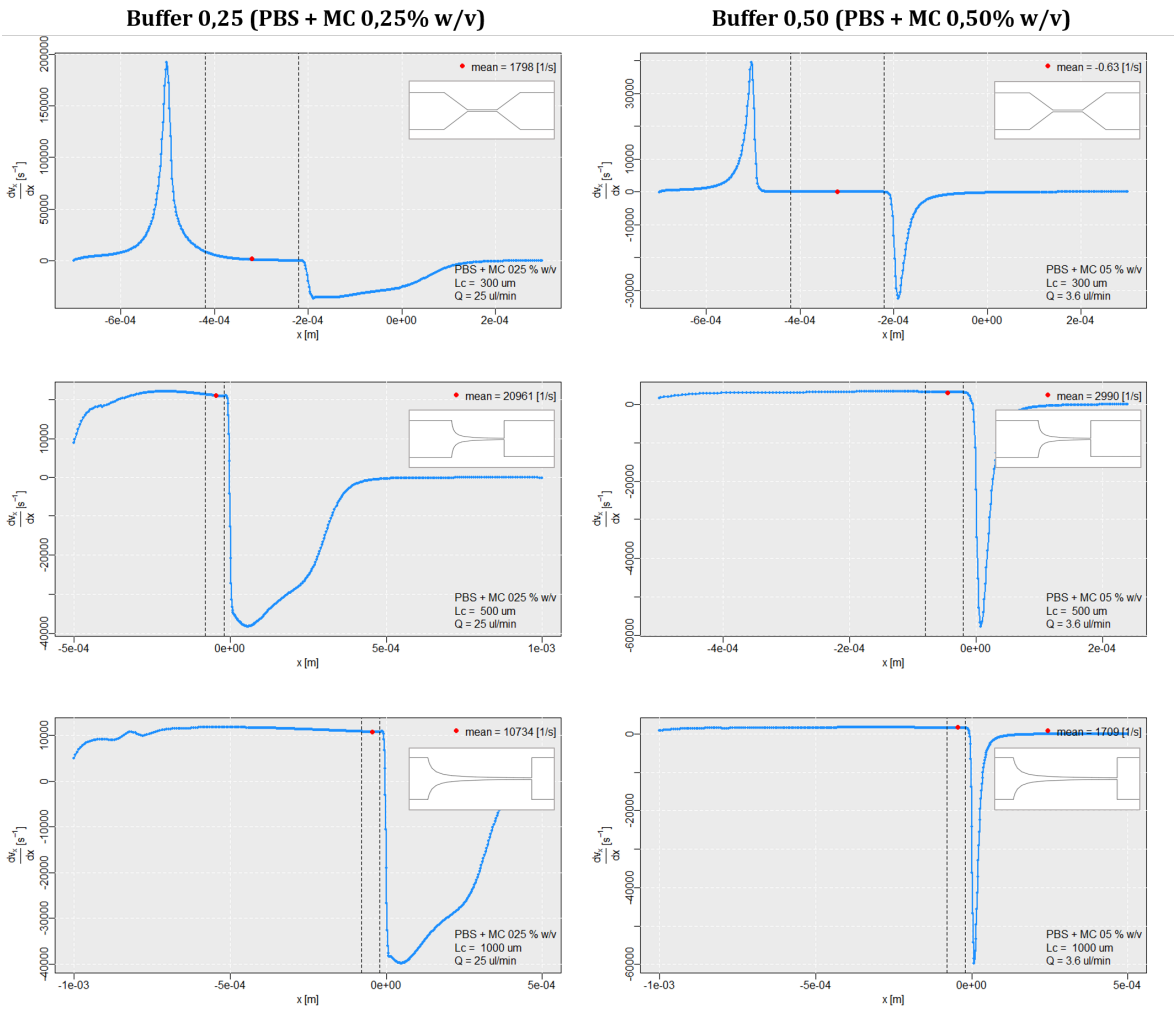

Figure 4.10: Extensional rate along the centreline in the three types of channels, as shown in the insets. The plots on the left refer to Buffer 0.25, the ones on the right refer to Buffer 0.50; all the plots refer to the maximum flow rate cases ($Q_{tot} = 100\frac{\mu l}{min}$ and $Q_{tot} = 14.4\frac{\mu l}{min}$ respectively).
The red dots identify the mean values in the region of the channel of interest that were taken as representative for that specific condition.

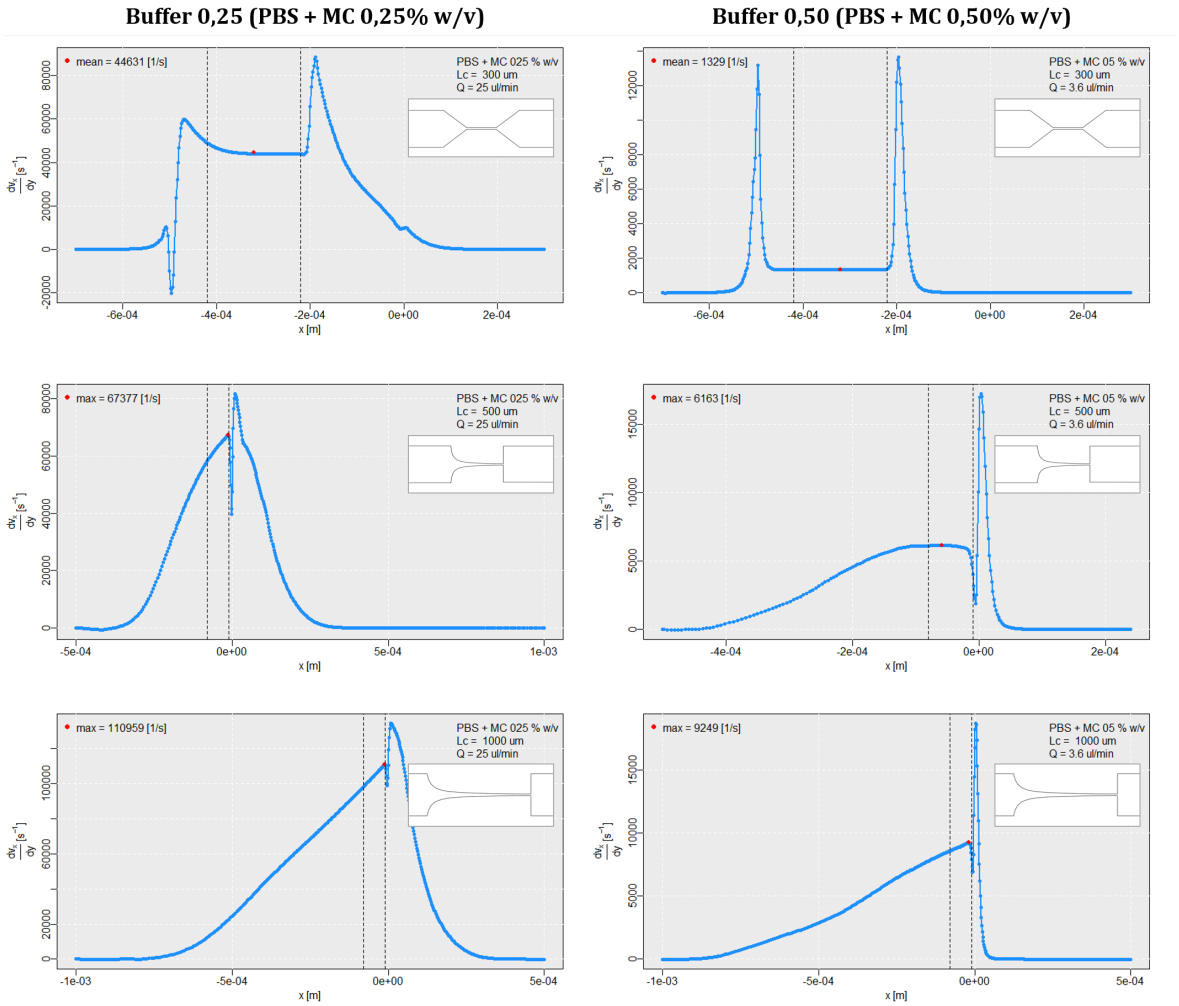

Figure 4.11: Shear rate along the centreline in the three types of channels, as shown in the insets The plots on the left refer to Buffer 0.25, the ones on the right refer to Buffer 0.50; all the plots refer to the maximum flow rate cases ($Q_{tot} = 100\frac{\mu l}{min}$ and $Q_{tot} = 14.4\frac{\mu l}{min}$ respectively).
The red dots identify the values of interest in the selected region of the channel that were taken as representative for that specific condition: for the straight channel the constant value and for the hyperbolic channels the maximum before the ri-expansion.

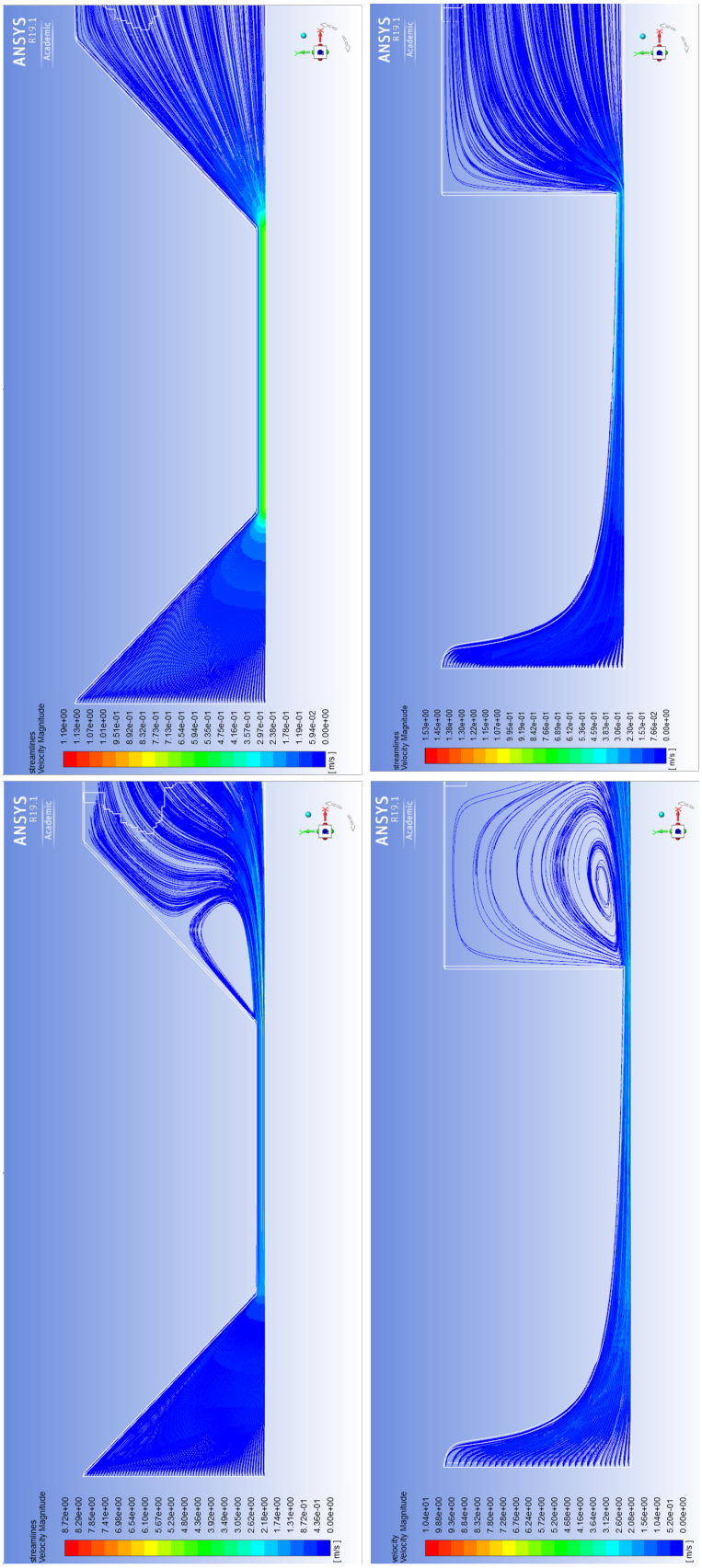

Figure 4.12: Streamlines of the velocity magnitude in the two geometries (the long hyperbolic channel behaves analogously to the short one, not shown) for Buffer 0.25 (left) and Buffer 0.50 (right) at the maximum corresponding flow rates ($Q_{tot} = 100\frac{\mu l}{min}$, $Q_{tot} = 14.4\frac{\mu l}{min}$).

With the criteria discussed above, punctual values of shear and extensional rates as a function of flow rate were compared (Figure 4.13).

As expected, the extensional rate in the straight channel was close to zero for the low flow rates, Buffer 0.50) and much lower in the case of higher flow rates (Buffer 0.25). For all hyperbolic channels, the extensional rate increases linearly with the flow rate and is higher in the shorter channels ($L_c = 500\mu m$) with respect to their longer counterpart (Figure 4.13, top).

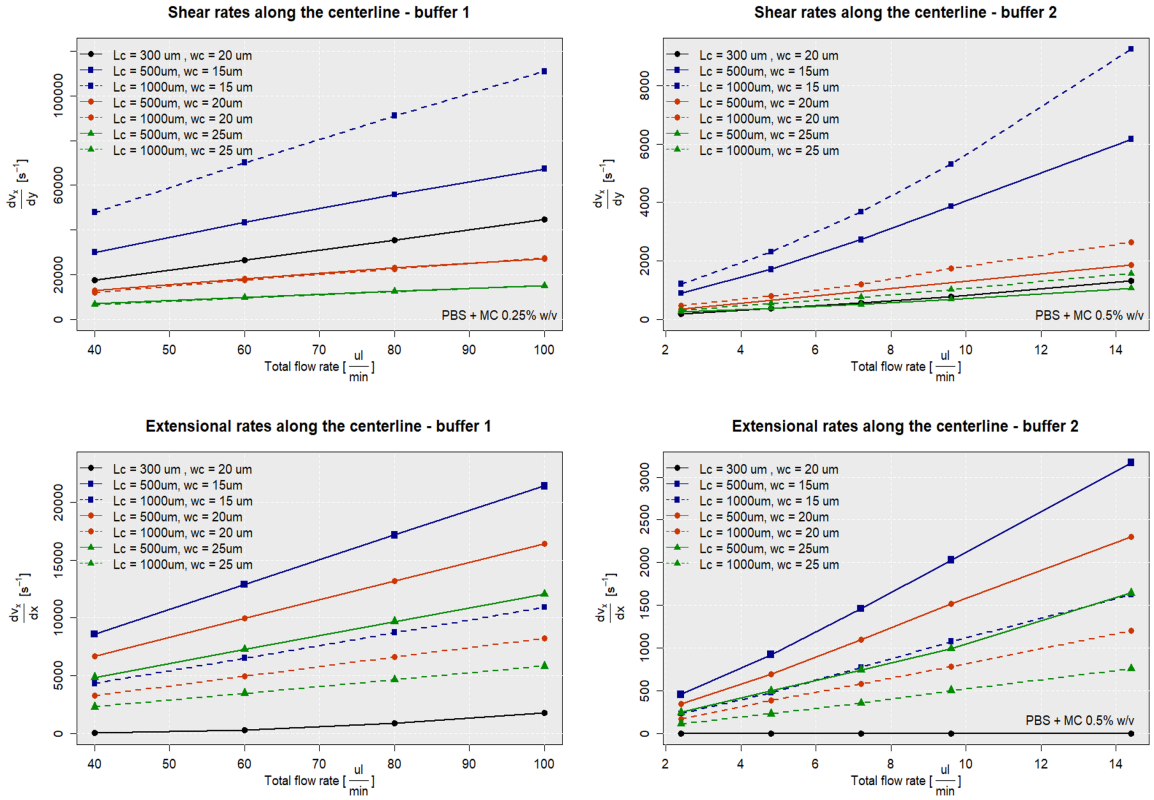

Figure 4.13: Extensional and shear rates as function of the flow rate Q for all the hyperbolic channels and the straight channel (left panel: Buffer 0.25, right panel: Buffer 0.50).

As regards the shear rate, a different behaviour was observed for the narrowest width $w_c = 15\mu m$ as compared to higher w_c: for the former, shear rate showed to be higher in the longer channel, while the opposite was reported for $w_c = 20\mu m$ and $w_c = 25\mu m$. At higher flow rates (Buffer 0.25), $\dot{\gamma}$ are almost overlapping (Figure 4.13,

bottom left). In this condition the shear increases linearly with the flow rate, unlike what happens for the lower flow rates where a pronounced non linearity is visible for the case $w_c = 15\mu m$ (Figure 4.13, bottom right).

The complete report of $\dot{\gamma}$ and $\dot{\varepsilon}$ for all flow rates is given in Appendix A, but the difference in magnitude between the two cases (low and high viscosity) can be already appreciated from the different scales of the y-axes.

4.2 Experimental results

All data come from videos recorded with the high speed camera in bright field microscopy: they were converted to image stacks with the software ImageJ and processed as explained previously (see Materials and Methods). The extrapolated geometrical parameters were used to calculate two quantities of interest for the description of cell deformation:

- Deformation, a non dimensional parameter defining how far is the cell from its rest circular shape:

$$Deformation = 1 - Circularity = 1 - \frac{2\sqrt{\pi A}}{P} \tag{4.4}$$

  where A [μm^2] is the area and P [μm] the perimeter of the cell contour;

- Ratio, a non dimensional parameter defining the stretching in the horizontal direction assuming that the cell acquires a nearly elliptical shape with the long axis aligned to the flow direction (Figure 4.14):

$$Ratio = \frac{\text{Long Axis}}{\text{Short Axis}} \tag{4.5}$$

To rule out any ambiguity, the term "deformation" indicates what is sometimes found as "deformability" in literature, but the former was preferred as the experimental results presented afterwards address a measured response of cells rather than an intrinsic property as the word "deformability" would suggest.

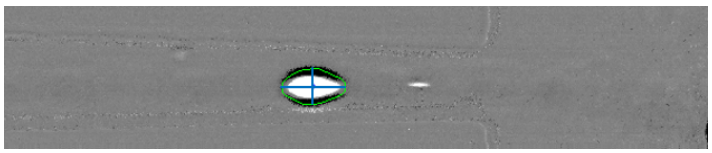

Figure 4.14: Image of a deformed cell showing long and short axes for the calculation of ratio. The green contour was traced by the image processing code, whereas the blue lines were added for sake of clarity to show the axes.

It is important to note that in all cases the deformed cells displayed higher size than reported in data sheets as a consequence of their stretched configuration. This is not an issue - since the parameters of interest cited above are both non dimensional - but it has to be acknowledged as he area is also displayed in results. Another point to take into account for size evaluation is the focusing plane: a slight over-focus was found as optimal condition for subsequent image processing, with a dark halo surrounding the white inside of the cell (Figure 4.15).

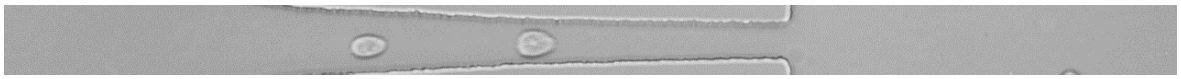

Figure 4.15: Microscopy image showing the over focus configuration of the experiments, with high contrast between the white cell interior part and the black halo at its boundary.

The diameter distribution was plotted for all experimental conditions, showing the predicted size overestimation (an example is shown in Figure 4.16) with respect to the sizes of the tested cells as reported in data sheets (Table 3.3 in Materials and Methods).

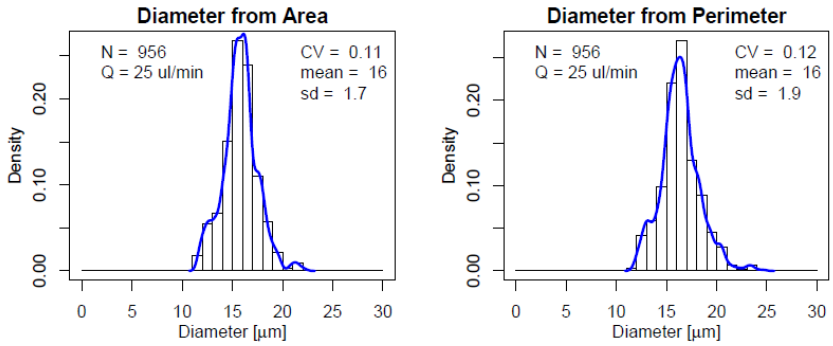

Figure 4.16: Example of diameter distribution calculated from area (left) and perimeter (right) in the recovery section (experimental conditions: Jurkat cells, $L_c = 500\mu m, w_c = 15\mu m$).

As a common practice, experimental data are displayed with mean value and standard error of the mean (typically $mean \pm SD$); in this case though, it was observed that the distribution of deformation values was, in the quasi totality of cases, skewed towards the left with respect to a normal distribution, especially at lower flow rates (Figure 4.17). The dispersion of data was also observed to increase with flow rate,

possibly due to the fact that higher fluid induced forces "activate" the deformation of a more abundant part of the cells flowing through the channel, giving rise to a more heterogeneous response.

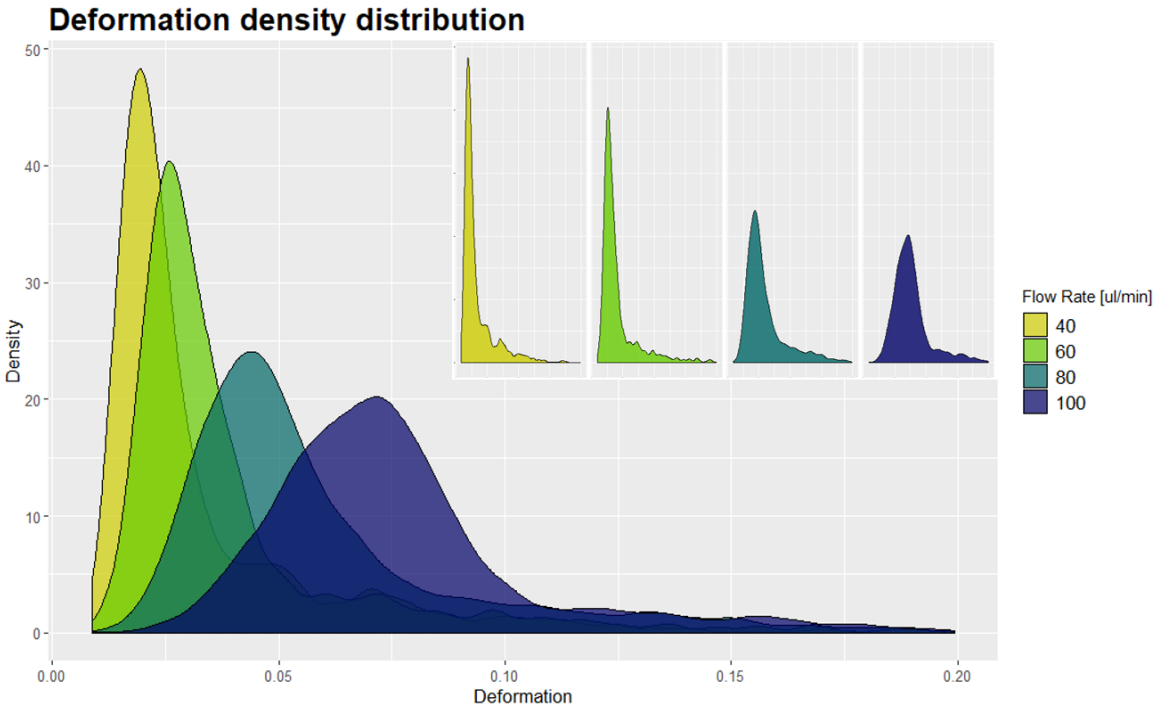

Figure 4.17: Density distribution of deformation for all flow rates. The inset shows the single distributions for sake of clarity. Values refer to the experiments with HL60 cells and the short hyperbolic channel ($L_c = 500\mu m, w_c = 25\mu m$).

Results were visualized as scatter plots of deformation and ratio versus the detected area; since the data had a lot of variability mainly coming from inherent heterogeneity of biological samples, 50% contours of data are displayed, a practice also found in the literature (Otto et al., 2015). As an example, Figure 4.18 shows deformation and ratio scatter plots with a solid black line representing the 50% density contour: the dispersion of data in terms of both size and detected deformation can be inferred from the width of the cloud of points in the x and y directions respectively; the dotted lines locate the centre of distribution of area and deformation. For all experiments, an increase in the deformation was observed with increasing flow rates, in accordance to the increase in the extensional stretching and shear stress expected at higher flow

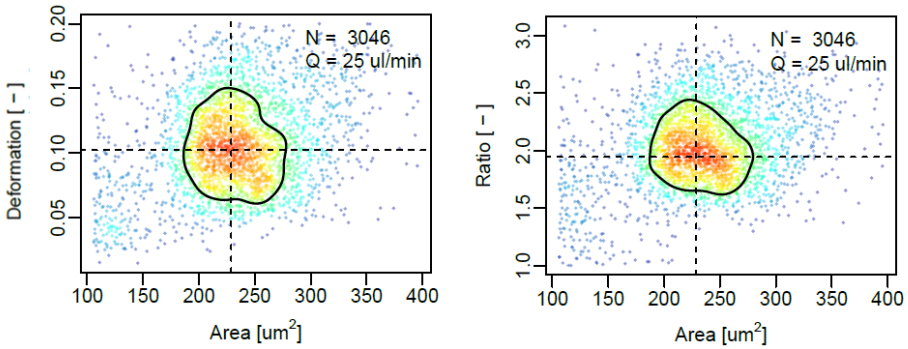

Figure 4.18: Scatter plots of deformation (left) and ratio (right) of Jurkat cells (channel $1000\mu m$ long with $20\mu m$ constriction. Solid lines represent 50% density contours, dotted lines pass through the centre of the distribution, N is the number of experimental points and Q the sample flow rate.

velocity: this was visible from the scatter plots of deformation versus area in all the hyperbolic channels and for both Jurkat (Figure 4.19) and HL60 cells (Figure 4.20). As also observed above (Figure 4.17), data dispersion in terms of deformation increased at increasing flow rate whereas the dispersion in terms of area remained approximately constant at all flow rates.

4.2.1 Deformation and recovery phases

In order to have a clearer idea of the degree of deformation with respect to a control case, the difference between deformation (at the end of the channel) and recovery phase (after the ri-expansion) was investigated. Two separate regions were defined in the images, the first one 200 pixels long at the end of the channel (with a 20X magnification this corresponds to about $80\mu m$), the second one - $100\mu m$ long - for the recovery region placed $100\mu m$ after the ri-expansion to ensure that properly recovered cells were being considered (Figure 4.21).

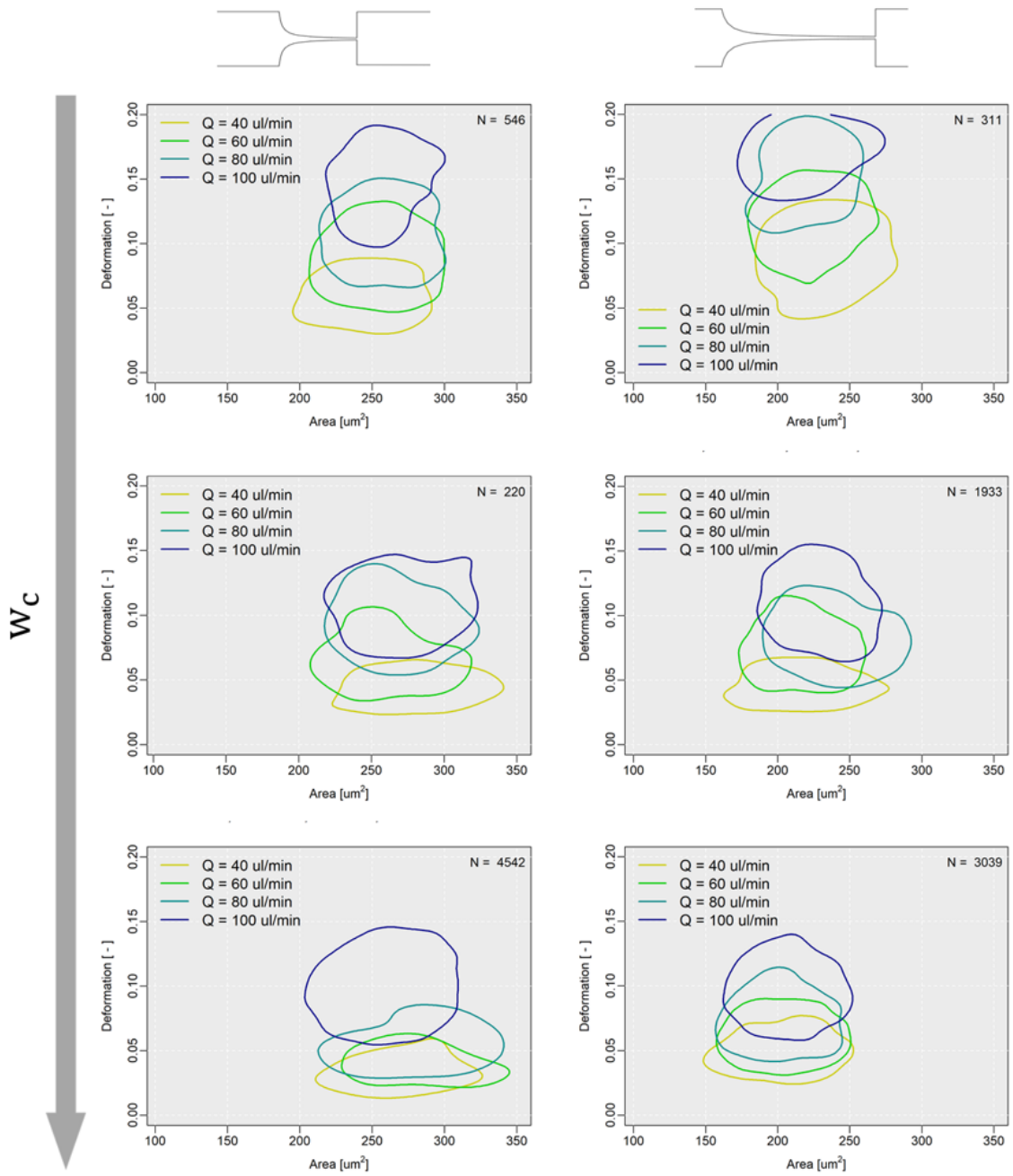

Figure 4.19: Scatter plots of deformation of Jurkat cells in all the channels: the lines represent 50% density contours of deformation in the four flow rates tested for Buffer 0.25. Insets show the channel each plot refers to, with w_c increasing from top to bottom (15, 20 and 25 μm).

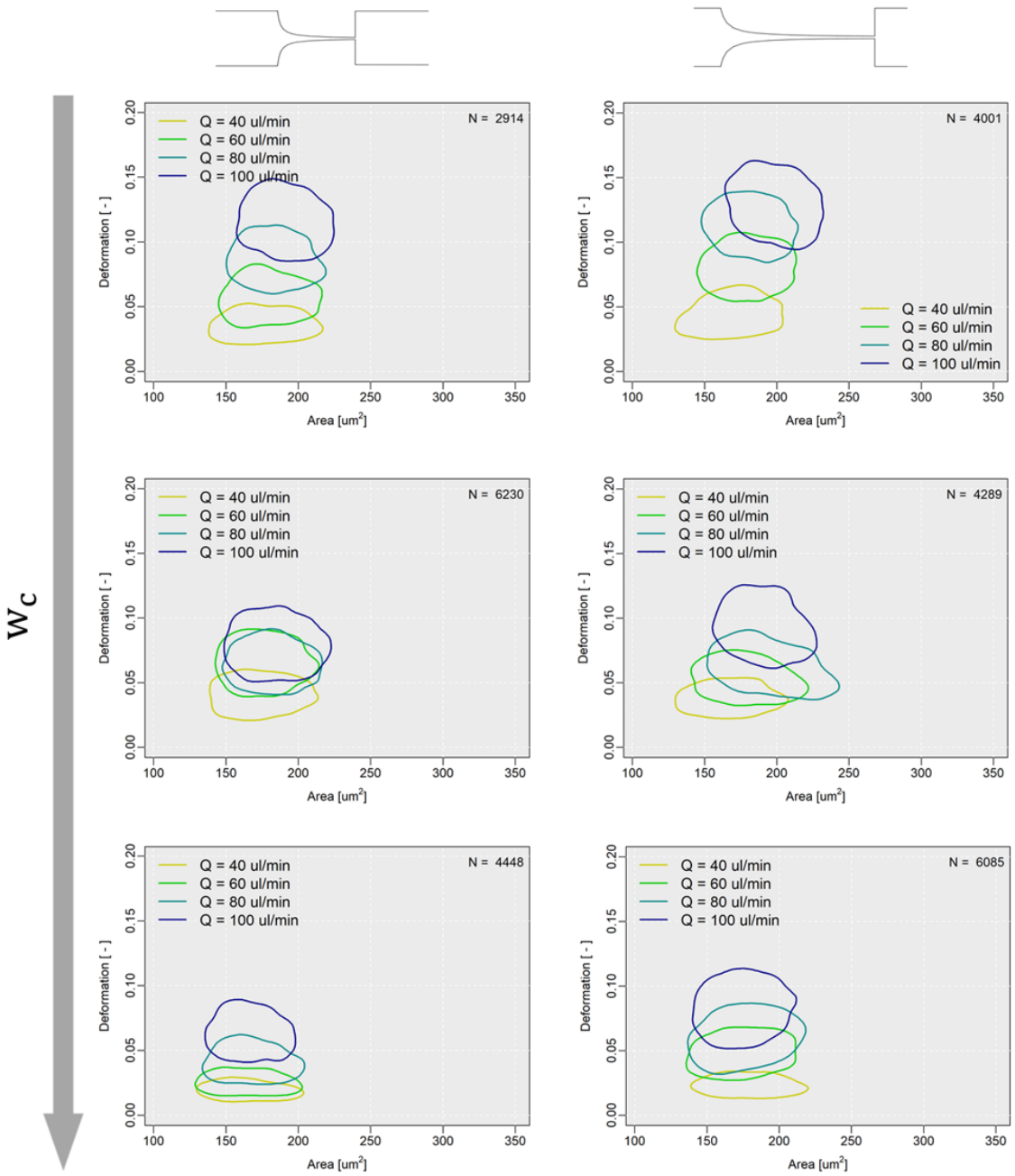

Figure 4.20: Scatter plots of deformation of HL60 cells in all the channels: the lines represent 50% density contours of deformation in the four flow rates tested for Buffer 0.25. Insets show the channel each plot refers to, with w_c increasing from top to bottom (15, 20 and 25 μm).

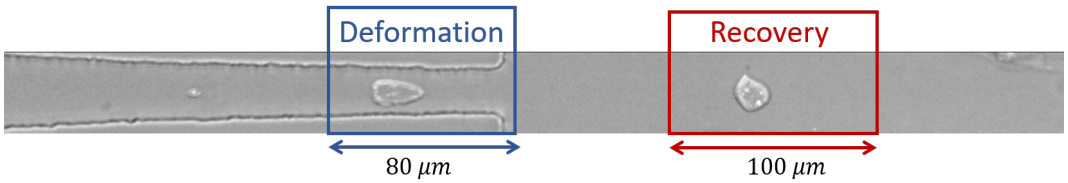

Figure 4.21: Microscopy image showing deformation and recovery regions.

The observation of a recovery phase was more complex in the case of Buffer 0.50 (lower flow rates) since after the abrupt slow down in correspondence with the ri-expansion, cells tended to redistribute spanning the whole enlarged section in the y direction.

This was observed during the experiments but also predicted by observing the velocity streamlines from the simulations, showing the formation of a vortex downstream the contraction in the case of high flow rates and the redistribution of the streamlines in the whole ri-expanded section in the case of lower flow rate (Figure 4.12).

The choice of a narrow ROI (40 to 50μm high), necessary to keep a high frame rate, impeded the observation of a large field in the y direction. For this reason, the recovery was analysed just for Buffer 0.25 where cells still remained in the jet following a linear trajectory even after the ri-expansion.

Despite the narrow region of interest (ROI), sufficiently numerous populations for both phases could be analysed, and a clear distinction between the two identified: predictably, the cases presenting the lowest forces (minimum flow rate) showed overlapping of the deformed and recovered populations, as visible from the scatter plots (Figure 4.22) and from the trend of deformation at increasing flow rate (Figure 4.23). As also visible from the scatter plots of deformation and recovery populations (Figure 4.22), HL60 cells were found to be stiffer than Jurkat cells in all conditions. This was in agreement with a previous work on a cross slot channel in our group (Piergiovanni, 2018) and with AFM studies on these two cell lines that found HL60 cell to have a 18 fold (Rosenbluth et al., 2006) and 2 to 2.4 fold (Lam et al., 2007) larger apparent stiffness.

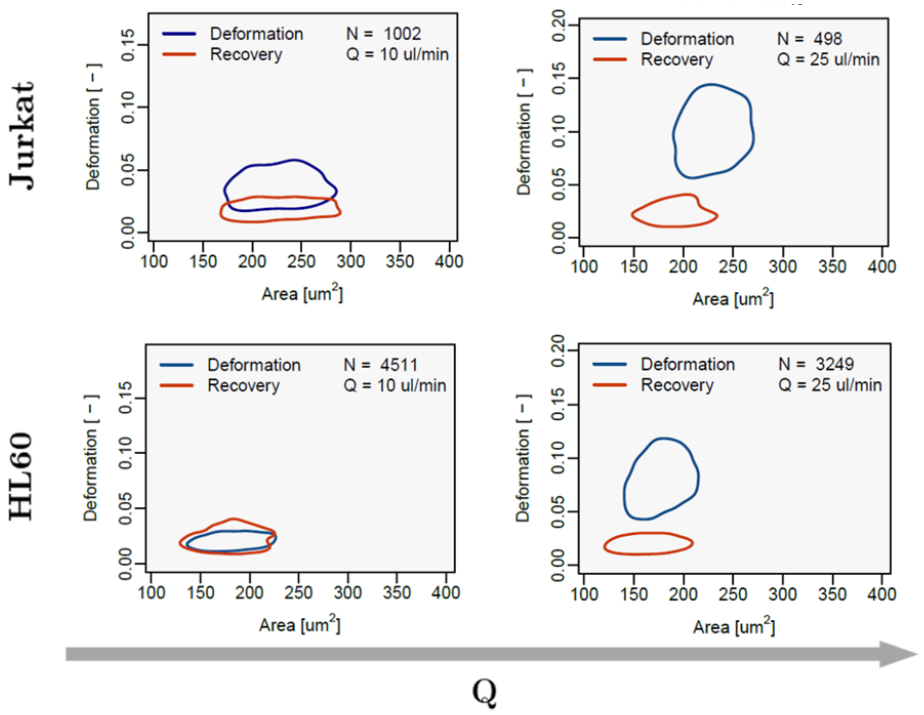

Figure 4.22: Scatter plots of deformation of deformed and recovered cells for Jurkat (top) and HL60 (bottom) at the minimum and maximum flow rates (left to right: $Q_{sample} = 10\frac{\mu l}{min}, Q_{sample} = 25\frac{\mu l}{min}$). Values refer to the short hyperbolic channel with minimum width ($L_c = 500\mu m, w_c = 15\mu m$).

The plots shown do not report error bars as the inherent variability of the cell samples implied large dispersion of data, which was only partially coming from the degree of repeatability of the experiments. In fact, more than one group reported the dependence of cell stiffness on the phase of the life cycle, both via micropipette aspiration (Tsai et al., 1996) and in a microfluidic channel (Otto et al., 2015).

4.2.2 Influence of geometrical parameters

As described above (see Materials and Methods), the height of the device was kept constant at ($20\mu m$) for focusing issues whereas the other sizes were tuned: the length of the hyperbolic section ($L_c = 500\mu m$, $L_c = 1000\mu m$,) and the width at the contraction ($w_c = 15\mu m$, $20\mu m$ and $25\mu m$).

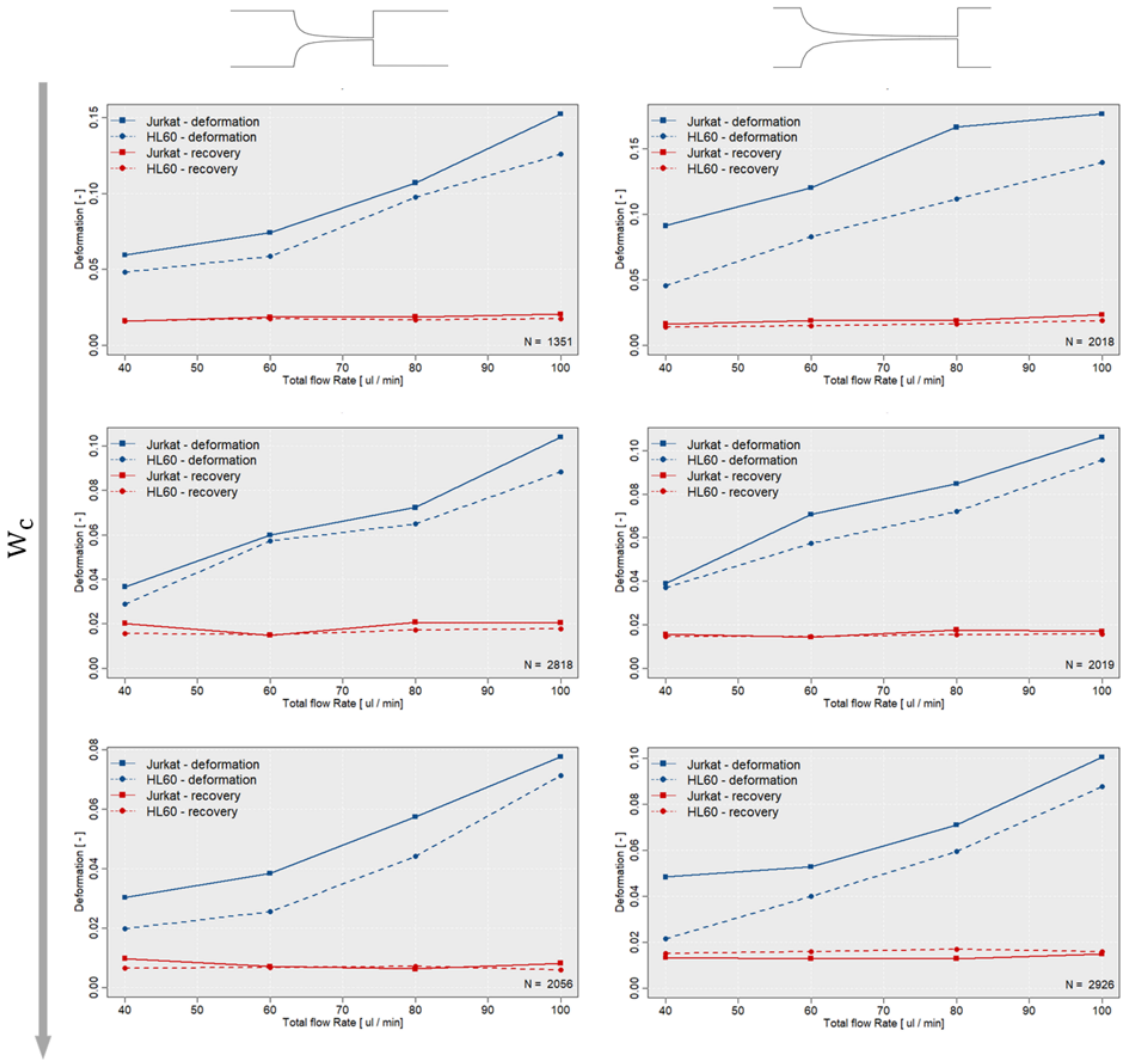

Figure 4.23: Deformation of the two cell lines in deformation and recovery phases, for all flow rates. Experiments were performed with Buffer 0.25. Please note the different scale of y-axis for the case $L_c = 1000\mu m, w_c = 15\mu m$ (top right).

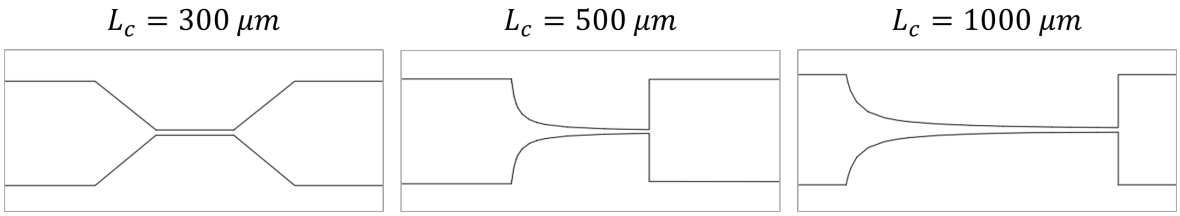

Figure 4.24: CAD design of all the shapes: straight channel, short and long hyperbolic channels (AutoCAD).

The Hencky strain is often found in literature as a quantity describing the induced deformation just by geometrical parameters and increases with decreasing contraction

width (Eq. 2.1 in State of the art). A higher deformation was thus expected in channels with lower w_c: this was observed for all channels, for Buffer 0.25 (Figure 4.25) and Buffer 0.50 (Figure 4.27).

As for the length of the hyperbolic part, the $1000\mu m$ long channel nearly resembled a straight channel in the last section, whereas for $L_C = 500\mu m$ a pronounced curvature existed (Figure 4.24).

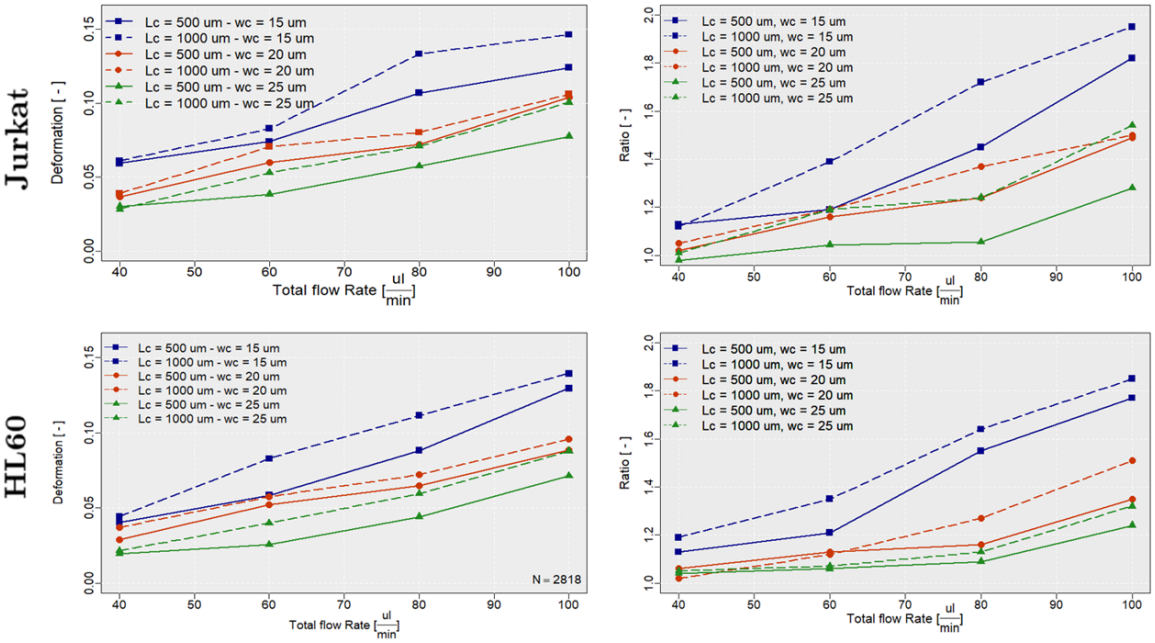

Figure 4.25: Comparison of the deformation among channels of different length and width for Jurkat (top) and HL60 (bottom) cell lines. All data refer to the experiments with Buffer 0.25.

For the long channels, a higher deformation was expected given the lower cross section in the last part of the channel, with a significant shear stress experienced by the cells in the vicinity of the walls: this was observed for all the widths and for both cell lines (Figure 4.25, plain vs dotted lines). The ratios reported the same pattern with long hyperbolic channels yielding a greater deformability with respect to the short ones. For larger widths ($w_c = 20\mu m, w_c = 25\mu m$) no deviation from the rest configuration was detected at the minimum flow rate ($ratio \approx 1$), whereas at higher flow rates an

evident stretching was observed. Cells flowing in the channel with the lowest width at the contraction ($w_c = 15\mu m$) reported some stretching already at the minimum flow rate, and a pronounced ratio at higher speed.

It was not clear whether the deformation induced in the straight channel was higher with respect to the hyperbolic case, since it was found to be so for Jurkat cells, but not for HL60 (Figure 4.26, left panel). On the contrary, the ratio for the straight channel appeared higher with respect to the hyperbolic channels with the same width $w_c = 20\mu m$ for HL60 cells and similar to the one of long hyperbolic channel for Jurkat cells (Figure 4.26, right panel).

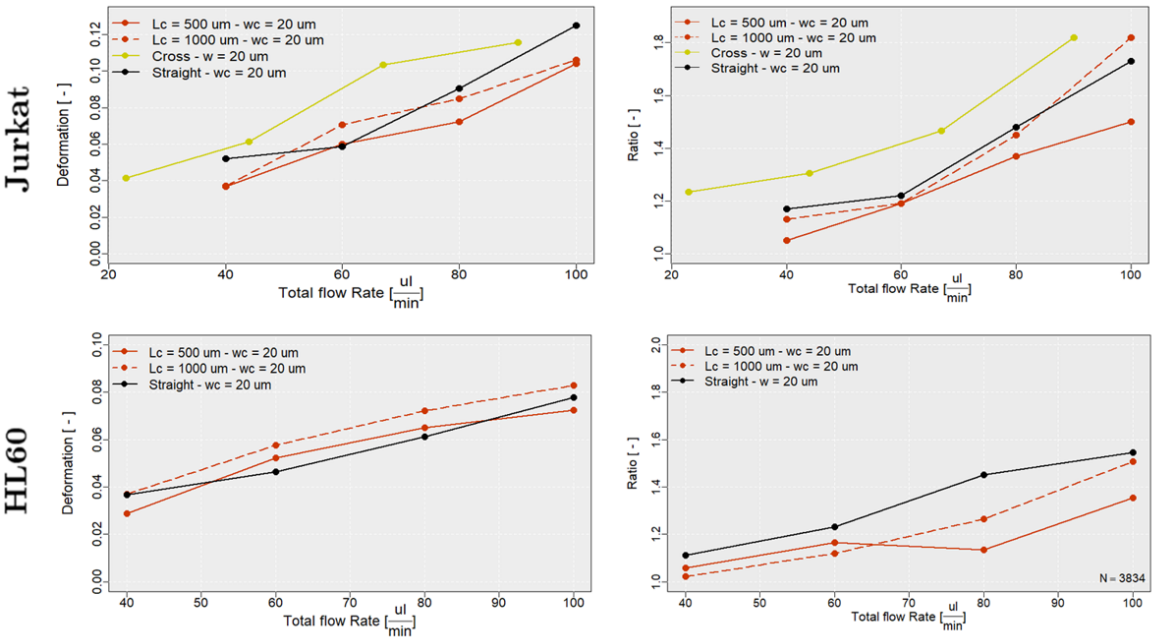

Figure 4.26: Comparison of the deformation between straight and hyperbolic channels (and cross shaped channel) for Jurkat (top) and HL60 (bottom).

The values of ratio were compared to the ones reported in studies with cross shaped devices: in a cross section of $60\mu m$ x $30\mu m$ with PBS flowing at $Q = 800\frac{\mu l}{min}$ (mean velocity in the centre of about $3.4\frac{m}{s}$) a ratio of 1.33 was reported for Jurkat cells (Dudani et al., 2013) and ratios ranging from 1.26 to 1.34 and from 1.23 and 1.34 for HL60 and Jurkat cells respectively were found in a previous work in our group for a cross section of $30\mu m$ x $30\mu m$ with PBS flowing at mean velocities up to $2\frac{m}{s}$ (Piergiovanni, 2018).

In the present work, the cross sections at the contraction ranged from 300 to 500 μm^2 and at the maximum flow rate the corresponding mean fluid velocities at the contraction were 5.55, 4.17 and 3.34 $\frac{m}{s}$: the larger intensity of deformation and ratio with respect to the previous work in our group likely depended on two factors: Firstly, the higher mean velocities and higher viscosity of Buffer 0.25 with respect to PBS (at higher shear rates around 3 $mPa\ s$, see Figure 3.6 in Materials and Methods), and secondly the addition of the shear effect that was essentially absent in the cross shaped devices and of the sheath flow confining the cells in a narrow centre stream of high stresses could have contributed to this observation. The complete report of ratios is available in Appendix C.

To confirm the effect of viscosity on the observed deformation and ratio, experiments on a cross shaped device with $20\mu m$ x $20\mu m$ cross section were performed and compared to the values found previously in our group (Piergiovanni, 2018) with flow rates scaled to get the same mean fluid velocity: ratios between 1.33 and 1.92 and were detected for the cross shape device, even higher than the ones in the hyperbolic channels (Figure 4.26, top right): indeed, despite the absence of shear, the cross shaped device featured a much higher extensional effect with respect to the hyperbolic channels (see Appendix B for the values regarding the cross shape device and Appendix A for the other channels).

The same relationships between the different channels were reported also for the case of Buffer 0.50 (Figure 4.27): the difference in the deformation between short and long channels with higher width ($w_c = 20\mu m$) was less evident with respect to the case of $w_c = 15\mu m$.

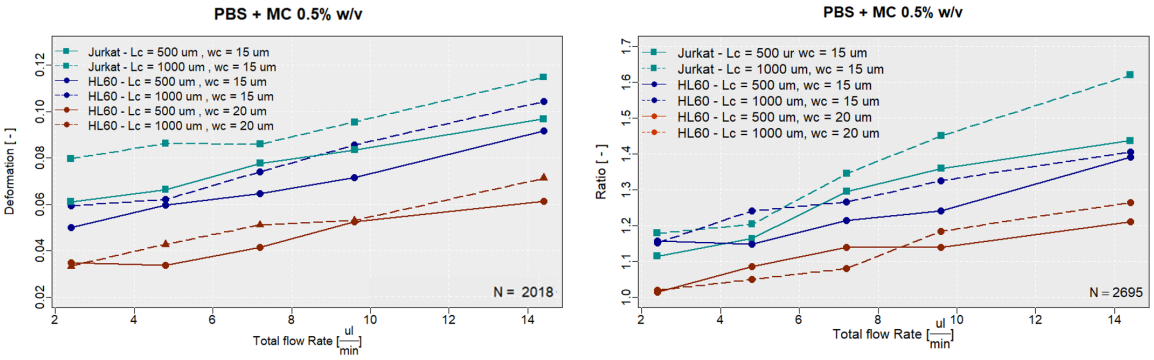

Figure 4.27: Comparison of the deformation among channels of different length and width for Jurkat (cyan) and HL60 (blue and red). All data refer to the experiments with Buffer 0.50.

Similar values of deformation were found for HL60 cells flowing through a straight channel of $20\mu m$x$20\mu m$ cross section at similar flow rates and with the same fluid as Buffer 0.50, with values ranging from 0.03 to 0.08 (Otto et al., 2015). Another work making use of a larger straight channel ($30\mu m$x$30\mu m$) at much lower flow rate ($Q = 8\frac{nl}{s} = 0.48\frac{\mu l}{s}$) and higher buffer viscosity (PBS + MC 1.0% w/v) reported deformations between 0.01 and 0.02 for HL60 cells, that is reasonably comparable to the values obtained here once taken into account the difference in velocity.

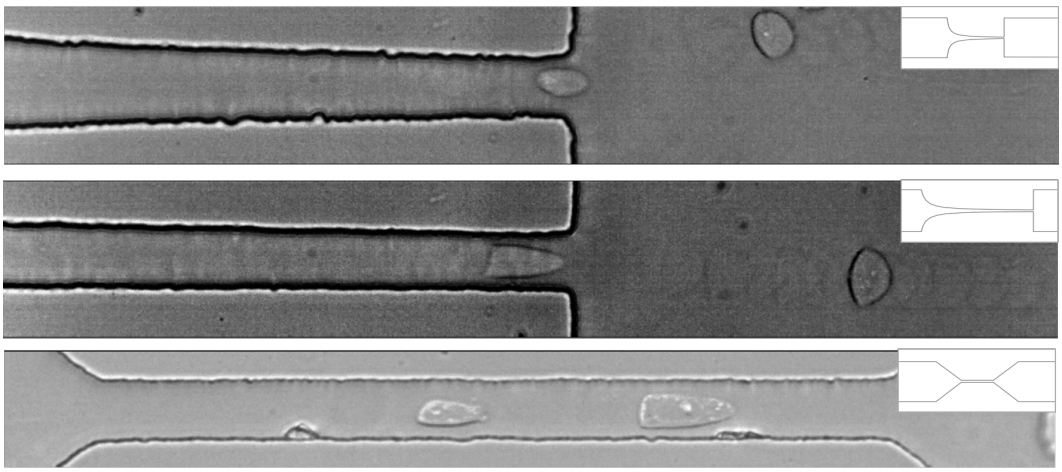

Figure 4.28: Different deformation modes in channels of different shape: the first two images (top to bottom) were taken from recordings with 40X objective on the hyperbolic channels ($w_c = 15\mu m$) whereas the bottom image shows cells flowing in the straight channel.

Interestingly, the deformation mode in the case of "truly" hyperbolic channel ($L_c = 500\mu m$) and "straight" resembling channel ($L_c = 1000\mu m$) was remarkably different, with cells displaying an ellipse like shape in the former and a bullet shape in the latter (Figure 4.28). The bullet shape with the front of the cells protruding in the flow direction and the flattened rear is typical of cells flowing in a straight channel (Figure 2.9 in State of the art).

4.2.3 Statistical analysis

To confirm that the variation of geometrical parameters truly induced a difference in deformation, a non parametric *Mann-Whitney test* was performed taking into account, for all shapes, the maximum flow rate ($Q_{tot} = 100\frac{\mu l}{min}$ for Buffer 0.25, $Q_{tot} = 14.4\frac{\mu l}{min}$ for Buffer 0.50). The choice of this test was driven by the observation of the strong deviation of data from a normal distribution (as shown previously in Figure 4.17 on page 87).

Despite the large number of points for each experiments could suggest the applicability of a parametric *t-test* anyway, the former was preferred as it evaluates the distributions, not the value of the mean (which was not used to display results as not representative of the population). The robustness of such test was not an issue as in all cases a large number of measurement points was available ($N > 1000$).

The comparison among different channels showed that no significant difference between straight and short hyperbolic channel of the same width ($L_c = 500\mu m, w_c = 20\mu m$) whereas the corresponding long channel ($L_c = 1000\mu m, w_c = 20\mu m$) had a different deformation with respect to the straight channel, as observed for both cell lines (Figure 4.29, Figure 4.30).

Channels of the same width and different lengths reported no difference in deformation for Jurkat cells (Figure 4.29) but did instead for HL60 cells (Figure 4.30).

By comparing channels with the same length and varying width, a statistically signific-

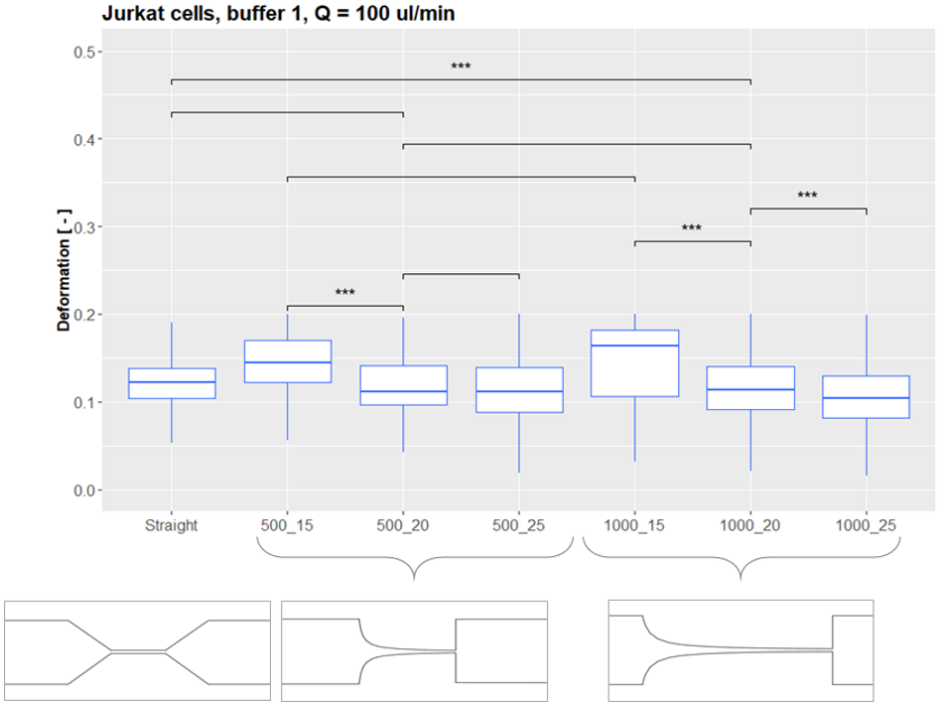

Figure 4.29: Statistical analysis for channels of different shape and size for Jurkat cells. Values refer to the experiments with Buffer 0.25 and maximum flow rate $Q_{tot} = 100\frac{\mu l}{min}$. Brackets show the compared populations and stars the significance level ($* : p < 0.05$,$** : p < 0.01$,$*** : p < 0.001$,$**** : p << 0.001$). No stars are displayed when the test returned a non significant *p-value*.

ant difference in the deformation was found between $w_c = 15\mu m$ and $w_c = 20\mu m$ and between $w_c = 20\mu m$ and $w_c = 25\mu m$ for all cases (both cell lines, both lengths) except for Jurkat cells in the case $L_c = 500\mu m, w_c = 20\mu m$ VS $L_c = 500\mu m, w_c = 25\mu m$ (Figure 4.29).

The same test was performed to assess the difference between the two cell lines in the same condition (same channel and same flow rate). In the case of Buffer 0.25, for the lowest and highest total flow rates ($Q_{tot} = 40\frac{\mu l}{min}, Q_{tot} = 100\frac{\mu l}{min}$) the deformation was always significantly different between HL60 and Jurkat cells except for the case of $L_c = 1000\mu m, w_c = 15\mu m$ (Figure 4.31).

With the more viscous Buffer 0.50, only the channels with $w_c = 15\mu m$ could be compared and in both of them there was a statistically significant difference between the deformation of the two cell lines at the lowest and highest flow rates (Figure 4.32).

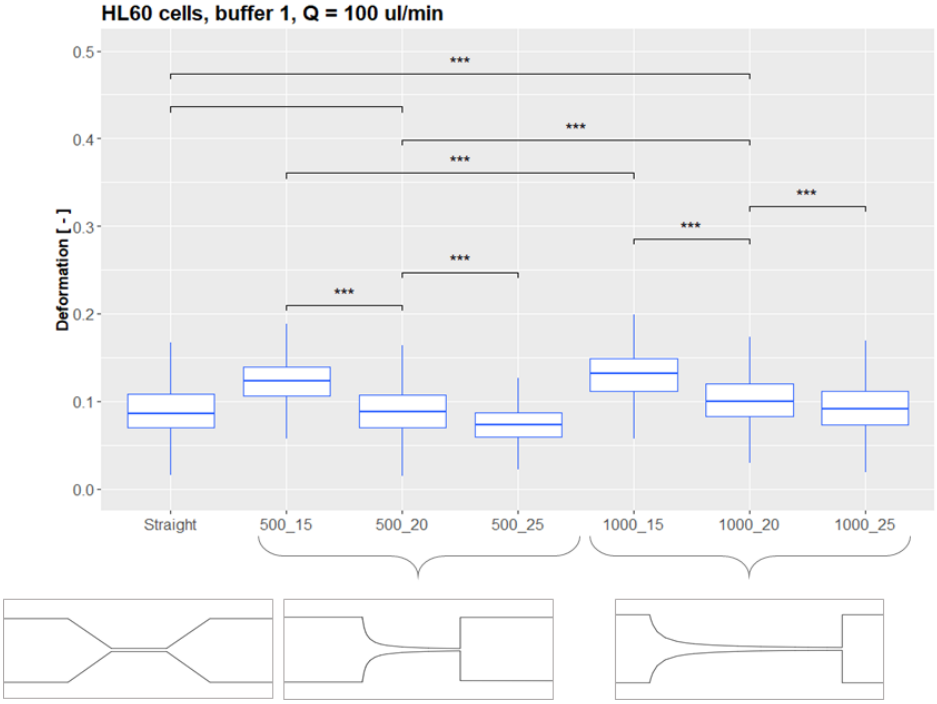

Figure 4.30: Statistical analysis for channels of different shape and size for HL60 cells. Values refer to the experiments with Buffer 0.25 and maximum flow rate $Q_{tot} = 100\frac{\mu l}{min}$. Brackets show the compared populations and stars the significance level ($^{*}: p < 0.05, ^{**}: p < 0.01, ^{***}: p < 0.001, ^{****}: p << 0.001$). No stars are displayed when the test returned a non significant *p-value*.

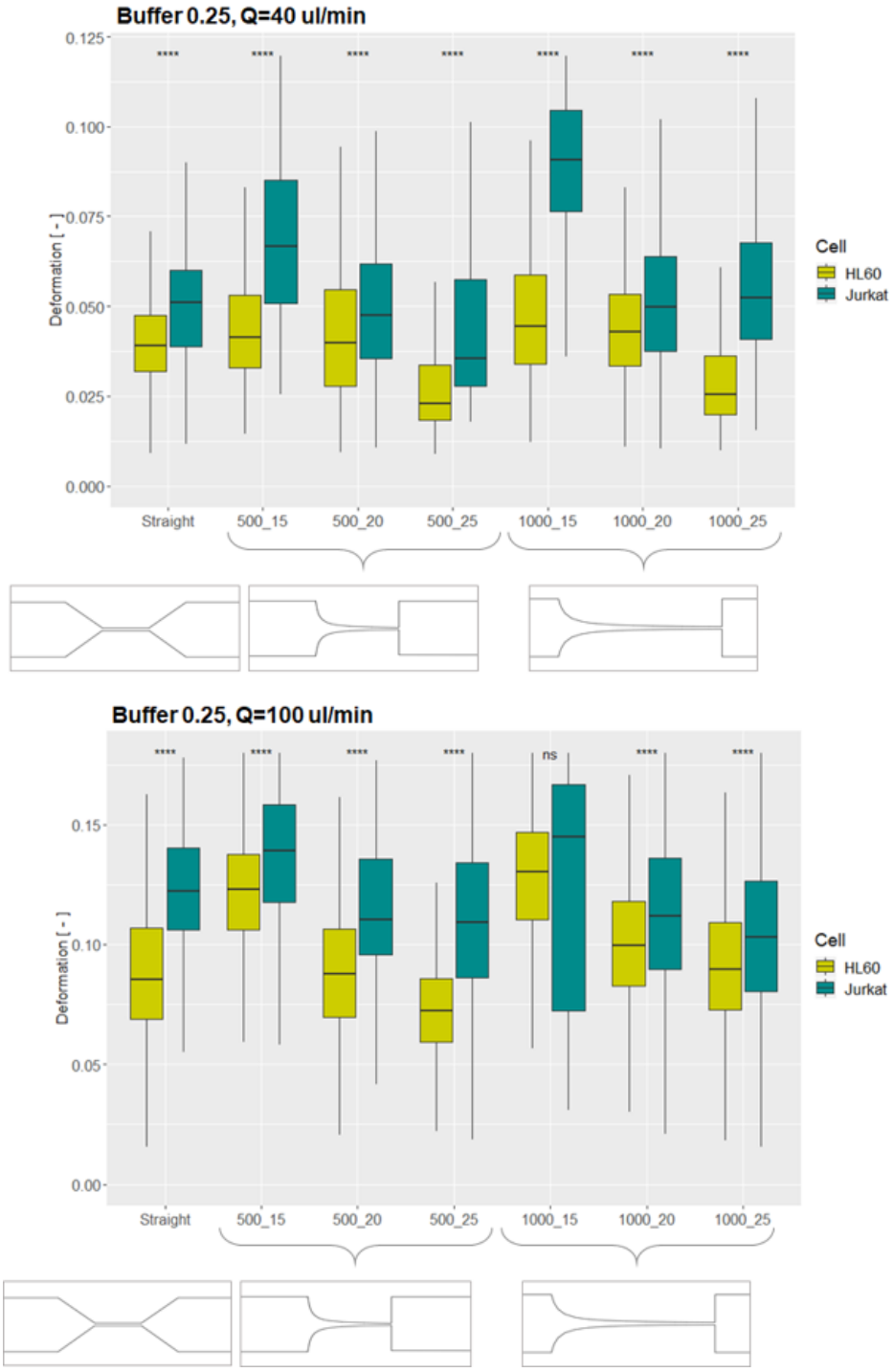

Figure 4.31: Statistical analysis for the two cell lines at minimum and maximum flow rates (top to bottom). Values refer to the experiments with Buffer 0.25. Brackets show the compared populations and stars the significance level ($* : p < 0.05$,$** : p < 0.01$,$*** : p < 0.001$,$**** : p << 0.001$). No stars are displayed when the test returned a non significant *p-value*.

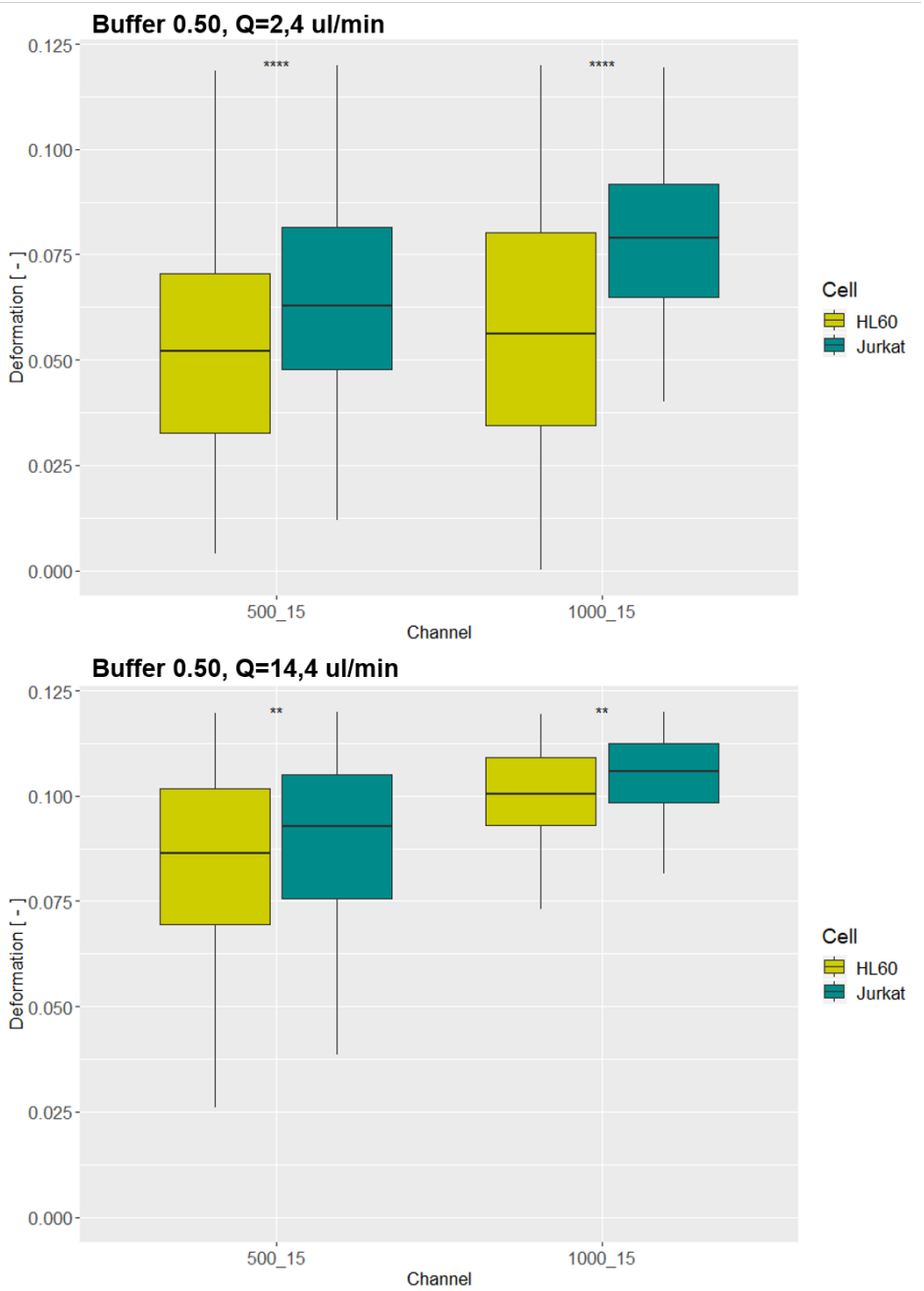

Figure 4.32: Statistical analysis for the two cell lines at minimum and maximum flow rates (top to bottom). Values refer to the experiments with Buffer 0.50. Brackets show the compared populations and stars the significance level (* : $p < 0.05$,** : $p < 0.01$,*** : $p < 0.001$,**** : $p << 0.001$). No stars are displayed when the test returned a non significant *p-value*.

4.2.4 Space dependent deformation and recovery

In the hyperbolic channels, the cross section progressively shrank in the y direction from $w_u = 400\mu m$ to $w_c = 15 \div 25\mu m$ (with constant height $z = 20\mu m$), thus an increase in deformation along the channel was expected due to the increase in velocity and fluid induced stresses. This was investigated in the maximum deformation scenario, i.e. in the long hyperbolic channels with narrowest width at the contraction ($L_c = 1000\mu m, w_c = 15\mu m$) along three equidistant sections (each $200\mu m$ long, gap $70\mu m$). An increase in deformation proceeding towards the end of the channel was reported for both cell lines, in particular, in each section nearly double the deformation of the previous one was recorded (as shown by the values of percentage increase in the table in Figure 4.33).

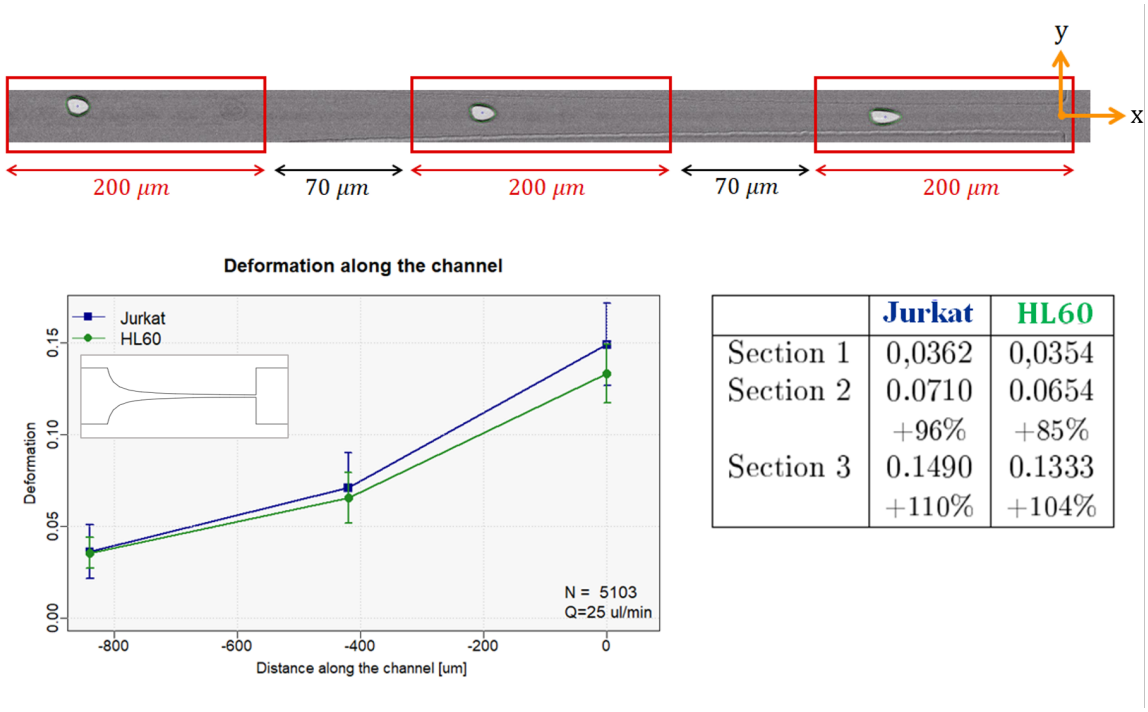

	Jurkat	HL60
Section 1	0,0362	0,0354
Section 2	0.0710	0.0654
	+96%	+85%
Section 3	0.1490	0.1333
	+110%	+104%

Figure 4.33: Evaluation of the deformation in sections along the hyperbolic channel in the maximum stresses scenario ($L_c = 1000\mu m, w_c = 15\mu m$, maximum flow rate $Q_{tot} = 100\frac{\mu l}{min}$). The top figure shows the partition of the channel for the calculation (with the flow going from left to right); the coordinate system is placed in correspondence with the contraction (shown in orange). The results displayed in the plot are peak values of the deformation distribution in each zone, reported in the table at the right with percentage increase with reference to the previous zone.

Similarly, the space dependent recovery of cells in the ri-expansion was evaluated for the higher flow rates (Buffer 0.25) since at very low velocities cells tended to redistribute spanning the whole ri-expansion width, while at higher speed a jet was formed and cells were retained herein. Moreover, in the former case cells were observed to "collapse" one onto the other and group together, hindering an appropriate evaluation of their contours with image processing and, more importantly, deviating from the hypothesis of "single cell analysis", with clear reciprocal influence on the deformation mode.

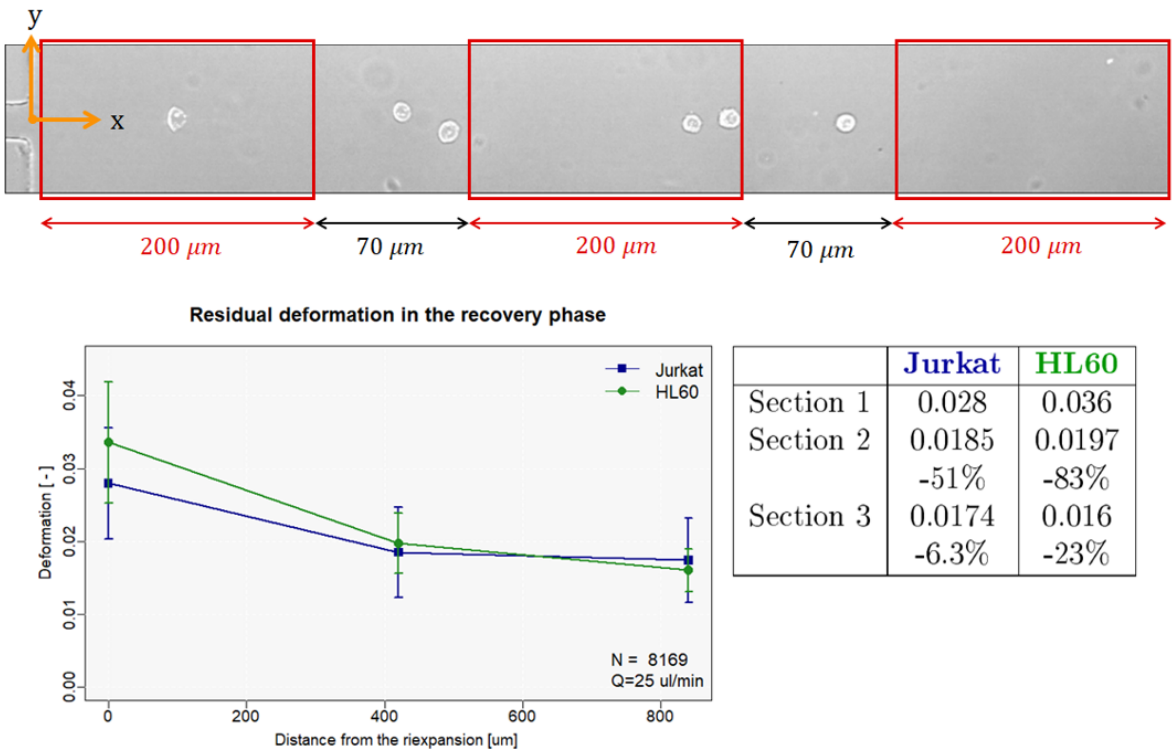

	Jurkat	HL60
Section 1	0.028	0.036
Section 2	0.0185	0.0197
	-51%	-83%
Section 3	0.0174	0.016
	-6.3%	-23%

Figure 4.34: Evaluation of the residual deformation in the recovery phase in the maximum stresses scenario ($L_c = 1000\mu m, w_c = 15\mu m$, maximum flow rate $Q_{sample} = 25\frac{\mu l}{min}$).
The top figure shows the partition of the channel for the calculation (with the flow going from left to right); the coordinate system is placed in correspondence with the contraction (shown in orange). The results displayed in the plot are peak values of the deformation distribution in each zone, reported in the table at the right with percentage decrease with reference to the previous zone.

The chosen ROI was $120\mu m$ high $140\mu m$ long (maximum available length as in all other experiments, since the frame rate just depends on the height) and three distinct

sections were identified analogously to what done in the evaluation of the deformation along the channel.

A comparison of the behaviour of HL60 and Jurkat cells showed that the stiffer cell line (HL60) preserved a higher deformation in the very first part of the ri-expansion after the maximum stress point (that is, where $w = w_c$). For both cell lines, there was a much lower difference in deformation between the last two sections, suggesting that recovery mostly took place early downstream the ri-expansion (Figure 4.34). The recovery mode was also investigated at different flow rates and for the three widths at the contraction (Figure 4.35): at lower flow rates, the wider channels ($w_c = 20\mu m, w_c = 25\mu m$) did not show any difference between each another nor among the three sections, whereas at $Q_{tot} = 80$ and $100\frac{\mu l}{min}$ cells still had a degree of deformation in the first section. For all cases, the deformation in the last section was very low and roughly equal in all channels and at all flow rates, suggesting that in this part nearly full recovery was achieved.

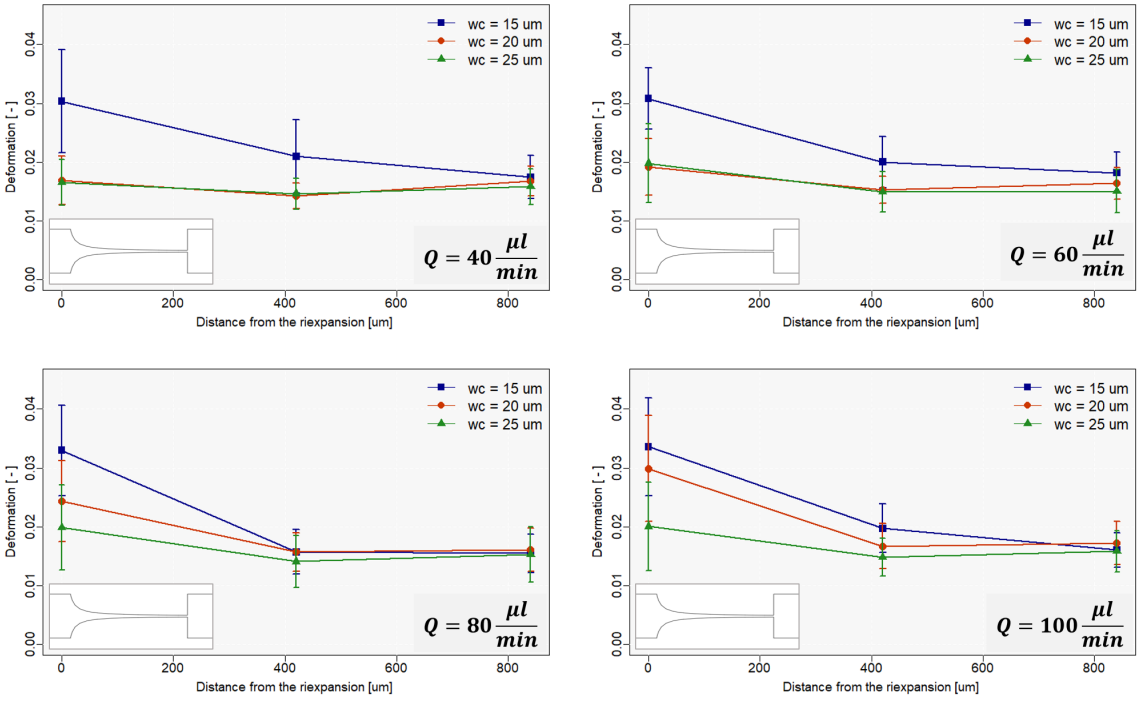

Figure 4.35: Evaluation of the residual deformation in the recovery phase in the long hyperbolic channel ($L_c = 1000\mu m$) for the three widths and at all flow rates.

To have an insight into the magnitude of the cell velocity in the sections of the hyperbolic channels and in the recovery part, this was calculated as follows:

$$v_{cell} = \frac{(x_2 - x_1) \cdot 0.36 \frac{\mu m}{pixel}}{\Delta t} \tag{4.6}$$

where x_1, x_2 indicate the position of the cell in two subsequent frames (measured with ImageJ, see Figure 4.36) scaled by the conversion from pixel to microns (for 20X magnification) and Δt the time step between two frames, that is

$$\Delta t = \frac{t_{tot}}{\text{frame rate}} \tag{4.7}$$

with t_{tot} the total duration of each movie. The frame rate was 10000 fps in the recordings of the channel part (ROI $45\mu m$ high) and 5000 fps in the recordings of the ri-expansion part (ROI $130\mu m$ high).

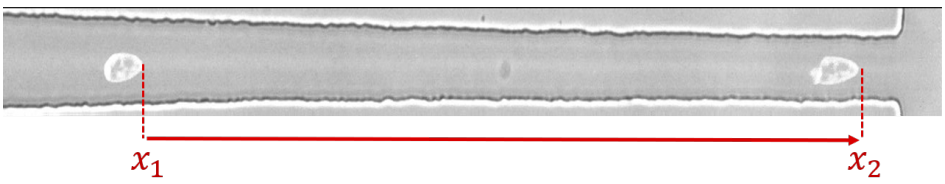

Figure 4.36: Calculation of the cell velocity from the recorded images: approximately the same point of a cell in two subsequent positions was taken and the distance in pixel calculated.

For the recovery part, the velocity was evaluated just downstream the ri-expansion when cells still followed a straight path inside the jet. Table 4.3 displays the values referring to the maximum velocities scenario ($w_c = 15\mu m$) for HL60 cells at all flow rates. At lower flow rate, the difference between the velocity in the channel and in the recovery phase was more evident, whereas at higher flow rate the slowing process was smoother, as if cells retained the high momentum imparted for a longer time.
This was also clearly visible from the recordings: in the case of $Q = 100 \frac{\mu l}{min}$ cell were still proceeding along a roughly straight trajectory up to $800\mu m$ downstream the ri-

expansion, whereas at lower flow rate their spread along the y direction was more evident.

	$v_{cell}\left[\frac{m}{s}\right]$	
$Q_{tot}\left[\frac{\mu l}{min}\right]$	**Deformation**	**Recovery**
40	2.1168	0.576
60	2.5272	0.7776
80	2.8944	1.296
100	3.528	1.6704

Table 4.3: Cell velocities in the contraction and ri-expansion parts. Values refer to experiments on HL60 cells with the long hyperbolic channel ($L_c = 1000\mu m, w_c = 15\mu m$).

4.2.5 Influence of the fluid

The deformation in different fluid dynamic conditions was compared, with flow rates changing based on the viscosity of the buffer: the detailed description of the protocol is given in Materials and Methods and the maximum flow rates corresponding to each buffer are reported in Figure 4.4 (for all conditions $Q_{sheath} = 3 \cdot Q_{sample}$, hence $Q_{tot} = 4 \cdot Q_{sample}$).

Buffer	**MC Concentration**	**Maximum flow rate**
Buffer 0.25	0.25% w/v	$Q_{tot} = 100\frac{\mu l}{min}$
Buffer 0.37	0.37% w/v	$Q_{tot} = 60\frac{\mu l}{min}$
Buffer 0.50	0.50% w/v	$Q_{tot} = 14.4\frac{\mu l}{min}$

Table 4.4: Maximum total flow rate for each buffer.

The effect of viscosity was readily evident by observing the difference in deformation between Buffer 0.25 and Buffer 0.37 at the same flow rates ($Q_{tot} = 40\frac{\mu l}{min}$, $Q_{tot} = 60\frac{\mu l}{min}$); also, deformation at around $Q_{tot} = 15\frac{\mu l}{min}$ (the maximum flow rate for Buffer 0.50) was even higher than the deformation with Buffer 0.37 at $Q_{tot} = 20\frac{\mu l}{min}$ (Figure 4.37).

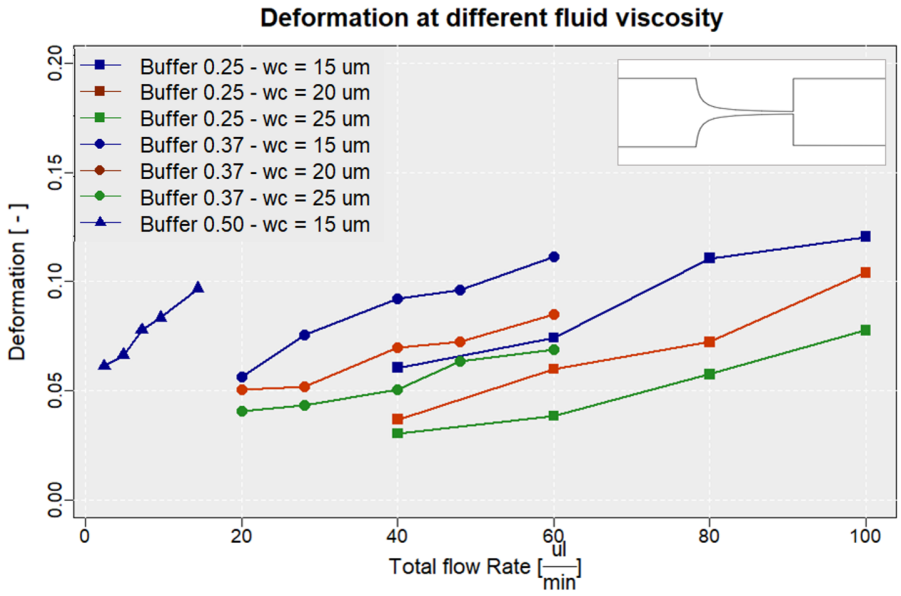

Figure 4.37: Influence of buffer viscosity on deformation of Jurkat cells. Values refer to the short hyperbolic channel ($L_c = 500\mu m$, shown in inset).

4.2.6 Influence of treatments for the modification of cellular stiffness

Fixation with formalin

Deformation of fixed cells for the two cell lines showed to be significantly smaller than the corresponding control in all cases (Figure 4.38), confirming the expected stiffening effect of the formalin treatment due to the permanent cross-linking of cellular proteins. This effect has been already proved in several studies: AFM on K562 cells showed a 57 times higher Young Modulus for fixed cells with respect to the control (Wang et al., 2013); in a cross shaped microchannel inducing extensional flow on glioblastoma tumour initiating cells and 3T3 cells a 58 to 66% increase in the derived shear modulus (Guillou et al., 2016) and in a similar device on HeLa cells (Gossett et al., 2012).

Notably, a small yet non zero deformation was observed for fixed cells, which reported the same behaviour as their respective controls, with HL60 being stiffer than Jurkat

(Figure 4.38). Values of deformation for were three to four times smaller than the control for Jurkat cells and up to ten times smaller for HL60 cells (Table 4.5).

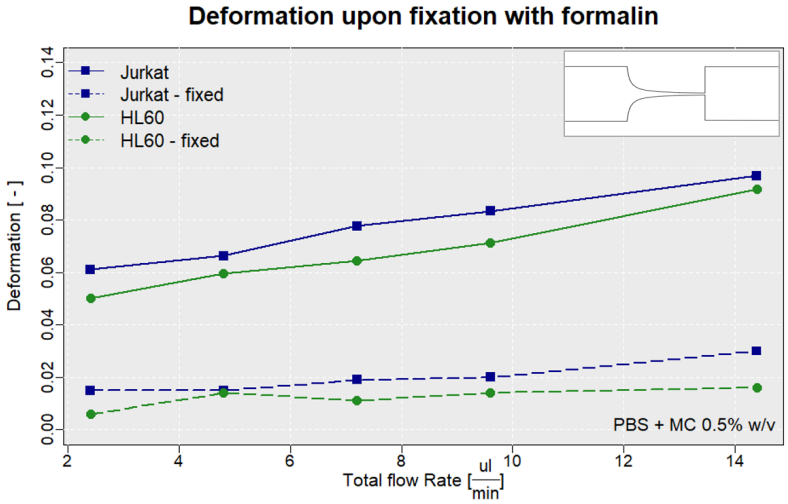

Figure 4.38: Deformation of Jurkat (blue) and HL60 (green) for the short hyperbolic channel with $w_c = 15\mu m$ (shown in inset). Control cases are represented in solid lines, whereas fixed cases are plotted with dashed lines.

		$Q_{tot}[\frac{\mu l}{min}]$				
		2.4	4.8	7.2	9.6	14.4
Jurkat	Control	0.061	0.066	0.078	0.083	0.097
	Fixed	0.015	0.015	0.019	0.019	0.030
		(3.33)	(3.93)	(3.42)	(3.74)	(3.07)
HL60	Control	0.050	0.059	0.065	0.071	0.092
	Fixed	0.006	0.014	0.011	0.014	0.016
		(10.2)	(4.72)	(7.09)	(5.93)	(6.06)

Table 4.5: Values of deformation for fixed cells with respect to the control cases with ratios of control over fixed cells deformation shown in parentheses.

Cytoskeletal disruption with cytochalasin D

The observed deformation upon administration of an increasing dose cytochalasin D on Jurkat cells showed an initial visible increment followed by a plateau for the higher concentrations. Cyto D concentration was increased tenfold for each experiment, whereas DMSO quantity was kept constant in all experiments to avoid any additional

effect on the measured deformation (see Materials and Methods).

The experiments were performed on the channel which gave the highest deformation ($L_c = 1000\mu m, w_c = 15\mu m$) and Buffer 0.50. Three measurements were performed for each of the four concentrations and three flow rates: $Q_{tot} = 2.4\frac{\mu l}{min}, 7.2\frac{\mu l}{min}, 14.4\frac{\mu l}{min}$. The normalized deformation with respect to the control (no drug) showed an increasing trend with increasing concentration with a plateau for the two highest concentrations (Figure 4.39): as also reported in the same experiments on HL60 flowing through a straight channel, deformation stabilizes above a certain concentration, likely due to complete cytoskeletal actin disruption (Otto et al., 2015). At the lowest flow rate, this plateau was already reached from $0.1\mu M$ on, whereas at $Q_{tot} = 7.2\frac{\mu l}{min}$ and $Q_{tot} = 14.4\frac{\mu l}{min}$ a sort of "step" was found between $0.1\mu M$ and $1\mu M$ cyto D concentrations, with a less steep increase in the last step ($1\mu M$ to $10\mu M$).

the exact values of the mean normalized deformation for each concentration of cytoD are reported in Table 4.6.

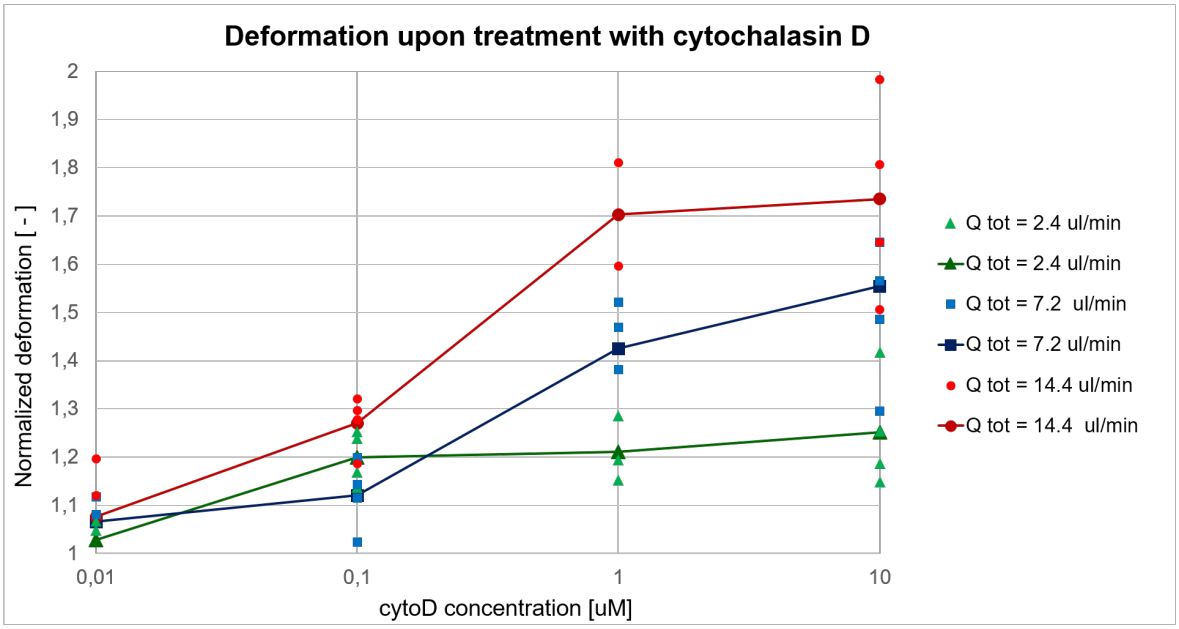

Figure 4.39: Normalized deformation upon treatment with cytochalasin D: experimental points at the three flow rates are shown and the solid lines interpolate the mean value for each condition. A logarithmic scale was used for the x-axis to allow for better visualization of the low concentration points.

The softening effect of such drug was already reported in a study on leukaemia derived cell lines, making use of both AFM and a microfluidic network of constriction channels: upon treatment with the same chemotherapeutic drug, addition of $2\mu M$ cytochalasin D resulted in a fivefold and sixfold decrease in stiffness for HL60 and Jurkat cells respectively (Lam et al., 2007).

A flow rate dependent increase in deformation on cells treated with $10\mu M$ cyto D in a cross slot device was also reported, with treated cells (glioblastoma tumour initiating cells and 3T3 fibroblasts) presenting extracted shear moduli 50% higher to twice as large as the control (Guillou et al., 2016).

		cytoD $[\mu M]$			
		0.01	0.1	1	10
$\boldsymbol{Q_{tot}}\left[\frac{\mu l}{min}\right]$	2.4	1.03 ± 0.05	1.20 ± 0.06	1.19 ± 0.07	1.25 ± 0.12
	7.2	1.05 ± 0.06	1.12 ± 0.07	1.42 ± 0.07	1.55 ± 0.15
	14.4	1.07 ± 0.15	1.27 ± 0.59	1.70 ± 0.12	1.73 ± 0.24

Table 4.6: Values of the normalized deformation upon treatment with cytochalasin D (mean ± SD).

Notably, the obtained values were slightly higher than the ones found for HL60 cells flowing in a straight channel of section $20\mu m$ x $20\mu m$ at similar flow rates (normalized deformation upon treatment ~ 1.45 at $Q = 0.12\frac{\mu l}{s} = 7.2\frac{\mu l}{min}$) (Otto et al., 2015), likely due to the smaller cross section used in the present experiments ($15\mu m x 20\mu m$). Others found a 42% increase in the extracted Young Modulus of control and treated HL60 (cytoD $1\mu M$) flowing in a straight channel of section $30\mu m$ x $30\mu m$ at very low flow rates and high buffer viscosity (Fregin et al., 2019).

Interestingly, a study in a cross shaped device operated at very high flow rates showed no significant difference in detected deformation of 3T3 cells upon administering pharmacological inhibitors of cytoskeletal components, suggesting that at high strain rates the cellular response may be dominated by other components (chromatin filaments or viscous cytosolic material) rather than the rigid actin filaments (Gossett et al., 2012).

4.3 Combined analysis of computational and experimental results

To relate experimental findings with computational results, the values of deformation were analysed in comparison with the main quantities involved in inducing stress on cells (shear and extensional rates). The trends of deformation of Jurkat and HL60 cells in the experiments with Buffer 0.25 at the maximum flow rate ($Q_{tot} = 100\frac{\mu l}{min}$) are displayed as compared to the respective values of shear (Figure 4.40) and extension (Figure 4.41).

As the width at the contraction w_c increases from 15 to 25 μm, both extensional and shear rate decreased, so did the detected deformation: this was in accordance with the expected decrease in the fluid induced forces (lower velocity and stresses). What is more interesting to note is the contribution of shear rate to the peak in deformation in the long channels ($L_c = 1000\mu m$) with respect to their short ones ($L_c = 500\mu m$): this was more visible in the maximum stresses scenario ($w_c = 15\mu m$) where a sharp increase in $\dot{\gamma}$ (about 65% larger than in the shorter channel) was the major contributor to the large deformation observed, with the extensional rate $\dot{\varepsilon}$ approximately half the value than the case with $L_c = 500\mu m$.

In the case of the straight channel, again shear played the major role in inducing deformation whereas the extensional rate was lower than any other hyperbolic channel.

A similar overview in the case of Buffer 0.50 at the maximum flow rate ($Q_{tot} = 14.4\frac{\mu l}{min}$) is given in Figures 4.42 and 4.43. Again the high deformation in the long channel ($L_c = 1000\mu m, w_c = 15\mu m$) could be given by the shear rate which is 50% higher with respect to the short channel with the same width.

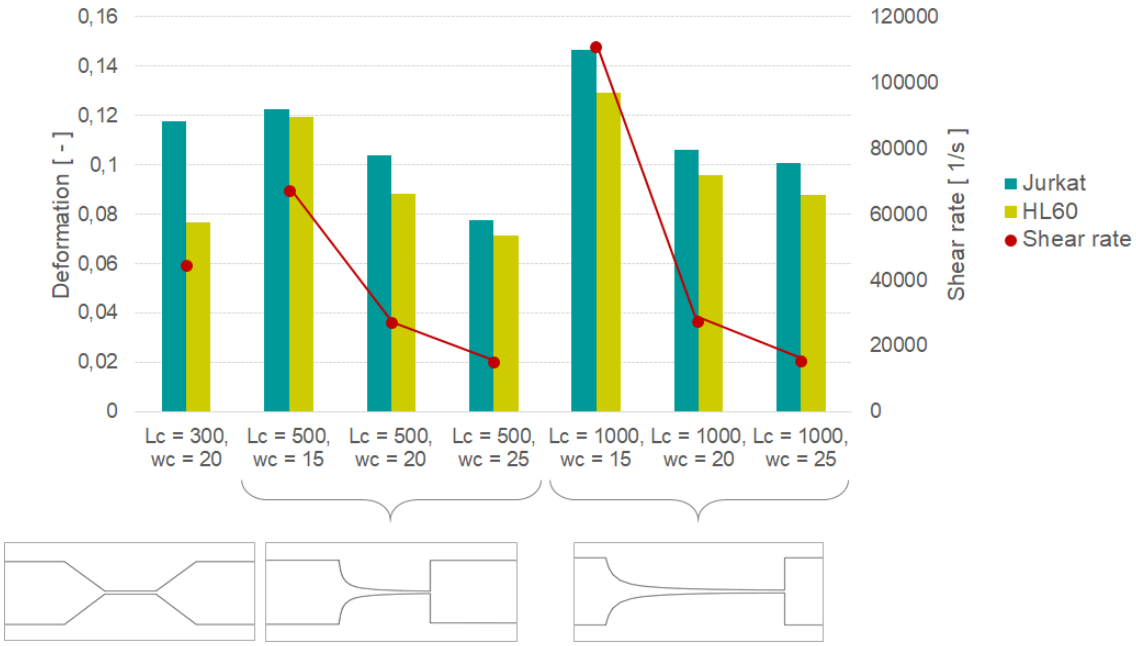

Figure 4.40: Evaluation of the deformation detected experimentally with respect to the shear rate. Values refer to the experiments and simulations with Buffer 0.25 and the corresponding maximum flow rate $Q_{tot} = 100\frac{\mu l}{min}$.

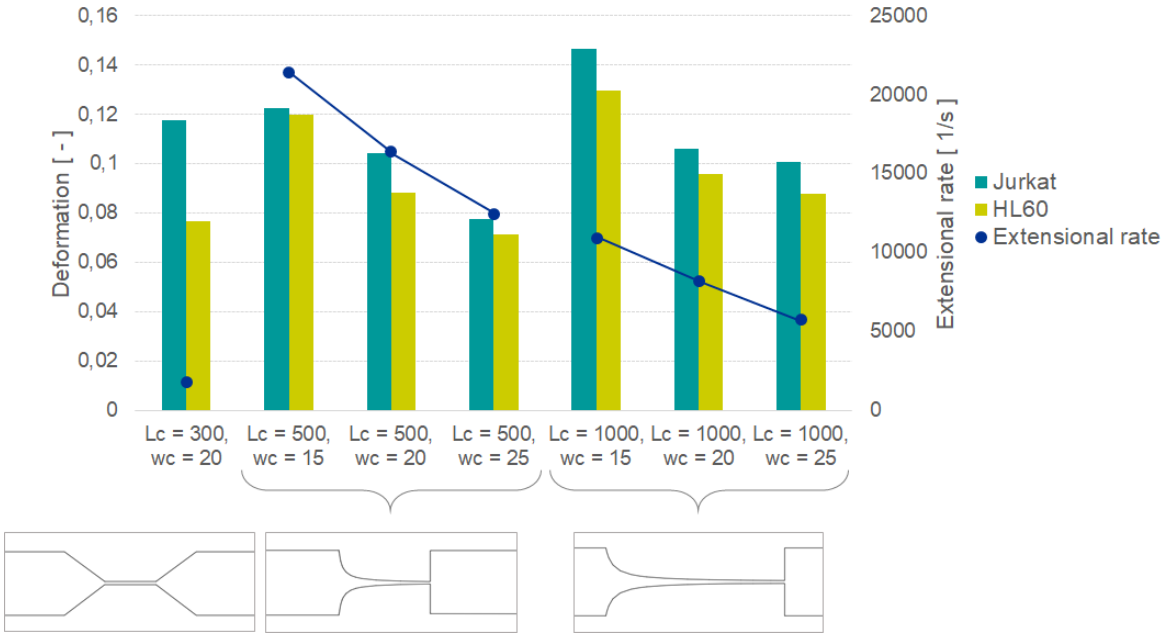

Figure 4.41: Evaluation of the deformation detected experimentally with respect to the extensional rate. Values refer to the experiments and simulations with Buffer 0.25 and the corresponding maximum flow rate $Q_{tot} = 100\frac{\mu l}{min}$.

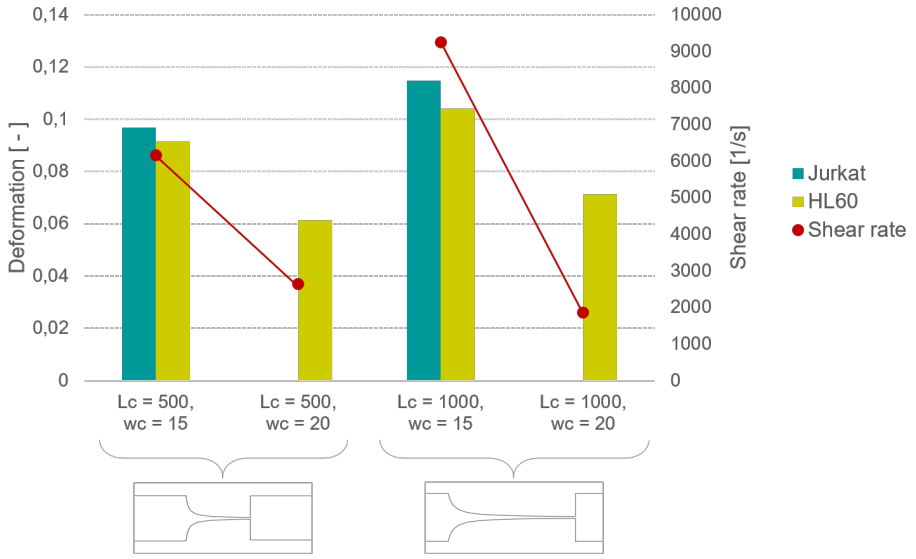

Figure 4.42: Evaluation of the deformation detected experimentally with respect to the shear rate. Values refer to the experiments and simulations with Buffer 0.50 and the corresponding maximum flow rate $Q_{tot} = 14.4\frac{\mu l}{min}$.

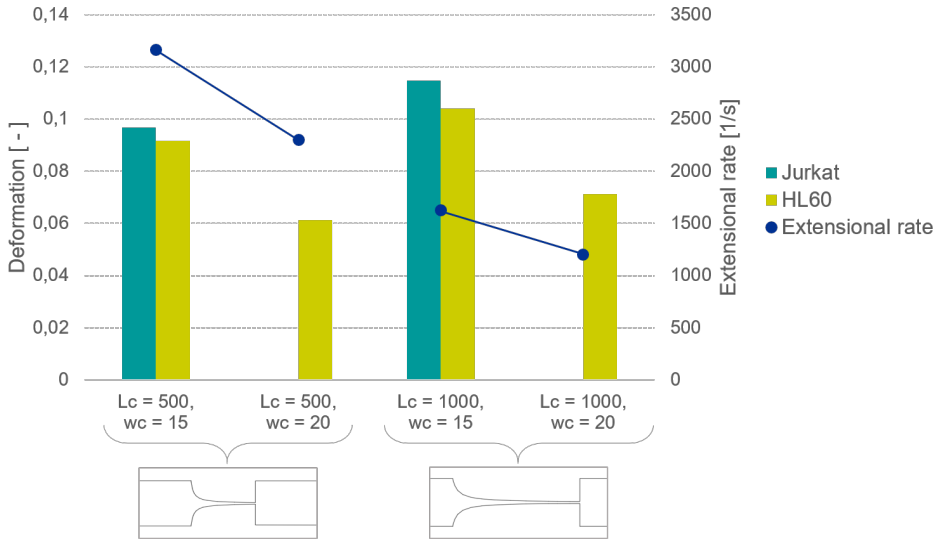

Figure 4.43: Evaluation of the deformation detected experimentally with respect to the extensional rate. Values refer to the experiments and simulations with Buffer 0.50 and the corresponding maximum flow rate $Q_{tot} = 14.4\frac{\mu l}{min}$.

4.4 Final considerations on optimal characteristics of the device

In the light of the experimental and computational results, the hyperbolic shape appears as an optimal solution in terms of fluid induced forces, comprising both a relevant extensional component and a shear one: to this extent, it overcomes the limits of the cross shape device, with almost no shear, and of the straight channel, with zero extension.

The comparison between short and long hyperbolic channels (two fold difference in length) revealed that the short hyperbolic channel with a pronounced curvature gave a more balanced distribution of shear and extensional effects providing a slightly lower deformation with respect to the long counterpart but still a significant and detectable response of the cell. Hence, it is reasonable and desirable to elect the "truly hyperbolic" shape (short channel) as optimal geometry for deformation measurements.

As far as the size is concerned, it is clear that this depends on the cells being tested, keeping in mind that an effective deformation is reached only when the cell size covers 30% to 90% of the channel cross section (Herbig et al., 2018). Also, the lower the cross section of the device, the larger will be the stresses on cells even at low flow rates, whereas larger cross sections expectedly induced almost no deformation at the lowest speeds (as observed especially for the case of $w_c = 25\mu m$ here).

It also need to be taken into account that cells have a strongly heterogeneous distribution of size within the same sample, given mostly by their stage in the cell cycle: thus, a margin of safety should be considered, especially for cell types that are thought to be stiffer then less likely to accommodate in a too small constriction. In this specific case, no clogging was observed in any of the experiments and a contraction width of $w_c = 15\mu m$ appeared well suited to induce a pronounced deformation on Jurkat and HL60 cells, thus can be deemed an optimal choice for cells with size in the same range

as the ones tested ($11 \div 13\mu m$, see Table 3.3 on page 43).

The height of $20\mu m$ was optimized from the first experimental trials and not tuned any more as it allowed for good focusing and not too asymmetric aspect ratio with the chosen widths.

For what regards image quality, it would be safe to affirm that the best solution in terms of reliability of results - that is the lowest possible motion blur and best focusing in the z direction - is the choice of a very viscous buffer (here, Buffer 0.50) and low speeds. Nonetheless, one needs to be aware of how realistic are the conditions with respect to the modelled situation: for example, thinking of the stress induced on cells in the accelerated motion of blood flowing into needles or catheters of smaller lumen with respect to the larger vessel they access, velocities lower than $1\frac{m}{s}$ as in the case of Buffer 0.50 would not be representative and Buffer 0.25 could be preferred, conjunctively with the use of higher flow rates. On the other way around, blood flow in capillaries can reach very low values in the order of $1\frac{cm}{s}$ thus the use of low flow rates would be more appropriate to simulate such condition.

Buffer 0.37 could be considered as an appropriate compromise between image quality and flow speed, providing good focusing in the z direction and allowing to use intermediate flow rates, limiting motion blur but still preserving significant fluid (and cell) velocity.

Undoubtedly, pushing the performance of the setup could improve the sensitivity considerably and overcome the limitations in terms of motion blur, allowing high quality measurements also at high speeds. There exist even more sophisticated high speed cameras with shorter exposure time ($t_{exp} = 200ns$, five time smaller than the one used here), but in this case a much more powerful light would be needed, possibly in stroboscopic mode, adding complexity and cost to an already high technology set up. Furthermore, the scope of this work lies more in analysing critically the parameters influencing the detected deformation and optimizing a platform to obtain reliable and relevant data, rather than pursuing an improvement in the setup and instrumentation.

To conclude, a hyperbolic channel with length $L_c = 500\mu m$, height $h = 20\mu m$ and width at the contraction $w_c = 15\mu m$ can be elected as optimal geometry for deformability measurements, whereas the choice of the appropriate buffer and consequently, flow rates, remains to be addressed specifically on a case by case basis as stated above.

Conclusions

The present work provides a platform to measure cell deformability in a fast, label free and cost effective way. Particular attention has been given to the realization of a flow field that could resemble the complex mixture of shear and extensional components occurring inside the body (e.g. in the microvasculature) or in extracorporeal devices (e.g. needles or catheters) having a much smaller diameter with respect to the typically large veins they access.

For this reason, a hyperbolic shape was elected as optimal since it featured both shear and extension, unlike the cross shaped or straight channels. Optimized conditions to probe cell mechanical properties in this scenario have been inferred to provide a reasonable solution in terms of image quality and physiological relevance of the conditions. With the sole use of bright field microscopy and a high speed camera, it was possible to discriminate the difference in deformation between two cell lines and to detect the effect of cytoskeletal changes as a macroscopic variation of stiffness in the case of cell fixation and treatment with an inhibitor of actin polymerization.

It is important to point out that, since the viscoelastic nature of human cells has been revealed, time dependence should be considered an important aspect of cell behaviour and must be taken into account: to this regard, this setup applied a quasi instantaneous force, unlike methods as cell transit in constrictions or AFM. The type of information that can be retrieved from either case is of course different: some groups adduced that cytoskeletal changes and nuclear stiffness are more likely to play a role in the deformation rates applied in deformability cytometry (Fregin et al., 2019) (Dudani et al., 2013). With the big advantage of a high throughput, the developed device allowed for the recording, detection and subsequent image processing of up to $4000\frac{cells}{s}$ flowing through the hyperbolic contraction.

The combined computational effort allowed to relate the experimental results on deformation with either extensional or shear components of the flow, revealing different deformation modes in the case of one or the other being preponderant.

5.1 Further developments

A crucial point of the whole experimental procedure was the quality of the acquired images: with a lower exposure time, motion blur could be significantly reduced to allow for higher quality images at much higher cell speeds. Moreover, when the shape and deformation modes of the cell become important, such as for example in the study of nuclear stiffness contribution to the overall deformation (Tatsumi et al., 2014), it is evident that a higher magnification would provide a more reliable reconstruction of the contours. This would be feasible only with a much stronger light of a pulsed LED, as also reported elsewhere (Otto et al., 2015) (Fregin et al., 2019).

Importantly, the automation of the process of recording and processing images in real time, as already attempted successfully elsewhere (Otto et al., 2015), would bring enormous advantage in terms of throughput and time effectiveness of the experiments. An interesting development of these systems has been already envisioned in the addition of a stiffness based separation for downstream processing (Urbanska et al., 2018). Another appealing proceeding could be the simultaneous probing of fluorescence in combination with deformation assessment, as attempted in a straight channel at very low cell speed to detect the subcellular distribution of fluorescent probes attached to the cells (Rosendahl et al., 2018), although technically unfeasible at high speed.

Overall, the label free approach to study of deformability and the numerous parameters and aspects of the cell behaviour that can be related to this property offers a high potential in the field of early disease detection and diagnosis of rare populations in clinical samples (e.g. circulating tumour cells) at a relatively low cost, high efficiency and time effectiveness, not to mention the absence of user bias that are present in non automated techniques. It is safe to foresee further and diverse applications of this type of assay as the complex relationships linking macro mechanical properties to cellular and molecular mechanisms are on the way of being unravelled.

Bibliography

Adamo, A., Sharei, A., Adamo, L., Lee, B., Mao, S., and Jensen, K. F. (2012). Microfluidics-based assessment of cell deformability. *Analytical Chemistry*, 84(15):6438–6443.

Alexopoulos, L. G., Haider, M. A., Vail, T. P., and Guilak, F. (2003). Alterations in the Mechanical Properties of the Human Chondrocyte Pericellular Matrix With Osteoarthritis. *Journal of Biomechanical Engineering*, 125:323–333.

Bento, D., Rodrigues, R. O., Faustino, V., Pinho, D., Fernandes, C. S., Pereira, A. I., Garcia, V., Miranda, J. M., and Lima, R. (2018). Deformation of red blood cells, air bubbles, and droplets in microfluidic devices: Flow visualizations and measurements. *Micromachines*, 9(4):151–169.

Brown, M. J., Hallam, J. A., Colucci-Guyon, E., and Shaw, S. (2001). Rigidity of Circulating Lymphocytes Is Primarily Conferred by Vimentin Intermediate Filaments. *The Journal of Immunology*, 166(11):6640–6646.

Byun, S., Son, S., Amodei, D., Cermak, N., Shaw, J., Kang, J. H., Hecht, V. C., Winslow, M. M., Jacks, T., Mallick, P., and Manalis, S. R. (2013). Characterizing deformability and surface friction of cancer cells. *Proceedings of the National Academy of Sciences*, 110(19):7580–7585.

Calejo, J., Pinho, D., Galindo-Rosales, F. J., Lima, R., and Campo-Deaño, L. (2016).

Particulate blood analogues reproducing the erythrocytes cell-free layer in a microfluidic device containing a hyperbolic contraction. *Micromachines*, 7(1):4–16.

Carlo, D. D. and Lee, L. P. (2008). Dynamic Single-Cell Analysis for Quantitative Biology. *Analytical Chemistry*, 78(23):7918–7925.

Cha, S., Shin, T., Lee, S. S., Shim, W., Lee, G., Lee, S. J., Kim, Y., and Kim, J. M. (2012). Cell stretching measurement utilizing viscoelastic particle focusing. *Analytical Chemistry*, 84:10471–10477.

Chen, J., Chen, D., Yuan, T., Chen, X., Xie, Y., Fu, H., Cui, D., Fan, X., and Khaing Oo, M. K. (2014). Blood plasma separation microfluidic chip with gradual filtration. *Microelectronic Engineering*, 128:36–41.

Cross, S. E., Jin, Y. S., Rao, J., and Gimzewski, J. K. (2007). Nanomechanical analysis of cells from cancer patients. *Nature Nanotechnology*, 2(12):780–783.

Darling, E. M. and Di Carlo, D. (2015). High-Throughput Assessment of Cellular Mechanical Properties. *Annual Review of Biomedical Engineering*, 17:35–62.

Del Giudice, F., Sathish, S., D'Avino, G., and Shen, A. Q. (2017). From the Edge to the Center: Viscoelastic Migration of Particles and Cells in a Strongly Shear-Thinning Liquid Flowing in a Microchannel. *Analytical Chemistry*, 89(24):13146–13159.

Di Carlo, D. (2012). A mechanical biomarker of cell state in medicine. *Journal of Laboratory Automation*, 17(1):32–42.

Discher, D. E., Janmey, P., and Wang, Y. L. (2005). Tissue cells feel and respond to the stiffness of their substrate. *Science*, 310(5751):1139–1143.

Dudani, J. S., Gossett, D. R., Tse, H. T., and Di Carlo, D. (2013). Pinched-flow hydrodynamic stretching of single-cells. *Lab on a Chip*, 13:3728–3734.

El-Ali, J., Sorger, P. K., and Jensen, K. F. (2006). Cells on chips. *Nature*, 442:403–411.

Faustino, V., Pinho, D., Yaginuma, T., Calhelha, R. C., Ferreira, I. C., and Lima, R. (2014). Extensional flow-based microfluidic device: Deformability assessment of red blood cells in contact with tumor cells. *Biochip Journal*, 8(1):42–47.

Fay, M. E., Myers, D. R., Kumar, A., Turbyfield, C. T., Byler, R., Crawford, K., Mannino, R. G., Laohapant, A., Tyburski, E. A., Sakurai, Y., Rosenbluth, M. J., Switz, N. A., Sulchek, T. A., Graham, M. D., and Lam, W. A. (2016). Cellular softening mediates leukocyte demargination and trafficking, thereby increasing clinical blood counts. *Proceedings of the National Academy of Sciences*, 113(8):1987–1992.

Feigl, K., Tanner, F. X., Edwards, B. J., and Collier, J. R. (2003). A numerical study of the measurement of elongational viscosity of polymeric fluids in a semihyperbolically converging die. *Journal of Non-Newtonian Fluid Mechanics*, 115(2-3):191–215.

Fregin, B., Czerwinski, F., Biedenweg, D., Girardo, S., Gross, S., Aurich, K., and Otto, O. (2019). High-throughput single-cell rheology in complex samples by dynamic real-time deformability cytometry. *Nature Communications*, 10:415–426.

Geiger, B., Bershadsky, A., Pankov, R., and Yamada, K. M. (2001). Transmembrane extracellular matrix-cytoskeleton crosstalk. *Nature Reviews Molecular Cell Biology*, 2:793–805.

Gossett, D. R., Tse, H. T. K., Lee, S. A., Ying, Y., Lindgren, A. G., Yang, O. O., Rao, J., Clark, A. T., and Di Carlo, D. (2012). Hydrodynamic stretching of single cells for large population mechanical phenotyping. *Proceedings of the National Academy of Sciences*, 109(20):7630–7635.

Guck, J., Schinkinger, S., Lincoln, B., Wottawah, F., Ebert, S., Romeyke, M., Lenz, D., Erickson, H. M., Ananthakrishnan, R., Mitchell, D., Kas, J., Ulvick, S., and Bilby, C. (2005). Optical deformability as an inherent cell marker for testing malignant transformation and metastatic competence. *Biophysical Journal*, 88:3689–3698.

Guilak, F., Tedrow, J. R., and Burgkart, R. (2000). Viscoelastic properties of the cell nucleus. *Biochemical and Biophysical Research Communications*, 169:781–786.

Guillou, L., Dahl, J. B., Lin, J. M. G., Barakat, A. I., Husson, J., Muller, S. J., and Kumar, S. (2016). Measuring Cell Viscoelastic Properties Using a Microfluidic Extensional Flow Device. *Biophysical Journal*, 111:2039–2050.

Guo, Q., Duffy, S. P., and Ma, H. (2017). Microfluidic Technologies for Deformability-Based Cell Sorting. In *Microtechnology for Cell Manipulation and Sorting*.

Guo, Q., Reiling, S. J., Rohrbach, P., and Ma, H. (2012). Microfluidic biomechanical assay for red blood cells parasitized by Plasmodium falciparum. *Lab on a Chip*, 12(6):1143–1150.

Guzniczak, E., Mohammad Zadeh, M., Dempsey, F., Jimenez, M., Bock, H., Whyte, G., Willoughby, N., and Bridle, H. (2017). High-throughput assessment of mechanical properties of stem cell derived red blood cells, toward cellular downstream processing. *Scientific Reports*, 7(1):1–11.

Herbig, M., Kräter, M., Plak, K., Müller, P., Guck, J., and Otto, O. (2018). Real-time deformability cytometry: Label-free functional characterization of cells. In *Flow cytometry protocols. Methods in Molecular Biology*.

Hou, H. W., Bhagat, A. A. S., Lin Chong, A. G., Mao, P., Wei Tan, K. S., Han, J., and Lim, C. T. (2010). Deformability based cell margination - A simple microfluidic design for malaria-infected erythrocyte separation. *Lab on a Chip*, 10:2605–2613.

Hou, H. W., Li, Q. S., Lee, G. Y. H., Kumar, A. P., Ong, C. N., and Lim, C. T. (2009). Deformability study of breast cancer cells using microfluidics. *Biomedical Microdevices*, 11:557–564.

Islam, M., Mezencev, R., McFarland, B., Brink, H., Campbell, B., Tasadduq, B., Waller, E. K., Lam, W., Alexeev, A., and Sulchek, T. (2018). Microfluidic cell sorting

by stiffness to examine heterogenic responses of cancer cells to chemotherapy. *Cell Death and Disease*, 9:239–251.

Lam, W. A., Rosenbluth, M. J., and Fletcher, D. A. (2007). Chemotherapy exposure increases leukemia cell stiffness. *Blood*, 109(8):3505–3508.

Lee, S. S., Yim, Y., Ahn, K. H., and Lee, S. J. (2009). Extensional flow-based assessment of red blood cell deformability using hyperbolic converging microchannel. *Biomedical Microdevices*, 11:1021–1027.

Masaeli, M., Gupta, D., O'Byrne, S., Tse, H. T., Gossett, D. R., Tseng, P., Utada, A. S., Jung, H. J., Young, S., Clark, A. T., and Di Carlo, D. (2016). Multiparameter mechanical and morphometric screening of cells. *Scientific Reports*, 6:37863–37884.

Milo, R., Jorgensen, P., Moran, U., Weber, G., and Springer, M. (2009). BioNumbers The database of key numbers in molecular and cell biology. *Nucleic Acids Research*, 38(SUPPL.1):750–753.

Moeendarbary, E. and Harris, A. R. (2014). Cell mechanics: Principles, practices, and prospects. *Wiley Interdisciplinary Reviews: Systems Biology and Medicine*, 6:371–388.

Morikawa, M., Inoue, Y., Sumi, Y., Kuroda, Y., and Tanaka, H. (2015). Leukocyte deformability is a novel biomarker to reflect sepsis-induced disseminated intravascular coagulation. *Acute Medicine & Surgery*, 2(1):13–20.

Murphy, T. W., Zhang, Q., Naler, L. B., Ma, S., and Lu, C. (2018). Recent advances in the use of microfluidic technologies for single cell analysis. *Analyst*, 143(1):60–80.

Nikon. Depth of Field and Depth of Focus | MicroscopyU.

Ober, T. J., Haward, S. J., Pipe, C. J., Soulages, J., and McKinley, G. H. (2013). Microfluidic extensional rheometry using a hyperbolic contraction geometry. *Rheologica Acta*, 52:529–546.

Oliveira, M. S., Alves, M. A., Pinho, F. T., and McKinley, G. H. (2007). Viscous flow through microfabricated hyperbolic contractions. *Experiments in Fluids*, 43:437–451.

Otto, O., Rosendahl, P., Mietke, A., Golfier, S., Herold, C., Klaue, D., Girardo, S., Pagliara, S., Ekpenyong, A., Jacobi, A., Wobus, M., Töpfner, N., Keyser, U. F., Mansfeld, J., Fischer-Friedrich, E., and Guck, J. (2015). Real-time deformability cytometry: On-the-fly cell mechanical phenotyping. *Nature Methods*, 12(3):199–202.

Pajerowski, J. D., Dahl, K. N., Zhong, F. L., Sammak, P. J., and Discher, D. E. (2007). Physical plasticity of the nucleus in stem cell differentiation. *Proceedings of the National Academy of Sciences*, 104(40):15619–15624.

Piergiovanni, M. (2018). *Single cell fluid dynamics for the study of the liver microcirculation: computational modelling and in vitro validation*. PhD thesis, Poltecnico di Milano.

Pravincumar, P., Bader, D. L., and Knight, M. M. (2012). Viscoelastic Cell Mechanics and Actin Remodelling Are Dependent on the Rate of Applied Pressure. *PLoS ONE*, 7(9).

Qie, L., Lim, C. T., Mills, J. P., Qie, L., Dao, M., and Suresh, S. (2004). Nonlinear Elastic and Viscoelastic Deformation of the Human Red Blood Cell with Optical Tweezers Developing an Indonesian forest monitoring network View project Radiation-Resistant Behavior of Nano-gradient Steel in Extreme Radiation Environments View pro. *Tech Science Press MCB*, 1(3):169–180.

Rand, R. and Burton, A. (1964). Mechanical Properties of the Red Cell Membrane I . Membrane Stiffness and Intracellular Pressure. *Biophysical journal*, 4:115–135.

Remmerbach, T. W., Wottawah, F., Dietrich, J., Lincoln, B., Wittekind, C., and Guck, J. (2009). Oral cancer diagnosis by mechanical phenotyping. *Cancer Research*, 69(5):1728–1732.

Rodrigues, R. O., Bañobre-López, M., Gallo, J., Tavares, P. B., Silva, A. M., Lima, R., and Gomes, H. T. (2016a). Haemocompatibility of iron oxide nanoparticles synthesized for theranostic applications: a high-sensitivity microfluidic tool. *Journal of Nanoparticle Research*, 18:194.

Rodrigues, R. O., Lopes, R., Pinho, D., Pereira, A. I., Garcia, V., Gassmann, S., Sousa, P. C., and Lima, R. (2016b). In vitro blood flow and cell-free layer in hyperbolic microchannels: Visualizations and measurements. *Biochip Journal*, 10(1):9–15.

Rodrigues, R. O., Pinho, D., Faustino, V., and Lima, R. (2015). A simple microfluidic device for the deformability assessment of blood cells in a continuous flow. *Biomedical Microdevices*, 17:108–117.

Rosenbluth, M. J., Lam, W. A., and Fletcher, D. A. (2006). Force microscopy of nonadherent cells: A comparison of leukemia cell deformability. *Biophysical Journal*, 90:2994–3003.

Rosenbluth, M. J., Lam, W. A., and Fletcher, D. A. (2008). Analyzing cell mechanics in hematologic diseases with microfluidic biophysical flow cytometry. *Lab on a Chip*, 8(7):1062–1070.

Rosendahl, P., Plak, K., Jacobi, A., Kraeter, M., Toepfner, N., Otto, O., Herold, C., Winzi, M., Herbig, M., Ge, Y., Girardo, S., Wagner, K., Baum, B., and Guck, J. (2018). Real-time fluorescence and deformability cytometry. *Nature Methods*, 15(5):355–358.

Scanlon, V. and Sanders, T. (2007). *Essentials of anatomy and physiology.* F. A. Davis Company, fifth edition.

Schulze, C., Wetzel, F., Kueper, T., Malsen, A., Muhr, G., Jaspers, S., Blatt, T., Wittern, K. P., Wenck, H., and Käs, J. A. (2012). Stiffening of human skin fibroblasts with age. *Clinics in Plastic Surgery*, 39(1):9–20.

Sousa, P. C., Pinho, F. T., Oliveira, M. S. N., and Alves, M. A. (2011). Extensional flow of blood analog solutions in microfluidic devices. *Biomicrofluidics*, 5(1):014108.

Suresh, S. (2006). Mechanical response of human red blood cells in health and disease: Some structure-property-function relationships. *Journal of Materials Research*, 21(8):1871–1877.

Suresh, S. (2007). Biomechanics and biophysics of cancer cells. *Acta Materialia*, 3(4):413–438.

Tatsumi, K., Haizumi, K., Sugimoto, K., and Nakabe, K. (2014). Analysis of lymphocytes deformation in microchannel flows using compound drop model. In *Journal of Physics: Conference Series*.

Tsai, M. A., Waugh, R. E., and Keng, P. C. (1996). Cell cycle-dependence of HL-60 cell deformability. *Biophysical Journal*, 70:2023–2029.

Tse, H. T. K., Mislick, K., Rao, J., Gossett, D. R., Moon, Y. S., Di Carlo, D., Masaeli, M., Ying, Y., Sohsman, M., and Adams, R. P. (2013). Quantitative Diagnosis of Malignant Pleural Effusions by Single-Cell Mechanophenotyping. *Science Translational Medicine*, 5(212).

Ung, W. L., Weitz, D. A., Heyman, J. A., Griffiths, A. D., Mazutis, L., and Gilbert, J. (2013). Single-cell analysis and sorting using droplet-based microfluidics. *Nature Protocols*, 8(5):870–891.

Urbanska, M., Rosendahl, P., Kräter, M., and Guck, J. (2018). High-throughput single-cell mechanical phenotyping with real-time deformability cytometry. In *Methods in Cell Biology*.

Wang, G., Mao, W., Byler, R., Patel, K., Henegar, C., Alexeev, A., and Sulchek, T. (2013). Stiffness Dependent Separation of Cells in a Microfluidic Device. *PLoS ONE*, 8(10):e75901.

Wang, N., Butler, J. P., and Ingber, D. E. (1993). Mechanotransduction across the cell surface and through the cytoskeleton. *Science*, 260(5111):1124–1127.

Wang, N., Naruse, K., Stamenovic, D., Fredberg, J. J., Mijailovich, S. M., Tolic-Norrelykke, I. M., Polte, T., Mannix, R., and Ingber, D. E. (2001). Mechanical behavior in living cells consistent with the tensegrity model. *Proceedings of the National Academy of Sciences*, 98(14):7765–7770.

Worthen, G. S., Schwab, B., Elson, E. L., and Downey, G. P. (1989). Mechanics of stimulated neutrophils: Cell stiffening induces retention in capillaries. *Science*, 245(4914):183–186.

Xu, Z., Zheng, Y., Wang, X., Shehata, N., Wang, C., and Sun, Y. (2018). Stiffness increase of red blood cells during storage. *Microsystems & Nanoengineering*, page 17103.

Yaginuma, T., Oliveira, M. S., Lima, R., Ishikawa, T., and Yamaguchi, T. (2013). Human red blood cell behavior under homogeneous extensional flow in a hyperbolic-shaped microchannel. *Biomicrofluidics*, 7:054110.

Zheng, Y., Nguyen, J., Wei, Y., and Sun, Y. (2013). Recent advances in microfluidic techniques for single-cell biophysical characterization. *Lab on a Chip*, 13:2464.

Zheng, Y., Wen, J., Nguyen, J., Cachia, M. A., Wang, C., and Sun, Y. (2015). Decreased deformability of lymphocytes in chronic lymphocytic leukemia. *Scientific Reports*, 5:7613.

Appendix

A.1 Computational analysis settings

Simulations were performed for Buffer 0.25 and Buffer 0.50 with all the corresponding flow rates (summarized in table 3.4): inlet velocities for the upstream sheath system were calculated as mean velocities in each condition as

$$v_{in} = \frac{Q}{A} \quad \left[\frac{\frac{\mu l}{min}}{\mu m^2}\right] \tag{A.1}$$

then converted in SI units $[\frac{m}{s}]$. Taking into account the cross sections for the sheath fluid and the sample in the upstream part:

- $A_{sheath} = h \cdot w = 20\mu m \cdot 200\mu m = 400\mu m^2 = 4 \cdot 10^{-10} m^2$;
- $A_{sample} = h \cdot w = 20\mu m \cdot 150mum = 300\mu m^2 = 3 \cdot 10^{-10} m^2$

with h and w the height and width of the channel respectively (Figure A.1). The resulting values are reported in Table A.1 and Table A.2 for Buffer 0.25 and Buffer 0.50 respectively.

$\boldsymbol{Q_{sample}[\frac{\mu l}{min}]}$	$\boldsymbol{Q_{sheath}[\frac{\mu l}{min}]}$	$\boldsymbol{v_{in,sample}[\frac{m}{s}]}$	$\boldsymbol{v_{in,sample}[\frac{m}{s}]}$
10	30	0.062	0.056
15	45	0.937	0.834
20	60	0.125	0.111
25	75	0.156	0.139

Table A.1: Sample flow rates and respective inlet velocities for Buffer 0.25.

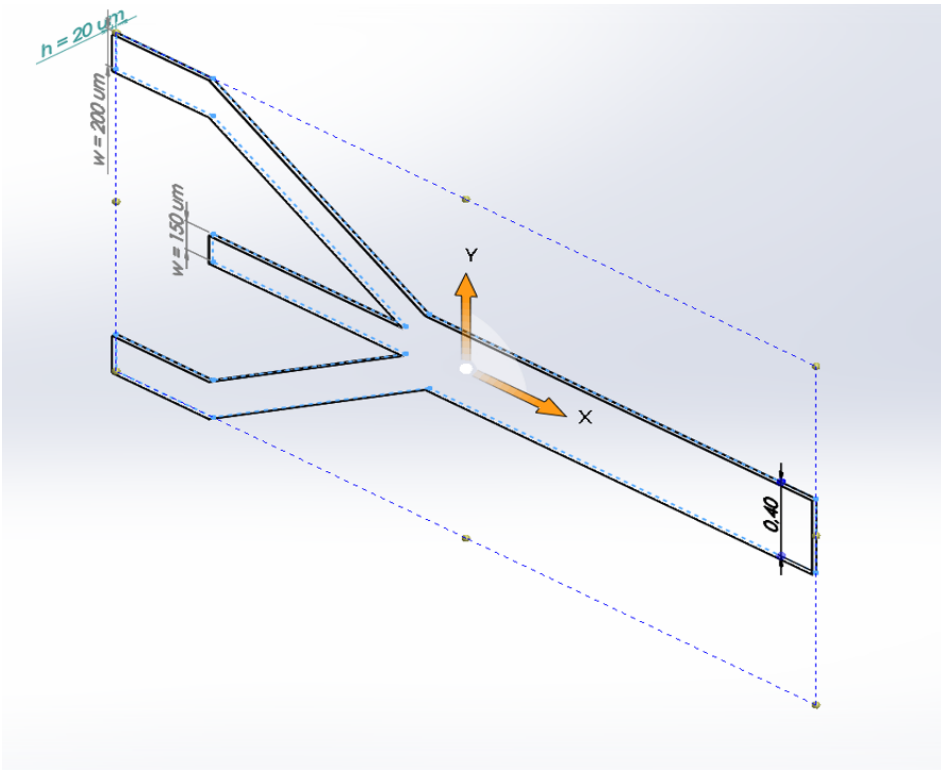

Figure A.1: Representation of the sheath flow system inlets for the calculation of the mean inlet velocities. The upper and lower branches serve as sheath fluid inlet, whereas the central one is the sample inlet.

$Q_{sample}\left[\frac{\mu l}{min}\right]$	$Q_{sheath}\left[\frac{\mu l}{min}\right]$	$v_{in,sample}\left[\frac{m}{s}\right]$	$v_{in,sample}\left[\frac{m}{s}\right]$
0.6	1.8	0.00375	0.0033
1.2	3.6	0.0075	0.0067
1.8	5.4	0.0112	0.0111
2.4	7.2	0.0150	0.0133
3.6	10.8	0.0225	0.0222

Table A.2: Sample flow rates and respective inlet velocities for Buffer 0.50.

A.2 Complete report of computational results

For the sake of completeness, the punctual values of the main parameters of interest (maximum wall shear stress, maximum velocity, extensional and shear rates along the centerline) for all simulations are given in the following tables.

It is clear at a glance that the shear rate was higher than the extensional counterpart in all scenarios.

Of particular relevance is the case of the straight channel which is expected to have a nearly zero extension and high shear. For the case of high velocities (Buffer 0.25) a non zero extensional rate was reported (yet 2 order of magnitude lower than the shear rate at the same flow rate); for the case of lower flow rates (Buffer 0.50) a zero extensional rate was found (Table A.5). The shear rates, in turn, were almost double the ones in the hyperbolic channel of the same width ($w_c = 20\mu m$) for high flow rates (Buffer 0.25) and comparable for low flow rates (Buffer 0.50).

As for the hyperbolic channels, the ratio between shear and extensional rate ($\frac{\dot{\gamma}}{\dot{\varepsilon}}$) is higher for Buffer 0.25 (higher flow rates) with respect to Buffer 0.50 in all cases (two rightmost columns in Tables A.4, A.3).

Specifically, this quantity is larger for the long channels ($L_c = 1000\mu m$), and for both lengths shear predominates over extension more significantly at higher velocities ($w_c = 15\mu m$): at lower speed the two quantities assume closer values, as evident from the case of $w_c = 25\mu m$.

The evaluation of shear stress is important to observe that the hyperbolic shape imparts a lower stress at the walls with respect to the straight channel, as can easily be seen by comparing the values of τ at the same width (Straight channel VS short hyperbolic channel with $w_c = 20\mu m$): the stress imparted by the straight channel is much closer to the case of $w_c = 15\mu m$ for the hyperbolic counterpart. In contrast, this is not true for the case of lower flow rates (Buffer 0.50) where comparable values of τ were found for the straight channel and the corresponding hyperbolic channel ($L_c = 500\mu m, w_c = 20\mu m$).

		$Q_{tot}\left[\frac{\mu l}{min}\right]$	$\tau_{max}[Pa]$	$v_{max}\left[\frac{m}{s}\right]$	$\dot{\gamma}\left[\frac{1}{s}\right]$	$\dot{\varepsilon}\left[\frac{1}{s}\right]$
$w_c = 15\mu m$	Buffer 0.25	40	3470	4.31	29991	8590
		60	5500	6.39	43411	12899
		80	7360	8.42	55854	17181
		100	9410	10.4	67377	21414
	Buffer 0.50	2.4	481	0.24	893	458
		4.8	818	0.48	1713	922
		7.2	1160	0.73	2725	1461
		9.6	1510	0.99	3863	2029
		14.4	2240	1.53	6163	3167
$w_c = 20\mu m$	Buffer 0.25	40	2350	3.25	12861	6771
		60	3500	4.52	18275	9972
		80	4660	6.35	23021	13220
		100	5830	7.84	27156	16401
	Buffer 0.50	2.4	349	0.18	477	349
		4.8	521	0.36	809	695
		7.2	755	0.54	1212	1100
		9.6	956	0.74	1747	1519
		14.4	1430	1.12	2640	2301
$w_c = 25\mu m$	Buffer 0.25	40	1680	2.62	6933	4856
		60	2490	3.89	9920	7287
		80	3310	5.13	12611	9688
		100	4140	6.35	15028	12050
	Buffer 0.50	2.4	280	0.15	303	247
		4.8	449	0.29	538	496
		7.2	554	0.43	755	746
		9.6	744	0.58	1013	991
		14.4	1060	0.88	1644	1569

Table A.3: Results of the simulations with the short hyperbolic channels ($L_c = 500\mu m$).

		$Q_{tot}\left[\frac{\mu l}{min}\right]$	$\tau_{max}[Pa]$	$v_{max}\left[\frac{m}{s}\right]$	$\dot{\gamma}\left[\frac{1}{s}\right]$	$\dot{\varepsilon}\left[\frac{1}{s}\right]$
$w_c = 15\mu m$	Buffer 0.25	40	3820	4.55	47948	4341
		60	5650	6.79	70115	6531
		80	7430	9.00	91111	8730
		100	9270	1.12	110959	10935
	Buffer 0.50	2.4	492	0.25	1212	232
		4.8	841	0.50	2307	480
		7.2	1200	0.77	3681	776
		9.6	1560	1.06	5304	1075
		14.4	2310	1.61	9249	1624
$w_c = 20\mu m$	Buffer 0.25	40	2290	3.31	12008	3287
		60	3390	4.94	17496	4941
		80	4490	6.55	22642	6596
		100	5590	8.13	27150	8248
	Buffer 0.50	2.4	341	0.18	341	170
		4.8	452	0.40	607	389
		7.2	679	0.6	853	584
		9.6	907	0.80	1351	784
		14.4	1390	1.13	1865	1201
$w_c = 25\mu m$	Buffer 0.25	40	1630	2.97	6534	2297
		60	2410	3.98	9567	3468
		80	3190	5.28	12444	4643
		100	3970	6.56	15172	5819
	Buffer 0.50	2.4	247	0.15	256	116
		4.8	393	0.29	383	231
		7.2	540	0.44	513	354
		9.6	694	0.59	692	501
		14.4	1000	0.91	1063	759

Table A.4: Results of the simulation with the long hyperbolic channels ($L_c = 1000\mu m$).

	$Q_{tot}\left[\frac{\mu l}{min}\right]$	$\tau_{max}[Pa]$	$v_{max}\left[\frac{m}{s}\right]$	$\dot{\gamma}\left[\frac{1}{s}\right]$	$\dot{\varepsilon}\left[\frac{1}{s}\right]$
Buffer 0.25	40	3210	3.49	17596	37.8
	60	5260	5.24	26534	282
	80	7470	6.98	35579	865
	100	9780	8.72	44631	1798
Buffer 0.50	2.4	353	0.19	184	0.311
	4.8	570	0.38	369	0.535
	7.2	772	0.57	559	0.681
	9.6	1010	0.77	778	0.755
	14.4	1520	1.19	1329	0.832

Table A.5: Results of the simulations with the straight channel.

Appendix

B.1 Simulation with the cross shaped channel

In order to compare the obtained results with the previous work in our group Piergiovanni (2018), a cross slot device with size $20\mu m$ x $20\mu m$ producing extensional flow was also studied. A simple mechanism of inertial focusing was employed, with the use of long straight channels (Figure B.1). Simulations were performed for just one flow rate ($Q_{in} = 90\frac{\mu l}{min}$, Buffer 0.25) to assess the difference in conditions with respect to the cases of the straight and hyperbolic channels in the "maximum stress" scenarios, that is the maximum flow rates tested for the corresponding channels.

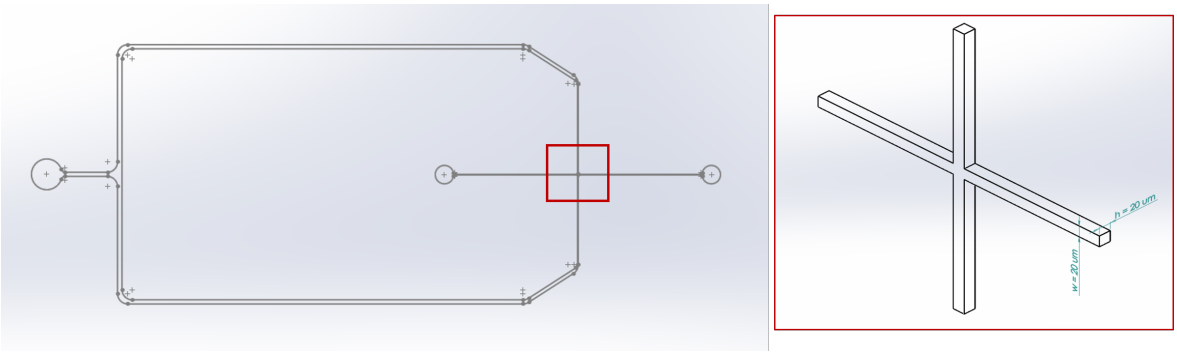

Figure B.1: Design of the cross shaped device and detailed view of the cross with dimensions.

As found in literature (see State of the art) this shape produces hyperbolic streamlines with a stagnation point in the centre of the cross where, correspondingly, a region

with very high extensional rate is found (Figure B.2). The shear rate was expectedly very low, presenting two opposite peaks of insignificant magnitude (0.3 s^{-1}) in correspondence with the centre of the cross; on the other hand, the extensional rate was very high with the maximum at the centre of the cross being around 320'000, much higher than $\dot{\varepsilon}$ for all hyperbolic and straight channels (see Tables in Appendix A).

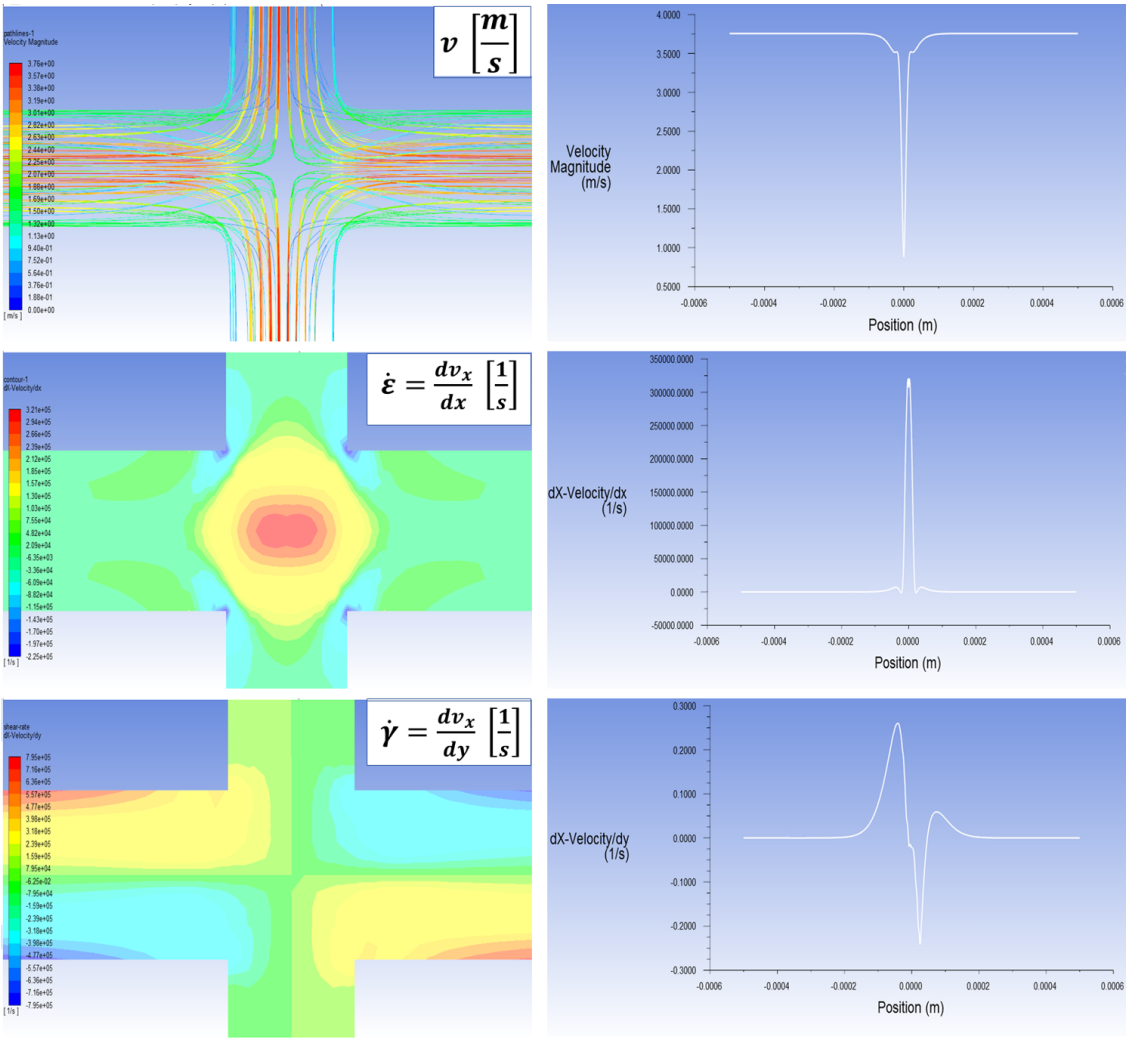

Figure B.2: Velocity streamlines, extensional rate contours, shear rate contours (left panel) and respective profile along the centreline(right panel) in the cross shaped device ($Q_{in} = 90\frac{\mu l}{min}$ for both inlets).

Appendix

C.1 Complete report of experimental results

For the sake of completeness, the punctual values of the evaluated parameters (Ratio and Deformation) for all experiments are given in the following tables. These refer to the peak of the deformation and ratio density distribution for each case, as explained in Materials and Methods (Figure 4.17 on page 87).

		Jurkat		**HL60**	
	$Q_{tot}[\frac{\mu l}{min}]$	Deformation [-]	Ratio [-]	Deformation [-]	Ratio [-]
Buffer 0.25	40	0.0520	1.17	0.0368	1.11
	60	0.0587	1.22	0.0464	1.23
	80	0.0906	1.48	0.0611	1.45
	100	0.1250	1.73	0.0777	1.55

Table C.1: Results of the experiments with the straight channel.

			Jurkat		HL60	
		$Q_{tot}[\frac{\mu l}{min}]$	$Deformation[-]$	$Ratio[-]$	$Deformation[-]$	$Ratio[-]$
$w_c = 15\mu m$	Buffer 0.25	40	0.0605	1.13	0.0405	1.13
		60	0.0742	1.19	0.0585	1.21
		80	0.1107	1.45	0.0882	1.55
		100	0.1224	1.82	0.1196	1.77
	Buffer 0.50	2.4	0.0611	1.11	0.0500	1.15
		4.8	0.0663	1.16	0.0596	1.16
		7.2	0.0777	1.30	0.0646	1.21
		9.6	0.0834	1.36	0.0714	1.24
		14.4	0.0968	1.44	0.0916	1.39
	Buffer 0.37	20	0.0564	1.21	-	-
		28	0.0755	1.43	-	-
		40	0.0920	1.60	-	-
		48	0.0963	1.63	-	-
		60	0.1166	1.72	-	-
$w_c = 20\mu m$	Buffer 0.25	40	0.0367	1.05	0.0288	1.06
		60	0.0599	1.19	0.0523	1.13
		80	0.0722	1.37	0.0650	1.16
		100	0.1040	1.50	0.0883	1.35
	Buffer 0.37	20	0.0507	1.03	-	-
		28	0.0519	1.10	-	-
		40	0.0699	1.22	-	-
		48	0.0726	1.34	-	-
		60	0.0849	1.41	-	-
	Buffer 0.50	2.4	-	-	0.0340	1.01
		4.8	-	-	0.0339	1.09
		7.2	-	-	0.0415	1.14
		9.6	-	-	0.0524	1.15
		14.7	-	-	0.0613	1.21
$w_c = 25\mu m$	Buffer 0.25	40	0.0303	0.972	0.0197	1.04
		60	0.0384	1.04	0.0256	1.05
		80	0.0575	1.06	0.0442	1.09
		100	0.0777	1.28	0.0714	1.24
	Buffer 0.37	20	0.0408	1.02	-	-
		28	0.0432	1.06	-	-
		40	0.0503	1.20	-	-
		48	0.0063	1.23	-	-
		60	0.0688	1.30	-	-

Table C.2: Results of the experiments with the short hyperbolic channel ($L_c = 500\mu m$).

			Jurkat		HL60	
		$Q_{tot}[\frac{\mu l}{min}]$	$Deformation[-]$	$Ratio[-]$	$Deformation[-]$	$Ratio[-]$
$w_c = 15\mu m$	Buffer 0.25	40	0.0912	1.12	0.0444	1.19
		60	0.0830	1.39	0.0828	1.35
		80	0.1204	1.72	0.1114	1.64
		100	0.1465	1.95	0.1294	1.85
	Buffer 0.50	2.4	0.0797	1.18	0.0594	1.15
		4.8	0.0861	1.20	0.0620	1.24
		7.2	0.0859	1.34	0.0741	1.27
		9.6	0.0954	1.45	0.0855	1.33
		14.4	0.0115	1.62	0.1041	1.41
$w_c = 20\mu m$	Buffer 0.25	40	0.0390	1.03	0.0370	1.02
		60	0.0707	1.16	0.0575	1.12
		80	0.0848	1.24	0.0721	1.27
		100	0.1062	1.49	0.0958	1.51
	Buffer 0.50	0.6	-	-	0.0348	1.02
		1.2	-	-	0.0480	1.05
		1.8	-	-	0.0514	1.08
		2.4	-	-	0.0542	1.18
		3.6	-	-	0.0630	1.26
$w_c = 25\mu m$	Buffer 0.25	40	0.0284	1.01	0.0215	1.05
		60	0.0529	1.19	0.0399	1.07
		80	0.0711	1.24	0.0595	1.13
		100	0.1006	1.54	0.0879	1.32

Table C.3: Results of the experiments with the long hyperbolic channel ($L_c = 1000\mu m$).